HDR

Alain Burgisser

Mémoire présenté en vue de l'obtention de l'Habilitation à Diriger des Recherches

par

Alain Burgisser
Chargé de Recherche
ISTO - UMR 6113 – UO-CNRS

Soutenue le 18 novembre 2009

devant le jury composé de :

Bruno Scaillet (ISTO, Orléans) - président
Claude Jaupart (IPGP, Paris) - rapporteur
Stephen Tait (IPGP, Paris) – rapporteur
Timothy Druitt (LMV, Clermont Ferrand) - rapporteur
Jean-Louis Bourdier (ISTO, Orléans) - examinateur

Sommaire

Partie I

Résumé des travaux

Avant propos

Ce mémoire contient les informations nécessaires au jury pour parvenir à une conclusion quant à ma capacité à diriger des recherches. Ni plus, ni moins.

Résumé du cheminement scientifique et repères chronologiques

Mon doctorat et mon post-doctorat à l'Université d'Alaska Fairbanks m'ont permis d'explorer les approches expérimentales, de terrain et théoriques pour mieux comprendre des phénomènes volcaniques critiques. De 1999 à 2004, j'ai réalisé plusieurs études de terrain sur des volcans d'Alaska et du Mexique qui se concentraient sur les dépôts d'éruptions explosives (Burgisser, 2005 ; Burgisser et Gardner, 2006 ; Gardner et al., 2007). Dans chaque étude, j'ai relié des mesures quantitatives de terrain à des modèles physiques que j'ai développés. L'étude de Burgisser et Gardner (2006) relie la taille et la densité de pyroclasts trouvés côte à côte à une distance donnée du cratère qui les a expulsés au mécanisme de tri qui a le plus vraisemblablement causé leur dépôt simultané. Les deux autres études lient le modèle théorique de transport de particules par gaz turbulent exposé dans Burgisser et Bergantz (2002) aux données de terrain. Un exemple de ces études se trouve dans la Partie III. La plupart de ces études de terrain ont été conduites dans des endroits reculés et dans des environnements naturels difficiles, ce qui m'a préparé à encadrer des post-doctorants et doctorants sur les volcans actifs ciblés par mes projets en cours (Soufrière Hills sur l'île de Montserrat dans les Caraïbes et Llaima au Chili).

Durant mon séjour en Alaska, j'ai également mené une étude expérimentale ciblée sur des décompressions à haute température de laves naturelles (Burgisser et Gardner, 2005). Etant la première évidence expérimentale de coalescence de bulles dans les magmas hautement visqueux, ces données ont été essentielles pour comprendre les changements physiques induit par la décompression et la remontée souvent explosive de ces magmas. Cette étude, reproduite en Partie III, m'a mené à formuler les concepts de base à l'issue de mon activité actuelle, comme le lien entre la coalescence des bulles et la perméabilité d'un magma.

Mon post-doctorat à l'ISTO de 2004 à 2006 m'a permis de construire des modèles numériques couplant thermodynamique, chimie et concepts physiques de dynamique des fluides. Certains de ces modèles sont basés sur des données expérimentales (Burgisser et Scaillet, 2007; Burgisser et al., 2008; Annen et al., 2008), et d'autres sont centrés sur le dégazage magmatique durant des éruptions de dôme (VMFIX dans le projet ERC et le projet ANR EXPLANT, voir ci-dessous et Partie II). Le développement de ces modèles couplés m'a rendu sensible aux phénomènes hautement interdépendants qui ne peuvent être compris que par la combinaison de différentes disciplines.

Une étape clé de ma carrière est mon appropriation de la physique multiphasée, qui a pour objet d'étude l'écoulement de mixtures réactives de fluide et de particules. J'ai introduit des concepts fondamentaux de physique multiphasée à la communauté volcanologique, ce qui m'a permis d'établir une meilleure compréhension théorique du comportement des mixtures de gaz et de particules produites par le volcanisme explosif (Burgisser et Bergantz, 2002; Burgisser et al., 2003). J'ai également publié une contribution contenant des outils physiques permettant de mettre à l'échelle les

expériences de laboratoire visant à reproduire des systèmes magmatiques en mouvement (Burgisser et al., 2005). Cette contribution, incluse dans la Partie III, a été motivée par la réalisation que les travaux expérimentaux effectués durant les trente dernières années ne correspondent souvent pas au régime dynamique des systèmes naturels qu'il sont censés reproduire. J'ai récemment noté un nouveau dispositif expérimental prenant en compte les mises à l'échelle que nous avons proposées (Dellino et al., 2007, J. Geophys. Res. 112:B04202).

La physique multiphasée reste cependant très jeune: les expérimentalistes qui déterminent les lois constitutives des systèmes les plus simples, les modélisateurs qui assemblent ces lois dans des modèles numériques complexes aux propriétés émergentes et les volcanologues de terrain qui mesures ces propriétés n'ont pas toujours le langage commun permettant de confronter leurs découvertes. Ceci arrive trop souvent parce qu'un paramètre mesuré sur le terrain n'est pas directement comparable à celui mesuré en laboratoire. Ma tâche actuelle est de trouver ce langage commun en utilisant ma familiarité des approches de terrain, numériques et expérimentales.

Le dégazage magmatique est un cas typique où la physique multiphasée permet une avancée significative par rapport à l'état actuel des connaissances. En combinant des lois simples, comme la croissance d'une bulle ou la solubilité d'une espèce chimique, des propriétés nouvelles émergent des simulations numériques, comme la ségrégation des bulles dans un conduit volcanique. De telles propriétés émergentes sont souvent valides à de grandes échelles et peuvent parfois être testées dans les systèmes naturels.

Le projet ERC *Deciphering Eruptions by Modeling Outputs of Natural Systems* (DEMONS), dont j'assume la direction (2008-2012, voir Partie II), utilise précisément cette approche (Partie II). Ce projet propose de lier les processus magmatiques profonds avec les émissions de gaz en surface afin d'utiliser efficacement les analyses de gaz volcaniques dans la prévention des risques volcaniques et la quantification des flux géochimiques globaux. Ce but sera atteint grâce à une modélisation des cinétiques de dégazage dans un conduit volcanique utilisant une combinaison d'approches de terrain, expérimentales, et numériques. La thèse d'I. Molina, ma première responsabilité directoriale, tient une place centrale dans ce projet. Sa tâche principale est d'intégrer dans le modèle de conduit volcanique multiphasé VMFIX l'évolution de la chimie des gaz. Ce vaste objectif sera atteint par une focalisation sur deux volcans actifs aux comportements typiques et opposés (Montserrat et Erebus).

A l'origine du projet DEMONS, nous avons utilisé le principe des propriétés émergentes lors de la création d'un modèle chimique de dégazage en combinant des lois de solubilité simples contrôlées expérimentalement à des réactions chimiques bien connues (Burgisser et Scaillet, 2007 ; Burgisser et al., 2008). Ce modèle produit une évolution de la composition chimique des gaz exsolvés par la décompression d'une complexité inattendue (Partie III). Nous avons noté en particulier des changements dramatiques de l'état d'oxydation du magma qui remettaient en cause la vue conventionnelle d'un état d'oxydation constant durant une remontée magmatique. Ces changements ont des répercussions importantes dans d'autres domaines comme l'étude de la formation de l'atmosphère terrestre, dont la teneur en oxygène dépend fortement de l'état d'oxydation des gaz volcaniques émis.

La physique multiphasée a vocation à être appliquée à de nombreuses situations en Volcanologie. Le transfert de magma au sein de la croûte terrestre est un autre exemple où elle ouvre de nouvelles voies de recherche. Des avancées significatives peuvent être faites en établissant la quantité et la localisation de la portion mobile d'un magma par rapport à sa fraction trop cristallisée pour bouger car cela place des contraintes sur la taille maximale d'une éruption volcanique. Avec ce problème en tête, nous avons commencé par établir un cadre théorique de la remobilisation d'un magma hautement cristallisé (Bergantz and Burgisser, in prep.). Il est complété par des simulations de convection thermique dans des chambres magmatique hautement cristallisées basées sur la physique multiphasée, et une étude du bilan thermique d'une chambre magmatique long terme (Annen et al., 2008). Je développe ainsi activement cette nouvelle approche de volcanologie physique, et le projet ERC est une première étape dans la construction d'une équipe de recherche indépendante et dynamique.

Mon indépendance en tant que chercheur s'est initiée dès mon doctorat avec la publication de l'étude de terrain du volcan Okmok en tant que seul auteur (Burgisser, 2005, Partie III). Cette autonomie se traduit aujourd'hui en huit publications en tant que premier auteur sur un total de douze publications dans des revues internationales et une publication dans un compte-rendu de conférence avec comité de lecture. J'ai également construit mes deux projets de post-doctorat et le prestigieux projet européen DEMONS (Partie II). L'intervalle court entre ma première rencontre avec le petrologue expérimental B. Scaillet en 2005 et notre première publication commune dans Nature (Burgisser et Scaillet, 2007, Partie III) illustre ma capacité à collaborations productives avec des chercheurs partageant des objets d'étude similaires mais utilisant des approches fondamentalement différentes (p. ex. Pichavant et al., 2007 ; Annen et al., 2008).

Encadrement

La construction d'une équipe de recherche indépendante passe par ma prise en charge de doctorants et de post-doctorants. Cette prise de responsabilité s'est amorcée avec une publication sur la perméabilité des ponces volcaniques issue d'un co-encadrement de Master II (2005-2006, Bouvet de Maisonneuve et al., 2008). Mon suivi de C. Bouvet de Maisonneuve se poursuit durant sa thèse *Petrologic and numerical modeling study of Strombolian eruption dynamics at Llaima volcano (Chile)* (2007-2011, direction M. Dungan, Université de Genève, co-direction A. Burgisser et O. Bachmann, Université de Washington). La partie de modélisation numérique de cette thèse débutera à l'ISTO mi-2009 et utilisera le même modèle d'écoulement multiphasé que le projet DEMONS. Je participe également au co-encadrement de la thèse de W. Degruyter à l'Université de Genève *Understanding volcanic degassing through textural analysis and numerical modelling* (2006-2010, direction O. Bachmann, Université de Washington), qui se penche sur la fragmentation du magma lors d'éruptions explosives. Le premier volet de cette thèse a fait l'objet d'une publication (Degruyter et al., accepté).

Le projet DEMONS inclus, outre la thèse d'I. Molina, deux post-doctorants. J'ai engagé M. Alletti, jeune (thèse soutenue en 2008) post-doctorante depuis octobre 2008, et J. Castro, chercheur américain d'expérience (thèse soutenue en 1999) en mars 2009. Ces trois membres de mon équipe de recherche ont été sélectionnés par mes soins après avoir considéré des candidats au niveau international. I. Molina, avec 8 années d'expérience comme technicienne au Geophysical Institute Escuela

Politécnica Nacional à Quito (Equateur) et 3 publications dans des revues internationales, est déjà tout à son aise dans une équipe de volcanologie physique que j'espère dynamique et soudée.

Mon arrivée à l'ISTO fin 2004 m'a permis d'encadrer dans cet institut 2 étudiants de Master II, 4 étudiants Master I et deux stagiaires étrangers poursuivant un équivalent du Master I. A l'instar des doctorants, la plupart de ces étudiants ont contribué à faire progresser mes travaux sur le dégazage magmatique. Je co-encadre la thèse de l'un d'entre eux, L. Forestier Coste, depuis septembre 2008.

L. Forestier Coste a effectué ses Masters I et II en collaboration avec le laboratoire de Mathématiques Appliquées d'Orléans (MAPMO) sur l'*Analyse d'équation fluide-cinétiques pour un modèle d'éruption volcanique*. Il est maintenant lancé en thèse sur la prolongation de ces travaux, qui visent à implémenter un modèle mathématique et numérique de croissance et coalescence de bulles dans les magmas (2008-2011, codirection F. James & S. Mancini, MAPMO, co-encadrement A. Burgisser). Sur le même sujet mais utilisant une approche diamétralement opposée, une série d'expériences sur la coalescence des bulles dans les liquides rhyolitiques a été menée dans le cadre du Master II de A. Moussadji *Dégazage expérimental d'un magma rhyolitique* (2006, codirection C. Martel & A. Burgisser, ISTO).

Dans le cadre du projet EXPLANT (voir ci-dessous), je me suis intéressé aux textures cristallines et vésiculaires présentes dans les ponces vulcaniennes récoltées durant la campagne de terrain à Montserrat en juillet 2006 (Poussineau et al., in prep ; Burgisser et al., in prep.). Avec L. Arbaret (ISTO), j'ai codirigé 2 Master I ayant pour objet l'étude de ces textures : M. Queffurus, *Etude morphométrique et conditions de formation des fibres de verre dans les ponces de Soufrière Hills, île de Montserrat*, et T. Vergoz *Analyse de la distribution de taille des grains des faciès cataclastiques des ponces des éruptions vulcaniennes de 1997 de la Soufrière Hills de Montserrat*. Ces Masters ont étés soutenus en juin 2007. L. Arbaret et moi-même avons également codirigé les Master I et II de M. Forien sur l'*Etude expérimentale de la fragmentation cristalline dans les suspensions magmatiques concentrées.* Ces travaux sont en cours de valorisation dans Forien et al. (in prep.).

Finalement, j'ai organisé et supervisé les séjours à l'ISTO de Harshvardhan et M. Semwal, étudiants Master I de l'Indian Institute of Technology à Kharagpur en Inde. Durant 2 mois (juin-juillet 2006), Harshvardhan s'est occupé d'étendre le modèle de dégazage chimique afin d'inclure l'exsolution du carbone, alors que M. Semwal (juin-juillet 2008) a préparé le code du même modèle pour une distribution en open source.

Participation aux jury de thèse

L. Girolami (2008) *Dynamique et sédimentation des écoulements pyroclastiques reproduits en laboratoire*, co-encadrement par T. Druitt et O. Roche (Laboratoire Magmas et Volcans, Clermont-Ferrand.

Administration de la recherche

Dans la nouvelle organisation décidée pour le plan quadriennal de l'ISTO 2008-2011, j'occupe la position de responsable de projet (*Magmatologie physique*, 3.8 équivalent temps plein pour 8 chercheurs et enseignant-chercheurs). La mise en

place de cette organisation a débuté dès mars 2007. Ma recherche s'inscrit parfaitement dans ce projet d'équipe et ma spécialisation dans la modélisation est complémentaire de la dominante expérimentale du reste de l'équipe.

Je suis membre extérieur du comité de sélection de l'Université Blaise Pascal à Clermont-Ferrand depuis 2009.

Participation à des revues scientifiques et évaluation de projets

Je suis membre du comité éditorial du *Journal of Volcanology and Geothermal Research* depuis 2006 et rapporteur pour Science, Journal of Volcanology and Geothermal Research, Bulletin of Volcanology, Journal of Geophysical Research, Terra Nova, Geophysical Research Letters et l'Agence Nationale pour la Recherche.

Financements

Je termine un financement de l'Agence Nationale pour la Recherche pour un projet intitulé *Explosivité des dôme de lave – Le cas du volcanisme des Petites Antilles* (EXPLANT), Coordinatrice C. Martel (2006-2008, 350 k€ pour 4 chercheurs équivalent temps plein).

La suite de mes recherches est financée dans le cadre du projet ERC *Deciphering Eruptions by Modeling Outputs of Natural Systems* (DEMONS, 2008-2012, ERC Starting Grants, 1500 k€ pour 2 chercheurs équivalent temps plein).

Liste des publications

Acceptée

1. Degruyter W., Bachmann O., *Burgisser A.*, Masschaele B.,Cnudde V. (2009) The influence of shear across volcanic conduits: a case study of the Kos Plateau Tuff eruption (Aegean Arc), **Bulletin of Volcanology**.

Sous presse

2. Bouvet de Maisonneuve C., Bachmann O., *Burgisser A.* (2008) Characterization of juvenile pyroclasts from the Kos Plateau Tuff (Aegean Arc): insights into the eruptive dynamics of a large rhyolitic eruption, **Bulletin of Volcanology**.

Imprimées

3. Annen C., Pichavant M., Bachmann O., *Burgisser A.* (2008), Conditions for the growth of a long-lived shallow crustal magma chamber below Mount Pelee volcano (Martinique, Lesser Antilles Arc), **Journal of Geophysical Research** 113, B07209, doi:10.1029/2007JB005049

4. *Burgisser A.* (2005) Physical volcanology of the 2050 BP caldera-forming eruption of Okmok volcano, Alaska, **Bulletin of Volcanology**, v. 67, p. 497-525.

5. *Burgisser A.*, Bergantz G.W. (2002) Reconciling pyroclastic flow and surge: the multiphase physics of pyroclastic density currents, **Earth and Planetary Science Letters**, v. 202, p. 405-418.

6. *Burgisser A.*, Gardner J.E. (2006) Using hydraulic equivalences to discriminate transport processes of volcanic flows, **Geology**, v. 34, 157-160.

7. *Burgisser A.*, Scaillet B. (2007) Redox evolution of a degassing magma rising to the surface, **Nature**, v. 445, p.194-197.

8. *Burgisser A.*, Bergantz G.W., Breidenthal R. (2003) On the effects of Stokes, Richardson, and stability numbers in persistent and accelerating vortices, *in* Gyr, A. and Kinzelbach, W. (eds) Sedimentation and sediment transport, Proc. Monte Verita Symposium, Switzerland, p. 111-120.

9. *Burgisser A.*, Gardner J.E. (2005) Experimental constraints on degassing and permeability in volcanic conduit flow, **Bulletin of Volcanology**, v. 67, p. 42-56.

10. *Burgisser A.*, Bergantz G.W., Breidenthal R. (2005) Addressing complexity in laboratory experiments: the scaling of dilute multiphase flows in magmatic systems, **Journal of Volcanology and Geothermal Research**, v. 141, p. 245-265.

11. *Burgisser A.*, Scaillet B., Harshvardhan (2008) Chemical patterns of erupting silicic magmas and their influence on the amount of degassing during ascent, **Journal of Geophysical Research,** *in press***.**

12. Gardner J.E., *Burgisser A.*, Hort M., Rutherford M. (2006) Experimental and model constraints on degassing of magma during ascent, in Siebe C., Macias J.L., Aguirre-Diaz G.J. (Eds) Neogene-Quaternary continental margin volcanism: A perspective from Mexico. **Geological Society of America Bulletin Special Pape**r, v. 402, 99-114.

13. Gardner J.E., *Burgisser A.*, Stelling P. (2007) Eruption and deposition of the Fisher Tuff (Alaska): Evidence for the evolution of pyroclastic flows, **Journal of Geology** v. 115, p. 417-436.

14. Pichavant M., Costa F., Scaillet B. Poussineau S., Martel C., *Burgisser A.* (2007) Equilibration scales in silicic to intermediate magmas - Implications for experimental studies, **Journal of Petrology**, v.48, p. 1955-1972.

Partie II

Projet de recherche
Deciphering Eruptions by Modeling Outputs of Natural Systems

financé par

European Research Council

"Ideas" Specific programme

Starting Grant

State-of-the-art and objectives

Active volcanoes emit high temperature gases that modify the chemical imbalance of the Earth's atmosphere. For instance, the SO_2 contained in volcanic plumes can damage ecosystems [13], change the radiative balance of the atmosphere and thus cause global climate change [14]. Numerous volcanic gases affect the Earth's climate; even water vapor contributes to ozone depletion if injected directly at high altitude [15]. It is thus crucial to be able to quantify the contribution and impact of volcanogenic gases on the atmosphere so that the global atmospheric effects of a major eruption can be predicted and so that volcanic gases can be discriminated from anthropogenic emissions.

At the scale of one volcano, monitoring of gas plumes is a major tool in volcanic risk management [16,17]. Volcanologists have long noted that not only the chemical composition of the gases emitted at the vent during eruptions varies widely from volcano to volcano, but also that it often changes during the course of a single eruption [16]. In parallel, recent progress in experimental petrology has allowed calculation of the gas composition that is in equilibrium with a given magma at depth [18]**.** When, however, the calculated gas composition at depth is compared to that measured at the surface, a general disagreement arises (Fig. 1). Various explanations have been proposed [19], but there are currently no tools to solve this discrepancy. Another problem is the decoupling between degassing flux and magmatic flux (Fig. 1). There seems to be no simple link between the amount of gas emitted and the volume of magma erupted, which makes any geochemical balance uncertain at best. Finally, it is currently impossible to determine whether a gas plume is generated in response to passive degassing of magma, to its crystallization, or to its ascent [20]. It is a serious drawback as these processes lead to opposite consequences on the volcanic activity.

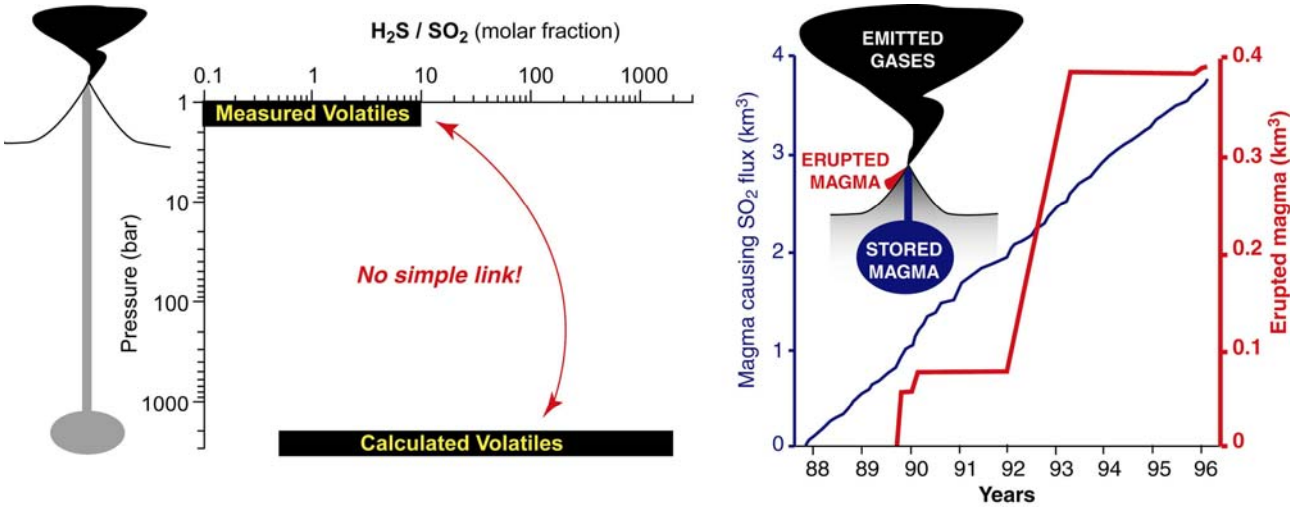

Figure 1: Influence of conduit processes on volcanic gas emission. **Right.** Absence of correlation between gas composition calculated from the lavas and those measured at vent [1]. **Left.** At Etna, large contrast between cumulative volume of magma producing the degassing (left axis) and the cumulative volume actually erupted (right axis) [21]. Degassed magma is calculated from the SO_2 flux measured at the vent.

Such difficulties are mainly due to the fact that the interplay between the various degassing mechanisms and gas chemistry has barely been addressed. As a result, the vast amount of gas measurements collected through the years remains grossly under-exploited. Although since the work by Sparks [22], there have been many studies focused on exsolution of bubbles, modeling efforts of degassing mainly focused on the physics of the phenomenon [e.g., 4,23]. Despite these efforts, the uncertainty remaining on the degassing mechanism is alarmingly high: we showed that conservative degassing processes produce 10^3 times less gas than more radical ones [3].

A trans-disciplinary approach to degassing. To efficiently use volcanic gas analysis for the global geochemical fluxes and for the mitigation of volcanic risks, we propose to link deep magmatic processes with emissions at the surface. Our objective is to calculate the quantity and composition of volcanic gases as a function of the petrology of the magma at depth and the eruptive regime, and compare those calculations with actual measures of plumes at active volcanoes. We will achieve that by *modeling the chemical kinetics of degassing in a volcanic conduit by using a combination of experimental, mathematical, field, and numerical approaches*.

More chemical species, phases, and dimensions. Previously, the few models evaluating the effect of the chemistry of degassing on magma ascent used partial gaseous mixtures that only contain a few chemical species of a given system, such as CO_2-H_2O [e.g., 24]. Our work showed that all volatile species must be considered when performing such a calculation [1]. Our thermodynamic approach is unique because the simulation is only determined by the chemical composition at depth. This method minimizes the degrees of freedom and allows for the emergence of new behavior induced by the coupling between physics and chemistry. The model we will develop during this project, Volcanic Multiphase Flow with Interphase eXchange (VMFIX), is the first attempt in taking into account degassing kinetics of all relevant chemical species to quantify the flux and composition of volcanic gases expelled by volcanoes. Only two of the 19 conduit flow models focused on the physics of magma ascent [25] are 2D, including an early version of VMFIX [26], and all of them treat magma as a homogeneous mixture. VMFIX is the first 3D multiphase model allowing differential motion of melt and bubbles, which will extend its applicability from Plinian eruptions to dome-forming, passive degassing, Strombolian, and Vulcanian regimes.

Which species for which volcano? Volcanic gas sensing is a rapidly advancing field where ways of detecting new chemical species are regularly found. There is, however, not a perfect adequacy between species measured by volcanic gas sensing and the ones that VMFIX will simulate. The development of our chemical model in VMFIX is thus inescapably linked to new data collection at active volcanoes. Our approach is to link eruptive dynamics to plume composition at two reference volcanoes at which crucial chemical species can be best measured. The first target is Erebus volcano (Antarctica), which has a passively degassing lava lake, and the second target is Soufrière Hills volcano (Montserrat, W.I.), which has a growing lava dome. The optimized match between modeled and measured species will maximize the constraints available to confront VMFIX simulations with field data.

A significant advance for hazard mitigation. The development of high permeability within the magma promotes efficient degassing and the magma erupts effusively, often forming a lava dome. A low permeability, however, causes bubbles to accumulate and their sudden disruption yields an explosive eruption. Our results on

the development of permeability in magmas and their integration in VMFIX are thus instrumental in understanding the transition between effusive and explosive regimes. Only a model integrating degassing kinetics and chemistry can predict the geochemical signature of a crystallizing magma from a decompressing one and determine the composition of gases emitted during an eruptive cycle or between different eruptions. We expect VMFIX to give the mass flux and chemical composition of the plume as a function of time for various eruptive regimes, thus opening the door to inverse modeling of volcanic gas monitoring. Such results could also be used as input for the numerical models of atmospheric dispersion of volcanic plumes to better estimate the short to long term impacts of volcanic gas on the Earth's atmosphere [27].

Methodology

Part #1: Integrated physical and chemical conduit flow model.

Physics. A robust knowledge of the physical processes at play in volcanic conduits is necessary to relate volcanic gas analyses to eruptive regime. I developed the numerical model Volcanic Multiphase Flow with Interphase eXchange (VMFIX), which considers magma as a multiphase mixture of bubbles and silicate liquid with independent motions, and is based on the generic solver MFIX (www.mfix.org). In VMFIX, both the silicate melt and the gas phase are treated in 3D with the Navier-Stokes equations. Magma fragmentation is handled by a change in the stress tensor of each phase so as to switch from bubbly liquid to dusty gas. Degassing is simulated by growth laws ruling H_2O bubbles [28]. Bubble coalescence can be simulated by changing the bubble density number, and permeability can be simulated by changing the drag between melt and gas. Although a proof of principle has been carried out with simplistic laws (e.g., constant coalescence rate), none of these two processes can be operational before VMFIX incorporates the way the bubbles connect and lose their gas (Part #2). Heat transfer effects are also taken in account, so that simulation of thermal convection can be carried out with up to 40% crystals (Part #3).

Chemistry. Our chemical model of degassing is based on the substantial dataset of internally consistent measures of volatile solubilities at the ISTO. Currently, this thermodynamic model allows us to calculate the evolution of the volatile composition during decompression for the S-O-H-C-Fe system [1,2,29]. To carry out comparisons with field measurements of volcanic plumes, halogens (F, Cl, Br) need to be added to our model. Because solubility laws of halogens in silicate melts are not known for magmatic conditions, we will perform laboratory experiments to define the relevant fugacity-concentration relationships. We anticipate that results from monitoring (Part #3) will drive us to determine experimentally solubilities of a couple of additional species.

Model integration. The chemistry calculations are currently carried out in equilibrium and are based on a 1D, homogeneous conduit flow model assuming closed system. This formulation strongly impedes the implementation of permeability. We will overcome this limitation by transferring the chemical model to 3D, non-homogeneous VMFIX. We will relax the equilibrium assumption and replace it by degassing kinetics, which will be implemented using published results of diffusion experiments [e.g., 30]. When necessary, additional diffusion experiments will be carried out. For each computational cell, the integrated model will calculate the amount of volatiles that needs to be exchanged between melt and gas. The current version of VMFIX treats bubble growth precisely that way. Integrating the chemical model into VMFIX is thus a challenging but realistic goal.

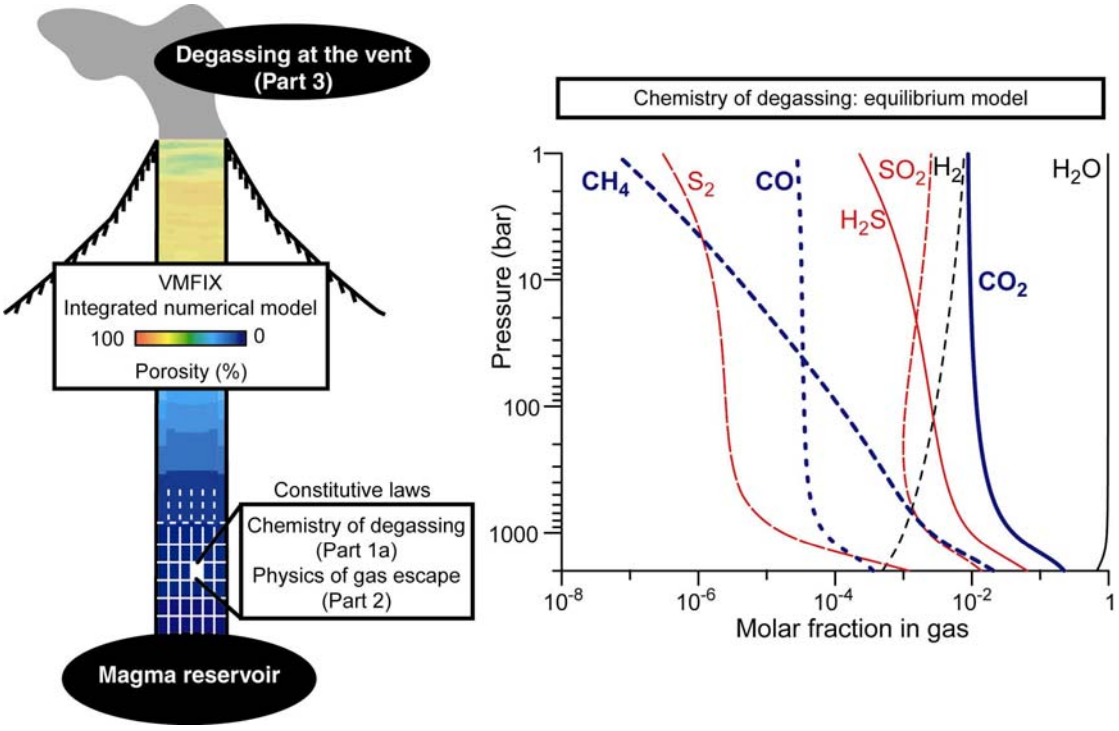

Figure 2: Towards an integrated model of magma degassing. **Left.** Sample output from the multiphase conduit flow model VMFIX along a 4-km long, 24-m wide conduit (exaggerated vertical scale). This 2D run shows the evolution of porosity during ascent. The integration of the chemical model and the physical model of gas escape will be done for each computational cell, as shown on the schematic numerical grid. **Right.** Typical chemistry calculation at equilibrium showing the complex evolution of gas composition during decompression [2]. The rhyolitic melt started decompressing at conditions close to those at Mt. St. Helens during the 1980 eruptions (little excess gas, 825°C ΔNNO+1, 113 ppm S and 522 ppm CO_2 in the melt).

Part #2: Gas escape by bubble coalescence and permeability

To correctly describe how bubble coalesce and create a permeable network from which gas can escape, two sets of decompression experiments are necessary. In the *first set*, the time for newly paired bubbles to relax back to a sphere is short compared to the time until a new coalescence occurs. Our methodology causes samples to develop various degrees of coalescence [4,31,32]. We will carry out decompression time series with various initial conditions (melt viscosity, etc.) to complete our baseline dataset for mathematical modeling of coalescence. The statistical evolution of the bubbles sizes and their coalescence will be described by kinetic modeling [33]. This mathematical model describes the evolution of the distribution function of bubbles in time and volume, and takes into account both growth and coalescence effects. The growth rate is linked to

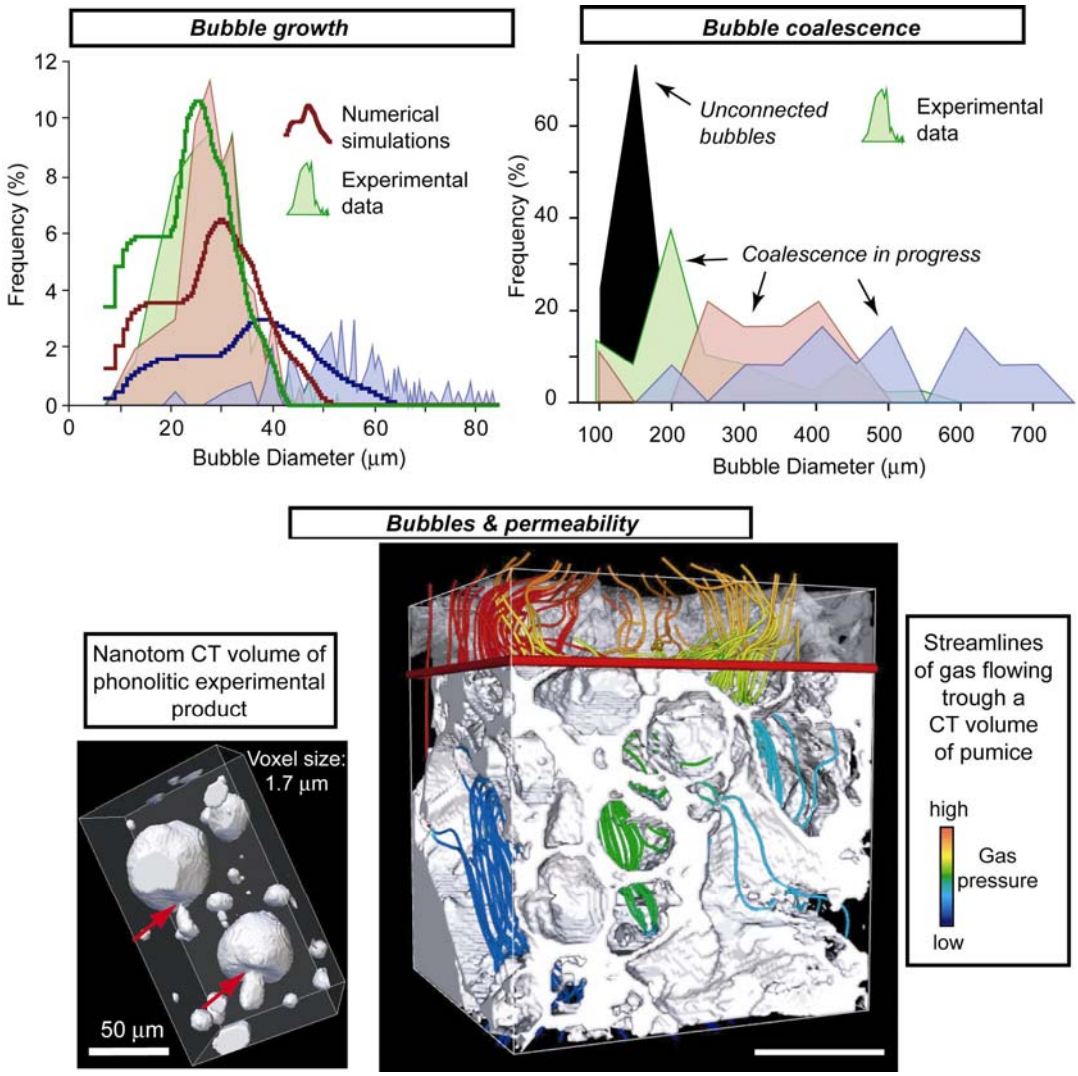

Figure 3: Unraveling the mechanisms of gas escape. **Top.** Kinetic modeling of bubble growth and coalescence so as to follow the evolution of bubble size distribution. Experiments started at 150 MPa and decompressed at different final pressure. Without coalescence (left), bubbles grow in equilibrium according to well-know laws that we integrated into the kinetic model (curves, [34]). With an experimental setup allowing coalescence to occur (right), size distributions become wider as coalescence affects only some bubbles, making them larger and larger (from [4]). **Bottom.** Modeling fluid flow through 3D volumes reconstructed by X-Ray Computed microTomography (CT). The rendered volume on the right is used a base mesh for a numerical model of fluid flow. The top part has been removed to show gas streamlines. Densely packed streamlines represent regions of preferred flowage and allow for permeability determination. The left volume shows bubble coalescence in a phonolite produced at the experimental petrology laboratory of ISTO. The volume, which shows distinctly 2 pairs of connected bubbles (red arrows), was obtained with the Nanotom we propose to acquire.

the distribution function itself, and will be expressed following a well-known bubble growth law [28] calibrated to fit previous experimental data [4]. In a first approximation, we consider that the coalescence phenomenon consists of binary instantaneous collisions between bubbles where the collision rate will be determined by fitting experimental results. The coalescence kernel in [33] is based on the relative motion of one bubble relative to another. While this is relevant for low viscosity magmas such as phonolite, it is not applicable to the viscous, rhyolitic magmas we also use in our experiments, because bubbles do not move relative to each other over

the duration of an experiment. Thus, the viscous kernel has to be determined by successive trial of physical laws against experimental data such as in Fig. 3. We have shown that this method is able to discriminate between equilibrium and disequilibrium bubble growth [34], and we are confident it can be applied to coalescence because causing a significant spread of bubble sizes. Preliminary data suggest the coalescence kernel will most likely depend on time and bubble size, but we will also attempt a more detailed modeling by introducing other collision kernels that take account of differential growth [35] and Ostwald ripening [36]. Once the evolution of the bubble size distribution has been computed, we can find the average bubble size, which is used by VMFIX to calculate the drag between the gas phase and the melt. Thus, by introducing the evolution of the distribution function into VMFIX, we will simulate the progression of coalescence at each computational cell.

In the *second experimental set*, newly coalesced bubbles do not relax immediately to spheres, thus forming a connected, permeable network [4,32]. Our goal is to determine what the controls of network formation and collapse are (bubble number density, melt viscosity, time, etc.). Essential parameters quantifying bubble connectivity (size, shape, and orientation distribution of the bubbles and their connections) are only accessible through 3D measurements. We thus will analyze our experimental products by high-resolution, X-Ray microtomography, which acquires a 3D direct image of samples and the objects they contain (bubbles, crystals, glass; Fig. 3). This ability to distinguish between the major phases of igneous rocks put microtomography at the forefront of current 3D analytical techniques [37]. It was first applied to volcanic rocks to quantify the shape and size distribution of crystals [38] and bubbles [39,40]. Tomographic analyses are nondestructive, which allow for further analyses (e.g., volatile content). Using 3D fluid flow modeling based on the microtomographic images, we successfully calculated the permeability of experimental samples [41, see also 42], where traditional gas permeameters fail because of the small sample size. We use the volume obtained by microtomography as boundary condition: the model calculates the fluid flow within the connected bubbles by solving the full 3D Navier-Stokes equations (Fig. 3). When a pressure difference is applied across the volume, the model determines the way the fluid flows towards the low-pressure region. The porous network formed by the connected bubbles opposes a resistance to the flowage, slowing the fluid down. The magnitude of this resistance can be converted to a permeability value.

We will collect data from 3D analyses (sample permeability and tortuosity, size and distribution of bubble connections) in order to establish laws of permeability development. Although empirical laws can doubtlessly be drawn from such data, we will attempt a mechanistic approach by deriving physics-based laws based on our kinetic model of coalescence so as to encompass both low- and high-viscosity magmas. We will start this approach by extending the coalescence model in order to make the difference between isolated bubbles with a given volume, and chains of smaller bubbles with the same total volume. These two kind of bubbles, as shown by experiences, evolve differentely, and, in particular, the second one is responsible for permeability [32]. Such development will allow the kinetic model to track the evolution of the bubble population responsible for gas escape. The mathematical analysis of such collisional kinetic model has made important breakthroughs in recent years [43], as well as for the design of efficient and robust numerical methods. Within this project, we will have to couple these numerical schemes with the magma flux computed by VMFIX. We will apply such advances to predict, using numerical simulations, the evolution of connected bubbles during

decompression, and so to obtain information about the permeability of magmas. These numerical results will quantify the gas fraction lost by the magma at each VMFIX cell.

Part #3: Volatile content of plumes at active volcanoes

We propose to collect new observations at two active volcanoes to build understanding of key manifestations of magma degassing and its links to eruptive style. Target volcanoes represent canonical cases of eruptive regimes with a long-standing activity: passive degassing with regular Strombolian explosions of low-viscosity magma at Erebus, and slow dome growth with occasional Vulcanian eruptions of high-viscosity magma at Soufrière Hills volcano.

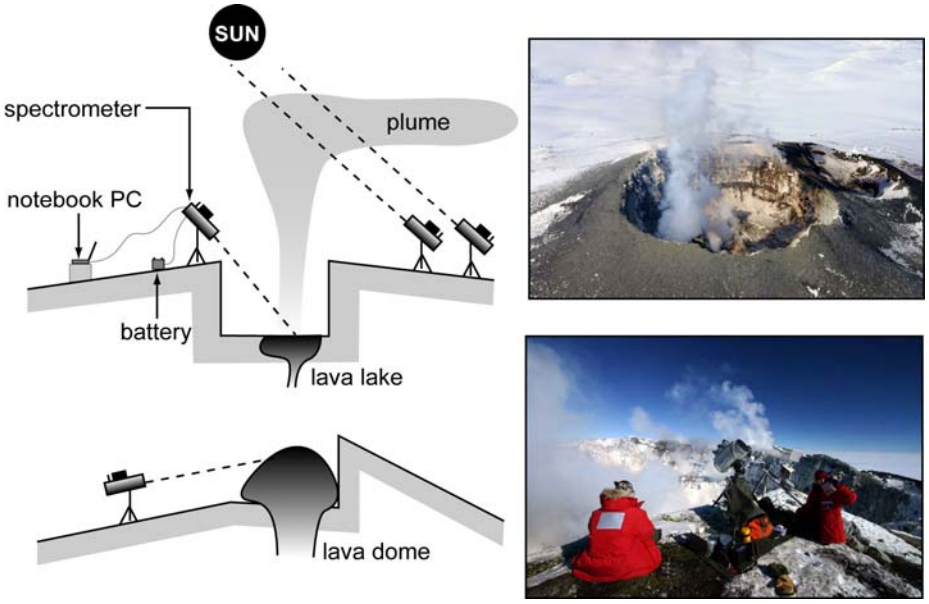

Figure 4: Measuring gas composition at active volcanoes. **Left.** Examples of spectrometer setups to acquire gas composition as time series (single OP-FTIR instrument) or as fluxes (coupled UV instruments). Time series setup uses hot lava from the lake at Erebus and from the dome at Montserrat as IR source. Flux setup with two parallel spectrometers uses the sun as light source. **Right.** Summit crater of Erebus, into which the lava lake is nested, and OP-FTIR sensor set at the rim, pointing downward at the lake to acquire gas composition.

Erebus has a phonolite lava lake active since 1972, and its exceptional setting (high altitude, low humidity and pollutant-free atmosphere) ensures a collection of unique, high-quality data of over nine gas species, including H_2O. Ability to measure water vapor is critical because at many volcanoes it represents >90 wt% of the volatiles expelled. A special effort will be made to measure the species handled by our model, (e.g., CH_4). Erebus' lava has a chemical composition similar to that of Vesuvius, upon which our thermodynamic model is based. We propose a field recording of the chemistry of Erebus plume by open-path Fourier-Transform InfraRed (OP-FTIR) spectroscopy (Fig. 4). In the rapidly advancing field of volcanic gas measurements, OP-FTIR has a special place because of the number of chemical species measured simultaneously with a high temporal resolution [44-46]. Since his first measurements at Etna in 1994, C. Oppenheimer has used OP-FTIR to successfully acquire data at Erebus [47,48], Soufrière Hills (see below), Vulcano, Stromboli, and Masaya. A new recording technique based on two-point ultraviolet (UV) spectroscopic measurements will allow us to retrieve fluxes of all volatile species measured in the infrared at high temporal resolution (about 1 s) [47]. The current spectrometer is able to collect data

for periods of up to about 10 hours, which is insufficient to address longer term changes in activity. We thus will develop a new spectroscopic system that can work over weeks to months under challenging Antarctic conditions. This requires, in particular, a low power consumption FTIR spectrometer. These chemical data will be combined with measures of the surface velocities of the lava lake with a Forward-Looking InfraRed (FLIR) camera, and lidar observations of lake level. Velocities are essential dynamical constraints on the convective state of the lake, against which VMFIX outputs will be tested.

Active since 1995, *Soufrière Hills*' lava dome has resumed growth in 2006, and, at the time of writing, the dome is second to largest since the beginning of the eruption. Ten years of studies harvested essential data for modeling with VMFIX, such as pre-eruptive conditions and conduit geometry from seismic data. As for Erebus, we propose a field recording of the plume chemistry by OP-FTIR during a time of steady dome growth, combined with measures of growth rate using the FLIR camera and traditional photogrammetry. Here, the goal is to build on the gas data already collected by the Montserrat Volcano Observatory (SO_2, Cl) and the Cambridge group [49-53] by adding the chemical species relevant to modeling. This requires a careful risk assessment for the proposed fieldwork and a few clear days. At an active volcano such as Soufrière Hills, such requirements cannot be scheduled precisely, but we expect suitable conditions to occur within the project duration. Although dome growth has stopped since May 2007, SO_2 degassing occurs at a rate similar to that of the long-term average. Such repose periods have happened several times during the eruption, and the imposing size of the current dome makes it prone to failure, as suggested by the smaller size of practically all preserved volcanic domes of similar composition. We thus allowed for flexible fieldwork durations and dates in order to guarantee sufficient data collection.

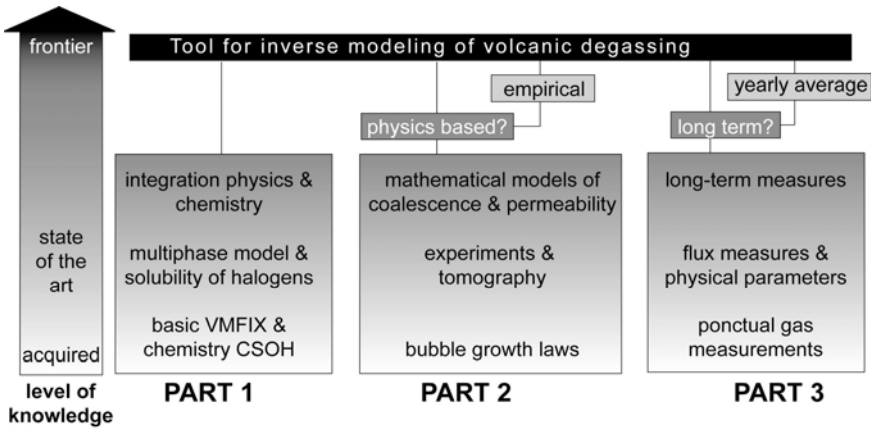

Figure 5: Key scientific tasks of the project and their relationship to current scientific knowledge.

Advancing Volcanology. DEMONS comprises three complementary parts that each start from sound previous work and that each involve state-of-the-art techniques (Fig. 5). Although each part will further our knowledge on degassing, it is the combination of these parts into a common framework that will bring us significantly beyond the state of the art, opening the possibility of true inverse modeling of volcanic gas data, which would contribute tremendously to volcanic hazard assessment and risk management. Part #2 and #3 include especially challenging tasks, as no current theory links coalescence and permeability, and long-term use of delicate optical instruments in harsh environments is inherently risky. In each case we have alternative solutions (empirical permeability laws and yearly averages of gas composition, respectively)

that still allow the integrated model to be completed without restricting much its applicable range. In summary, bringing together experimental work, numerical models, and field data into an integrated study of magma degassing at two end member volcanoes is the only way to believably link plume chemistry to eruptive dynamics [54].

Resources

In order to achieve the project's goals, the team will be composed of three contributing researchers and myself. We request funding to hire two Ph.D. students and one post-doc fellow for 3 years each, all under my supervision. All forecasted experimental work will use ISTO facilities such as autoclaves and micro-analysis techniques.

Part #1 *(A. Burgisser 40%, B. Scaillet 10%, 1 PhD, 1 PostDoc)*. The quantitative approach of degassing processes needs a deep knowledge of solubility laws of volatiles and their relationship to the P-T-X evolution of magmas. B. Scaillet is a specialist on volatiles in magmas and experimental petrology. Author of about 60 publications, he has developed solubility models of species commonly used in volcano monitoring, in particular sulfur. A PostDoc will be focused on halogens solubility experiments and the associated thermodynamic modeling. Models based on multiphase physics are inherently complex, and integrating chemical reactions into VMFIX is a challenging task, to which a Ph.D. thesis will be devoted. In the current configuration (SMP compilation on a bi-Xeon 3.2 GHz, 4Gb RAM station), VMFIX completes a 2D simulation in about 20h of calculation. The chemical model is currently not parallelized and can perform a typical degassing calculation in ~3 hours on a single processor machine (Xeon 3.2 GHz). Thus, the addition of the chemical model and the extension to 3D will considerably lengthen the computing time, making multiple runs problematic and parametric studies impractical in the current computer configuration. Both changes, however, can take full advantage of parallelization. VMFIX includes a DMP implementation and the original solver MFIX runs on many lab-size clusters. Its adaptation to a new cluster is thus a straightforward task. The chemical model can be parsed into VMFIX so that each computation cell performs its own chemical calculations. These arguments motivate us to ask for a 100 processors cluster with 100 Gb of memory. The multiprocessor architecture will speed up VMFIX calculations so that runs can be completed in a reasonable amount of time. Our determination, as a young team of researcher, to quickly achieve scientific independence is consistent with acquiring a cluster that is readily accessible to each team member. Other projects lead by the team members will take advantage of this cluster (Part #2 and thermal modeling of magma chamber).

Part #2 *(A. Burgisser 40%, S. Mancini 30%, 1 Postdoc)*. Mathematical modeling of coalescence is an arduous problem that is asking for a specialist of kinetic theory. S. Mancini has recently contributed to develop kinetic modeling in the medical domain [55,56]. She is from the Applied Mathematics (MAPMO) laboratory at the University of Orléans and started to collaborate with myself by co-supervising a Master I thesis on the numerical resolution of kinetic equations describing bubble growth and coalescence ([34], Fig. 3). She and I plan to co-supervise two Master II students and a PhD student on the numerical resolution of the kinetic equation. Decompression experiments and their analysis by microtomography will be conducted by the post-doc fellow. We also request funding for a laboratory microtomograph. In 2006 J. Gardner and I carried out feasibility tests on experimental pumice at the University of Texas at

Austin with their custom-built microtomograph (10 μm resolution). The processing of the tomographic volumes indicated that the porous network is formed by bubbles connected by apertures systematically larger than 20 μm, although submicron resolution, 2D SEM images suggested smaller apertures of 10 to 20 μm. Connections were thus sparsely represented by a couple of voxels in the tomographic volume, which proved to be insufficient to perform statistical analysis of their size and spatial distribution. This limitation drove us to carry further tests at the Swiss Light Source (SLS) at the Paul Scherrer Institute on natural pumice from Montserrat. The high quality images at the state-of-the-art resolution of 0.3 μm convinced us to work with a minimum resolution of 1 μm. We thus selected a laboratory-sized microtomograph able to reach such a precision and, unlike synchrotron-based tomography, immediately accessible. This last point is fundamental to carry out routine analysis of coalescence experiments, for which results from a given experiment give the initial conditions for the next experiment. It will also allow us to better select a few samples to analyze by synchrotron with a submicron resolution (SLS, European Synchrotron Radiation Facility or SOLEIL). Such small-scale analyses could address specific problems, such as the breakage of bubble walls, which are typically <2 μm. Since early 2006, the society Phoenix/XRay proposes the microtomograph Nanotom, the theoretical resolution of which is 0.5 μm (www.phoenix-xray.com/en/products/nanotom/nanotom.html). It can thus obtain images of objects between a few mm^3 and a few cm^3, which is appropriate for experimental products. In the framework of our negotiations with Phoenix/XRay, we lent samples for analysis with the Nanotom (Fig. 3). Our goal was real condition testing of the resolution and the power of the XRay source, which controls the contrast between the various phases present in the samples. These tests showed that a 1.5-μm resolution could be achieved by the Nanotom with an excellent phase contrast (see also Fig. 3). The Nanotom thus represents, to this date, the laboratory apparatus on the market the most appropriate for the analysis of our samples. Simulating fluid flow in the tomographic volumes to retrieve permeability is also a computer-intensive task. Currently, simulations take place on the same bi-processor machine as VMFIX and are limited to small volumes of 125^3 voxels (compared to typical image sizes $>1000^3$ voxels) because of the modest amount of memory available. Such a small volume is source of problems because magma is a porous media where large voids are interconnected by small connections. The cluster would allow for the simulation of the full tomographic volume, ensuring more representative permeabilities. The fluid flow model is also based on MFIX, making its adaptation to the new cluster easy.

Part #3 *(C. Oppenheimer 50%, A. Burgisser 10%).* C. Oppenheimer is a specialist in volcanic degassing, in particular in the field of data acquisition using ground-based techniques such as OP-FTIR and UV spectroscopy (www.plinian.com). Author of >100 publications, he is involved in monitoring Erebus in the framework of a NSF (USA) project until 2010. NSF funds expenses related to logistics at Erebus, but we request complementary funding for a new low power and Ethernet-ready OP-FTIR system (long-term power supplied and coupled sensors for flux measures), gear shipping, and travel. Both he and I have carried out field studies at Soufrière Hills, for which we request funds for two field campaigns of a month each. Four people will take part in each trip, including a PhD or post-doc, and we will deploy the instruments with a budgeted 5 days of helicopter support.

Project schedule

In Part #1, the work on halogen solubility can readily be started by the first PostDoc student. The PhD student will start six months later, so that the computer cluster can be ordered and installed beforehand. In Part #2, the post-doc fellow will start immediately by synthesizing existing data on coalescence and carry out additional experiments. There will be 6 months delay between ordering the microtomograph and its delivery at the ISTO. Taking in account installation time, we plan on having the machine operational by the end of Year 1 (latest by mid-Year 2), so that the post-doc fellow can analyze experimental products. Mathematical laws of coalescence will be developed during the whole duration of the project, being regularly fed by new experimental data. Empirical laws will be first built to be integrated into VMFIX, more physical laws probably taking longer to establish. Fieldwork on Erebus can only occur during the short Austral summer season and can thus be readily scheduled. Fieldwork on Montserrat, on the other hand, depends on prevailing activity of Soufrière Hills Volcano. We thus plan for two one-month periods of work during the four year project timeframe. Meetings with all participants will be held at the end of each field mission for fine-tuning of research planning and management. In parallel with this, C. Oppenheimer is planning a one-year sabbatical at ISTO, for which a proposal has been submitted at Région Centre (Le Studium) early in 2008. At the moment, preference is for the sabbatical to occur during Year 2, although postponing it by one year remains possible.

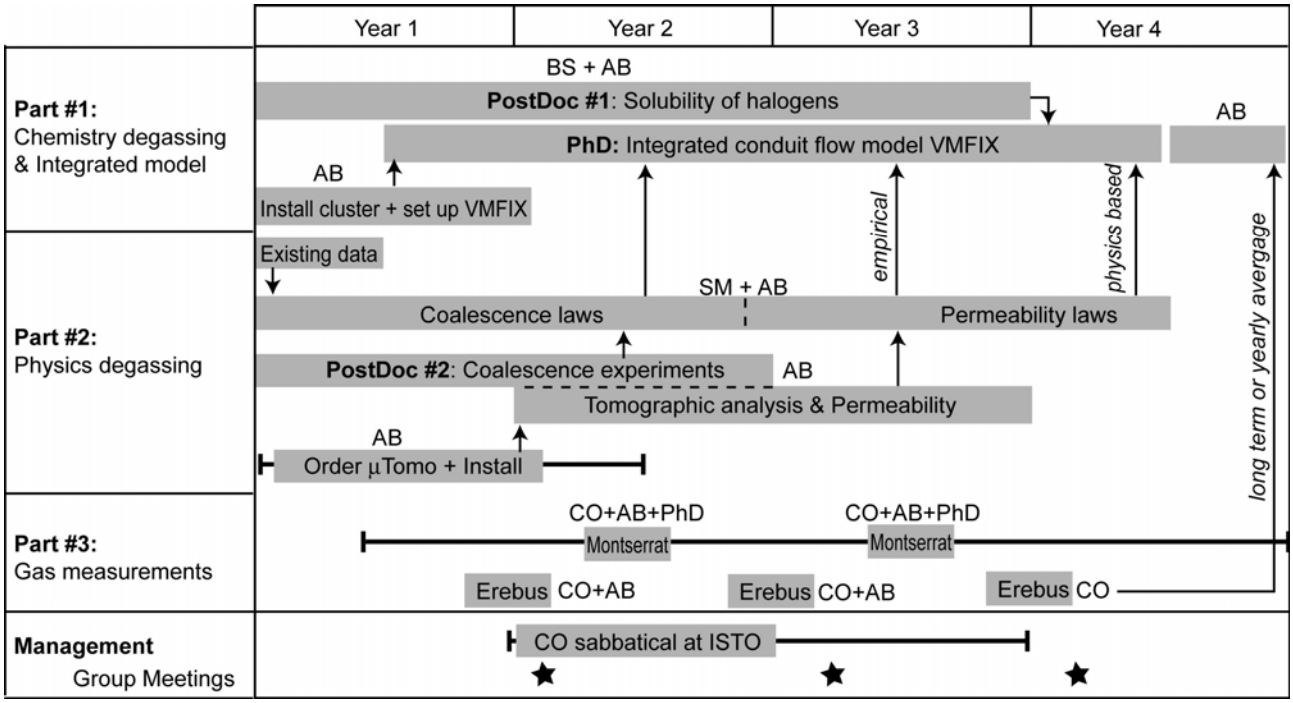

AB: A. Burgisser, **BS**: B. Scaillet; **SM**: S. Mancini, **CO**: C. Oppenheimer

References

1. Burgisser A, Scaillet B (2007) Nature 445:194-197.
2. Burgisser A et al (2008) J. Geophys. Res.,
3. Gardner JE et al (2006) in Siebe C et al (eds) Geol. Soc. Am. Bull. Spec. Paper 402:99-114.
4. Burgisser A, Gardner JE (2005) Bull. Volcanol. 67:42-56.
5. Annen C et al (2008) J. Geophys. Res., accepted.
6. Pichavant M et al (2007) J. Petrology,
7. Gardner JE et al (2007) J. Geology 115:417-436.
8. Burgisser A, Gardner JE (2006) Geology 34:157-160.
9. Burgisser A et al (2005) J. Volcanol. Geotherm. Res. 141:245-265.
10. Burgisser A (2005) Bull. Volcanol. 67:497-525.
11. Burgisser A et al (2003) in Gyr, A. and Kinzelbach, W. (eds), Proc. Monte Verita Symposium, Switzerland, 111-120.
12. Burgisser A, Bergantz GW (2002) Earth Planet, Sci, Lett, 202 : 405-418.
13. Demelle P (2003) Geol. Soc. Spec. Pub. 213:381-399.
14. Robock A (2000) Rev. Geophys. 38:191-219.
15. Solomon S et al (1996) J. Geophys. Res. 101:6713-6727.
16. Symonds RB et al. (1994) Rev. Mineral. 30:1-66.
17. Young SR et al (2003) Geol. Soc. Spec. Pub. 213:219-230.
18. Scaillet B, Pichavant M (2003) Geol Soc. Spec. Pub. 213:23-52.
19. Wallace PJ (2005) J. Volcanol. Geotherm. Res. 140:217-240.
20. Oppenheimer C et al. (2004) Geology 32:509-512.
21. Bruno N et al (1999) Bull. Volcanol.60:405-411.
22. Sparks RSJ (1978) J. Volcanol. Geotherm. Res. 3:1-37.
23. Gonnermann HM, Manga M (2007) Ann. Rev. Fluid Mech. 39:321-356.
24. Papale P, Polacci M (1999) Bull. Volcanol. 60:583-594.
25. Sahagian D (2005) J. Volcanol. Geotherm. Res. 143:1-15.
26. Dufek J, Bergantz GW (2005) J. Volcanol. Geotherm. Res. 141:113-132.
27. Textor C et al (2003) Geol. Soc. Spec. Pub. 213:307-328.
28. Lensky NG et al (2004) J. Volcanol. Geotherm. Res. 129:7-22.
29. Burgisser A et al (2006) Eos Trans. AGU 87 Fall Meet. Suppl., Abstr. V32C-02.
30. Watson EB (1994) Rev. Mineral. 30:371-411
31. Moussadji AB (2006) Mémoire Master II, Univ. Orléans 40 p.
32. Gardner JE (2007) J. Volcanol. Geotherm. Res. in press.
33. Lovejoy S et al (2004) J. Geophys Res 109:B11203
34. Forestier Coste L (2007) Mémoire Master I, Univ. Orléans 36 p.
35. Larsen JF, Gardner JE (2000) Earth Planet. Sci. Lett. 180:201-214
36. Larsen JF et al (2004) Geochim. Cosmochim. Acta 68:333-344.
37. Jerram DA, Higgins MD (2007) Elements 3:239-245.
38. Gualda GAR, Rivers M. (2006) J. Volcanol. Geotherm. Res. 154:48-62.
39. Song S-R et al (2001) Bull.Volcanol. 63:252-263.
40. Shin H et al (2005) Comput. & Geosci. 31:473-487.
41. Burgisser A et al (2006) EGU Gen. Ass. Abstr.
42. Wright HMN et al (2006) Geophys. Res. Lett. 33:L17316.
43. Escobedo M et al (2004) Comm. Math. Phys. 246:237-267.
44. Burton M et al (2007) Science 317:227-230.
45. Edmonds M, Gerlach TM (2007) Geology 35:751-754.
46. Aiuppa et al (2007) Geology, in press.
47. Oppenheimer C et al (2005) Atm. Environ. 39:6000-6006.

48. Oppenheimer C, Kyle PR (2007) J. Volcanol. Geotherm. Res. in press.
49. Edmonds M et al (2002) Bull. Volcanol. 64:21-30.
50. Edmonds M et al (2003) Bull. Volcanol. 65:578-586.
51. Edmonds M et al (2003) J. Volcanol. Geotherm. Res. 124:23-43.
52. Edmonds M. et al (2001) Earth Planet. Sci. Lett. 186:159-173.
53. Oppenheimer C et al (2002) Geol. Soc. London Memoir 21:621-639.
54. Wallace PJ et al (2003) EOS Trans. AGU 84:441-456.
55. Feita C et al (2005) Comput. Methods Biomech. Biomed. Eng. 8:279-293.
56. Baranger C et al (2005) ESAIM Proceed. CEMRACS 2004, 14:41-47.

Transition to independence

Equipment funded by this grant will allow me to address in the near future other critical problems in volcanology that ask for a similar multiphase approach, such as thermal convection in crystallizing magma chambers and dynamics of magma mixing. Results from deformation experiments on crystallized magmas carried out with a specially fitted Paterson press at ISTO are already opening new horizons on multiphase modeling of dense suspension in high-viscosity melts. The cluster is consistent with the creation of a young team under my lead that focuses on numerical modeling of multiphase flows. I also propose that the cluster, which will be located at ISTO, becomes shared equipment between ISTO (70%) and MAPMO (30%), as to foster further collaborations between applied mathematicians and myself. The 1-μm microtomograph is priority equipment for ISTO in the 2007-2011 period, as it can be applied to other geological materials studied at the Institute. For our young team, acquiring a 1 μm microtomograph means that *routine analysis* of experimental products will be possible. This is necessary each time we seek parameters only accessible by 3D analysis, such as particle spatial distribution, and characterization of porous media. A readily available machine at ISTO is thus essential to systematically study not only bubble coalescence in experimental and natural samples, but also, for instance, the spatial organization of crystals from the deformation experiments.

One cannot study active volcanoes without looking at them. Close collaboration with C. Oppenheimer will ensure that not only our young team does not lose contact with our natural targets, but also that new observations can fertilize our conceptualizations of volcanic phenomena. Thus, both PhD and post-docs will take an active part to the field trips to Montserrat and the subsequent data analysis. Other end-member cases of eruptive regime, such as Vulcanian, can be anticipated to be the focus of our future work at active volcanoes with the new long-term OP-FTIR sensor.

Partie III

Sélection de travaux

Addressing Complexity in Laboratory Experiments: The Scaling of Dilute Multiphase Flows in Magmatic Systems

ALAIN BURGISSER
Institut des Sciences de la Terre d'Orléans, CNRS – Université d'Orléans
GEORGE W. BERGANTZ
Dept. of Earth and Space Sciences, University of Washington, Box 351310
ROBERT E. BREIDENTHAL
Dept. of Aeronautics and Astronautics, University of Washington

Publié dans: Journal of Volcanology and Geothermal Research (2005), v. 141, p. 245-265.

Abstract

The kinematic and dynamic scaling of dilute multiphase mixtures in magmatic systems is the only guarantee for the geological verisimilitude of laboratory experiments. We present scaling relations that can provide a more complete framework to scale dilute magmatic systems because they explicitly take into account the complexity caused by the feedback between particles (crystal, bubble, or pyroclast) and the continuous phase (liquid or gas). We consider three canonical igneous systems: magma chambers, volcanic plumes, and pyroclastic surges, and we provide estimates of the proposed scaling relations for published experiments on those systems. Dilute magmatic mixtures can display a range of distinct dynamical regimes that we characterize with a combination of average (Eulerian) properties and instantaneous (Lagrangian) variables. The Eulerian properties of the mixtures yield the Reynolds number (Re), which indicates the level of unsteadiness in the continuous phase. The Lagrangian acceleration of particles is a function of the viscous drag and gravity forces, and from these two forces are derived the Stokes number (S_T) and the stability number (Σ_T), two dimensionless numbers that describe the dynamic behavior of the particles within the mixture. The compilation of 17 experimental studies relevant for pyroclastic surges and volcanic plumes indicates that there is a need for experiments above the mixing transition ($Re>10^4$), and for scaling S_T and Σ_T. Among the particle dynamic regimes present in surges and plumes, some deserve special attention, such as the role of mesoscale structures on transport and sedimentary processes, or the consequences of the transition to turbulence on particle gathering and dispersal. The compilation of 7 experimental studies relevant to magma bodies indicates that in the laminar regime, crystals mostly follow the motion of the melt, and thus the physical state of the system can be approximated as single phase. In the transition to turbulence, magmas can feature spatially heterogeneous distributions of laminar regions and important velocity gradients. This heterogeneity has a strong potential for crystals sorting. In conclusion, the Re-S_T-Σ_T framework demonstrates that, despite numerous experimental studies on processes relevant to magmatic systems, some and perhaps most, geologically important parameter ranges still need to be addressed at the laboratory scale.

1. Introduction

Mixtures of particles carried by liquids or gases are ubiquitous in magmatic systems. Both magma and ejecta, for example, are mixtures composed of particles (crystals, bubbles, or pyroclasts) carried by a continuous phase (melt or gas). It is axiomatic that the interplay between either silicate melt and crystals, or pyroclasts and entrained gases controls petrologic diversity and eruptive behavior, respectively, but these interactions are extremely difficult to characterize in real-time. Thus, in order to approximate the behavior of the particles entrained by magma or volcanic gases, volcanologists have traditionally simplified the dynamics by using the Eulerian approach. In this framework, one considers mean properties of the field variables (e.g., velocity, steady-state regime) and superimposes the motion that particles would have if the fluid were still. Following the same approach, laboratory experiments designed to illuminate magmatic and eruptive systems commonly considered the scaling of the mean properties of the carrier phase (i.e., Reynolds number), and the scaling between these mean properties and the solid phase properties (i.e., Rouse number). Entrainment rates of ambient air in pyroclastic surges, for example, were proposed from observations of salt-water density currents (e.g., Woods et al., 1998), and convection patterns in magmatic chambers stems from observing heated or cooled tanks of various liquids (e.g., Sparks et al., 1984; Jellinek et al., 1999). The Eulerian framework was also used to experimentally infer the kinematic and dynamic behavior of the particles often suspended in the natural volcanic flows. As a result, it is commonly assumed that the scaling of the continuous phase is sufficient to ensure that a laboratory experiment is a suitable analogue for a given magmatic mixture. Thus, natural volcanic mixtures are experimentally characterized by either particles settling in still fluid or well-mixed suspensions, and only the flow regions that present an end-member behavior are considered, such as the boundary layer of convecting magma bodies (Martin and Nokes, 1988) or the finest fraction of pyroclasts carried in a volcanic plume (Sparks et al., 1991).

Recent advances in the theory of multiphase physics (e.g., Raju and Meiburg, 1995; Crowe et al., 1997; Hogan and Cuzzi, 2001), however, suggest that particles do not simply follow the motions of the continuous phase, whether magmatic liquid or volcanic gas. Particle gathering and dispersal is controlled by the momentum exchange between the continuous phase and the particles. Thus, one can expect complex particle sorting to arise within flowing magmatic mixtures because non-steady processes are likely in magmatic systems. The Eulerian averaging of the flow properties, however, is not able to fully resolve the characteristic scales of particle sorting because it addresses only one aspect of their momentum exchange. This has implications for the geological verisimilitude of laboratory experiments, where kinematic and dynamic scaling are the only guarantee that entire classes of processes are not missed or misinterpreted because the laboratory scale does not adequately represent the natural systems.

Multiphase theories, on the other hand, can provide a more complete framework to scale natural volcanic systems because they explicitly take into account the complexity caused by the feedback between particles and the continuous phase. The scaling of this feedback can be achieved with a Lagrangian approach, where one introduces the unsteadiness of the flow field by using instantaneous parameters such as velocity or forces applied on a particle. Although multiphase physics and its application to laminar and turbulent systems are not new (Crowe et al., 1997), the application of these concepts to volcanic and magmatic systems is novel.

In this study, we present Lagrangian scaling relations that explicitly consider the unsteadiness of the fluid, and we derive the main types of particle behavior as a function of three scaling parameters: the Stokes (S_T), stability (Σ_T), and Reynolds (Re) numbers. In an attempt to present an elementary tutorial in using multiphase scaling, we consider three canonical igneous systems: magma chambers, volcanic plumes, and pyroclastic surges, and we provide estimates of S_T, Σ_T, and Re for published experiments on those systems. We compare the experimental ranges obtained to those of natural volcanic systems, giving an illustration of the capability of these scaling relations to achieve proper scaling of volcanic mixtures. One

important conclusion is that the dynamical domains that are typical of volcanic multiphase systems remain poorly explored by the available body of experimental work.

2. Scaling laws of dilute multiphase mixtures

The variety of the interactions occurring in volcanic mixtures is illustrated in Figure 1. If particles interact with each other, the flowing mixture will be dominated by collisions or near-neighbor interactions, which defines dense and granular systems. Our analysis, however, is restricted to dilute systems, where particle-particle interactions are negligible, which occurs at low particle volume fraction and/or at small relative inter-particle velocity (Crowe et al., 1997). In dilute mixtures, one key control is the relative strength of the forces applied on the particles by the continuous phase versus the forces applied on the continuous phase by the particles. In our analysis, two Lagrangian parameters (S_T and Σ_T) assess whether the continuous phase transfers momentum to particles, which then become coupled to the fluid, or from particles, which then decouple from the fluid. When kinetic energy is continuously exchanged between fluid and particles, feedback mechanisms arise and particles tend to self-organize in complex patterns (e.g., Martin and Meiburg, 1994). The other key control is the amount of unsteadiness of the continuous phase, which we assess by one Eulerian parameter (Re) that characterizes the dynamic state of the continuous phase in the absence of particles, an acceptable assumption for dilute flows. Whether the continuous phase is turbulent or not influences the coupling or decoupling of the particles. Turbulence tends to thoroughly mix particles that are coupled to the continuous phase ('well mixed', Fig. 1), and to segregate decoupled particles dependent on degree of decoupling (incompletely in 'mesoscale structures' or completely in 'independent trajectories'). In the laminar regime, fully-coupled particles are 'passive tracers', partly-decoupled particles drift from the continuous phase streamlines ('drifting'), and fully-decoupled particles or have 'independent trajectories' (Fig. 1).

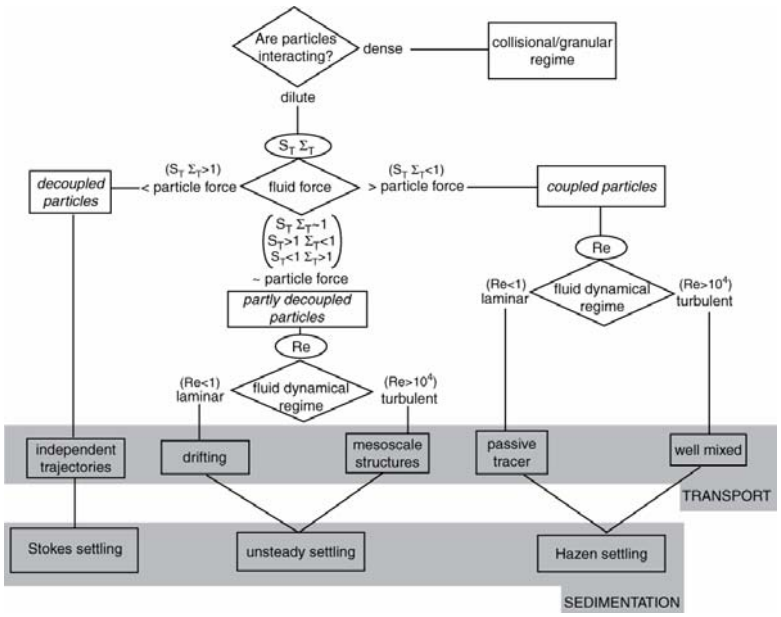

Figure 1. Overview of the interactions occurring in volcanic mixtures of particles and a continuous phase (i.e. liquid or gas). The Stokes number (S_T) and the stability number (Σ_T) are Lagrangian (instantaneous) scalings that assess whether the fluid transfers momentum to particles, and the Reynolds number (Re) is the Eulerian (average) scaling of the fluid dynamical regime. These three scalings characterize the way particles are transported within the mixture. In the turbulent regime, coupled particles are *well mixed*, feedback between fluid and particles segregates partly-decoupled particles in *mesoscale structures*, and fully-decoupled particles have *independent trajectories*. In the laminar regime, coupled particles are *passive tracers*, feedback between fluid and particles causes partly-decoupled particles to *drift* from the fluid streamlines, and fully decoupled particles have *independent trajectories*. Sedimentation processes differ for each multiphase behavior: *Stokes settling* refers to the linear sedimentation law in a still fluid, *Hazen settling* refers to an exponential sedimentation law in a well-mixed fluid, and *unsteady settling* refers to some intermediate case.

Driven by such complex interactions, sedimentation processes vary with the multiphase behavior of the mixture, but establishing these variations is beyond the scope of this paper. In general, particles fully decoupled from the fluid settle at their Stokesian velocity ($d\widetilde{v}/dt = 0$ in Equ. 1, cf. below), whereas particles fully coupled with the flow settle following an exponential decay law (Hazen, 1904; Martin and Nokes, 1989; Bursik and Woods, 1996). In laminar flows, the unsteady settling that results from the feedback between fluid and particles is poorly understood, whereas in turbulent flows, large-scale structures seem to control this regime of settling (Jopling, 1964; Niño et al., 2003; Paiement-Paradis et al., 2003).

To quantify the momentum transfer between the continuous phase and particles, we use the Lagrangian acceleration (i.e. relative to the fluid motion) of a particle in an unsteady flow; a similar approach was employed by Marsh and Maxey (1985). We express this instantaneous acceleration, which depends on the sum of the viscous and buoyancy forces acting on the particle, with a truncation of the Bassinet-Boussinesq-Oseen (BBO) equation valid for most magmatic mixtures (see Appendix A for the details of the simplification). The most convenient form is the dimensionless acceleration:

$$\frac{d\widetilde{v}}{dt} = \frac{\widetilde{u} - \widetilde{v}}{S_T} + \frac{e_g}{F_R^2} \tag{1}$$

where $\widetilde{u}$ is the dimensionless carrier phase velocity, $\widetilde{v}$ the dimensionless particle velocity, and e_g is the unit vector in gravity direction. The Stokes number S_T and the particle Froude number F_R are:

$$S_T = \frac{\tau_v}{f}\frac{\Delta U}{\delta}\left(1 + \frac{\rho_g}{2\rho_p}\right) \tag{2}$$

$$F_R^2 = \frac{\Delta U^2}{g\,\delta}\left(\frac{2\rho_p + \rho_g}{2\rho_p - 2\rho_g}\right) \tag{3}$$

where ΔU is the characteristic speed change of the continuous phase over the characteristic distance δ, g is the acceleration of gravity, ρ_p is the particle density, ρ_g is the continuous phase density, f is a drag factor (Equ. A3), and τ_v is the particle velocity response time:

$$\tau_v = \frac{(\rho_p - \rho_g)d^2}{18\,\mu} \tag{4}$$

where μ is the continuous phase dynamic viscosity.

In the particle acceleration equation (Equ. 1), the Stokes number (S_T) quantifies the effect of the viscous drag by balancing the timescale of the fluid motion with the particle response time τ_v, whereas the Froude number (F_R) quantifies the inertia of the particles. To measure the balance between viscous and inertial forces, we use the stability number (Σ_T), which is a ratio of Stokes and Froude numbers:

$$\Sigma_T = \frac{S_T}{F_R^2} = \frac{\tau_v g}{f\,\Delta U} = \frac{U_T}{\Delta U} \tag{5}$$

Note that Σ_T corresponds to the ratio of the terminal fall velocity U_T of the particle and the carrier-phase characteristic speed-change ΔU.

The unsteadiness of the fluid is linked to the dynamic state of the carrier phase, which is characterized by the bulk Reynolds number (Re):

$$Re = \frac{U\,L}{\upsilon} \tag{6}$$

where U is the characteristic Eulerian speed of the system, L its characteristic length (also called outer-scale), and υ is the kinematic viscosity of the continuous phase. At high Reynolds number, turbulence generates a whole range of eddy sizes, between the outer-scale (L) and the smallest scale of eddies (Kolmogorov length scale λ_0), where the fluid viscosity dissipates the turbulent energy (Figure 2). The condition $Re \geq 10^4$ defines the mixing transition (Konrad, 1976; Breidenthal, 1981; Dimotakis, 2000) that separates the *turbulent* regime, where all length scales (eddy sizes) are present, from the *transitional* regime, where only some scales (eddy sizes) are present. This distinction is important when one considers a fluid loaded with particles, and it will be discussed further in the following sections. The condition Re=1 separates the transitional regime from the *laminar* regime, where the outer-scale is the only length scale present (Dimotakis and Catrakis, 1999).

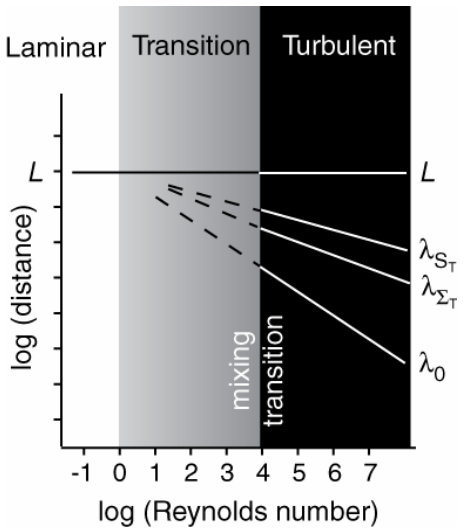

Figure 2. Scales of motion from laminar to turbulent conditions as a function of the Reynolds number (Dimotakis and Catrakis, 1999). L is the outer-scale, λ_{S_T} and λ_{Σ_T} are the particle length scales, and λ_0 is the Kolmogorov scale.

Our scaling analysis shows that Re (Equ. 6), S_T (Equ. 2), and Σ_T (Equ. 5) characterize the dynamics and kinematics of dilute multiphase mixtures. Yet, choosing appropriate scales for the fluid motions (U, L, ΔU, and δ) to evaluate these dimensionless numbers is not obvious. U and L are the outer Eulerian scales for Re, which can be estimated from the average properties of the natural volcanic system (e.g., the mean current speed and thickness in post-conduit flows or the mean convection speed and size in magmas, Fig. 3). ΔU and δ are the Lagrangian instantaneous scales, which vary with the dynamic object considered (e.g., eddies of various speed and size in post-conduit flows or viscous plumes of varying shape in magmas, Fig. 3). Although knowing the cause of motion (e.g., convection, buoyancy, or decompression) is essential to estimate correctly the scaling parameters, it does not affect the dynamic behavior of the mixture by itself; at equal Re, S_T, and Σ_T, a given mixture has a similar kinematic behavior regardless of the source of motion. In the following sections, we will consider different forms of Re, S_T, and Σ_T for two magmatic mixtures: crystals/magma and pyroclasts/gas.

Table 1. Summary of parameters used to scale experimental works in Figs. 6-8.

Ref.[a]	d μm	μ Pa s	ρ_f kg/m^3	ρ_p kg/m^3	U m/s	ΔU min. m/s	L m	δ min. m	Apparatus
Volcanic plumes									
1.	38-60	10^{-3}	1000	2470	0.05-0.1	0.0125	0.007-0.25	$7\ 10^{-4}$	Water tank
2.	28-131	10^{-3}	1000-1021	3210	0.07-0.018	0.007	0.09-0.15	0.09	Water tank
3.	135-328	10^{-3}	1000	3210	0.016-0.053	0.0133	0.006-1.3	0.006	Water tank
4.	23-53	10^{-3}	1000	3217	0.018-0.029	0.018	0.05-0.2	0.05	Water tank
5.	4.5-36.5	10^{-3}	1000-1037	3217	$1.35\ 10^{-3}$ – $2.9\ 10^{-3}$	$1.35\ 10^{-3}$	0.01-0.035	0.01	Water tank
6.	9-25	10^{-3}	1000-1030	3218	0.12-2.4	0.03	0.03	0.005	Water tank
7.	28-131	10^{-3}	1000-1021	3210	0.007-0.018	0.007	0.052-0.08	0.08	Water tank
Pyroclastic surges									
8.	23-37	10^{-3}	1000	3217	0.0036-0.0996	0.0249	0.01-0.14	0.014	Water tank
9.	31-$4\ 10^3$	10^{-3}	1000	1440-3200	0.09-0.61	0.0225	0.01-0.08	0.001	Water tank
10.	44-707	10^{-3}	1000	2200	0.192-1.12	0.048	0.15-0.3	0.015	Water tank
11.	123-390	10^{-3}	1000	2420-2650	0.06	0.015	0.4	0.04	Water tank
12.	210-297	$9.2\ 10^{-4}$-$7.4\ 10^{-4}$	1014-1142	1143-1196	0.01-0.4	0.1	0.06-0.12	0.012	Water tank
13.	100	10^{-3}	1030	2400-2600	0.01-0.1	0.01	0.05-0.1	0.01	Water tank
Powder snow avalanches									
14.	10-100	10^{-5}	1	4000-5000	0.08-0.3	0.02	0.1-0.2	0.01	Chute flow
14.	10^4 – $2\ 10^5$	10^{-5}	1	100	6	1.5	150-300	20	Provoked snow avalanche
Volcanic plumes and pyroclastic surges									
15.	90-500	10^{-5}	1	2000	10-100	2.5	0.1	0.01	Vertical shock tube
Magmas									
16.	$3\ 10^3$-$1.1\ 10^4$	$6.3\ 10^{-4}$-2.06	1260-1287	2109	$3.75\ 10^{-6}$-$1.25\ 10^{-4}$	$3.75\ 10^{-6}$	0.23	0.001	KNO_3 tank
17.	16	10^{-3}	1000	3217	10^{-4}-10^{-3}	10^{-4}	0.2	0.02	Water tank
18.	$5\ 10^3$-$2\ 10^4$	$1.26\ 10^{-3}$-0.129	1260-1287	2109	0.05-0.1	10^{-3}	0.2	0.01	KNO_3 tank
19.	210-500	10^{-3}	1000	1033	$8.13\ 10^{-3}$-Re[b]	$8\ 10^{-5}$	0.1-0.2	0.05	Water tank
20.	10^3-$5\ 10^3$	$6.3\ 10^{-4}$ - 0.001	1160-1358	1140-2284	10^{-7} -10^{-4}	10^{-7}	0.15	0.001	$NaCO_3$ tank
21.	10^3	160	1477	2600	$2.78\ 10^{-6}$	$2.78\ 10^{-6}$	0.2	0.1	Sucrose tank
Magmas and pyroclastic surges									
22.	1320	10^{-3}	1000	1000	0.162-5.576	0.162	0.0108	$1.08\ 10^{-3}$	Couette flow
22.	35	10^{-5}	1	2200	1.72-3.9	0.975	0.09	0.009	Chute flow

[a]References are: 1. Cardoso and Zarrebini (2000); 2. Carey et al. (1988); 3. Ernst et al. (1996); 4. Hogg and Huppert (2001); 5. Hoyal et al. (1999); 6. Huppert et al. (1991); 7. Sparks et al. (1991); 8. Bonnecaze et al. (1995); 9. Choux and Druitt (2002); 10. Ghosh et al. (1986); 11. Jobson and Sayre (1970); 12. Stix (2001); 13. Woods et al. (1998); 14. Bozhinskiy and Sukhanov (1998); 15. Anilkumar et al. (1993); 16. Huppert et al. (1983); 17. Koyaguchi et al. (1990); 18. Martin (1990); 19. Martin and Nokes (1989); 20. Turner and Gustafson (1981); 21. Weinstein et al. (1988); 22. Bagnold (1954).

[b]The upper bound of Reynolds number was calculated from Rayleigh and Prantl numbers.

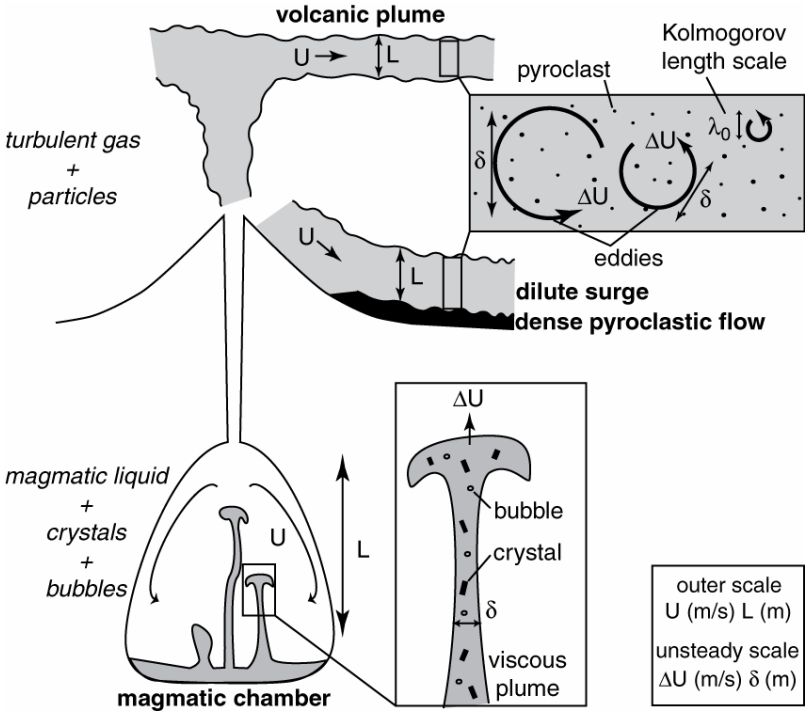

Figure 3. Possible scales of the continuous phase motions: U, L, ΔU, and δ, encountered in magmatic mixtures, the evaluation of which is necessary to calculate S_T, Σ_T, and Re. Outer-scales (U and L) are tied to macroscopic characteristics of the system, whether volcanic plume, pyroclastic surge, or magmatic chamber. In turbulent, post-conduit volcanic systems, unsteady scales (ΔU and δ) range from the outer-scale down to the Kolmorogov scale. In mostly laminar systems such as convecting magmas, ΔU and δ are constrained by viscous plumes. Note that dense systems such as pyroclastic flows cannot be scaled with the framework presented herein.

3. Methods used to evaluate the scaling of experimental studies

There is a substantial number of laboratory experiments designed to illustrate the dynamics of multiphase magmatic systems. Below, we summarize the parameter ranges of these experiments to assess their geological verisimilitude. To that end we have selected experiments (Table 1) meeting two criteria. First, the experiment has been published with, or was quoted by, work on one of the two magmatic mixtures discussed here (crystals/magma or pyroclasts/gas). Second, the experiment must explicitly address the dynamics of a multiphase system. For example, we have not included experiments attempting to address the dynamics of magma chambers from one or two-liquid systems because there are no particles in such experiments.

For each experiment, we calculated the three dynamic scaling parameters relevant to the Lagrangian-Eulerian framework of multiphase flows: Re, S_T, and Σ_T. Whereas estimates of Re are often provided, none of the studies report the Lagrangian scaling S_T or Σ_T. Thus, we estimated the Lagrangian scaling by using the characteristics of the particles (density and diameter) and the fluid (density and viscosity, Table 1). The characteristic length scale δ and speed ΔU are constrained by the outer-scales L and U (the same values as used in the bulk Re, Equ. 6) and the smallest unsteadiness within the flow. Because the values of the two dynamic parameters δ and ΔU considerably vary in time and space, we selected the values that maximize the range covered by the dimensionless numbers S_T and Σ_T. In general, the minimum size of unsteadiness δ is the lower bound of L if $Re<10^4$ and a tenth of that value if $Re>10^4$. The minimum speed of unsteadiness ΔU is the lower bound of U if $Re<10^4$ and the quarter of that value if $Re>10^4$ (see section 4 below). Each experiment is thus represented by a box in the Re-S_T-Σ_T space defined by the maximum and minimum values of the three dimensionless numbers. Even moderate changes (say less than an order of magnitude) on L and U do not affect significantly the box size at the scale we are considering: the three scalings span more than 10 orders of magnitude in all volcanic systems. It should also be

appreciated that the data points collected from an experiment form either a cloud of discreet points (unique scale L in laminar regime) or a volume (continuum of scales in the transitional and turbulent regimes) that does not necessarily fill the entire box. Furthermore, if some experiments systematically explore a range of Re, it is never the case for S_T or Σ_T. Any given data set is thus likely to consist of an apparently random selection of S_T and Σ_T values, and we will discuss the implications of this lack of regularity for the geological verisimilitude of the laboratory experiments.

4. Multiphase scaling of mixtures of pyroclasts and gas

Post-conduit transport of pyroclasts occurs either by volcanic plumes or by pyroclastic density currents. The carrier phase is gaseous with a Reynolds number above the mixing transition ($Re \geq 10^4$) and is therefore turbulent. Equation 1 is valid because the density ratio between particle and gas exceeds 10^3 (see Appendix A). In our Lagrangian description of turbulence, we choose ΔU to be the eddy rotation speed and δ the eddy diameter to focus on the unsteadiness of the gas (Fig. 3). Therefore, S_T is the ratio of the response time of particles τ_v (particle reaction to unsteady forcing by gas turbulence) to the eddy rotation time and measures the coupling between gas and particles. The term in parenthesis in Equ. 2 is equal to unity and the Stokes number becomes:

$$S_T = \frac{\tau_v}{f}\frac{\Delta U}{\delta} \tag{7}$$

Particles with $S_T > 1$ decouple from the gas and increase the turbulence intensity of the mixture, whereas particles with $S_T < 1$ are dynamically attached to the gas and reduce turbulence intensity. If $S_T \sim 1$, particles tend to gather at the eddy periphery, possibly escaping from its gyratory motion (Hogan and Cuzzi, 2001). The Stokes number controls a self-organization of the particles within an eddy, concentrating or dispersing particles as a function of their density and/or size.

The stability number is a measure of the particle residence time within an eddy and assesses the steady gravitational forcing on particles versus the viscous drag of the gas. Equation 5 reduces to:

$$\Sigma_T = \frac{\tau_v g}{f \Delta U} \tag{8}$$

Particles with $\Sigma_T > 1$ are dominated by the steady acceleration of gravity and have a trajectory along the lines of this force, whereas gravity forces can be neglected for particles with $\Sigma_T < 1$.

Because the combination of S_T and Σ_T quantifies the effect of the fluid forces on the particles (Fig. 1), these parameters reveal whether *1)* particles are decoupled from the gas and settle ($S_T > 1$ and $\Sigma_T > 1$), or *2)* particles are coupled with the gas and well mixed within the flow ($S_T < 1$ and $\Sigma_T < 1$), or *3)* a strong feedback exists between fluid and particle, creating transient particle-gathering and dispersal ($S_T \sim 1$ and $\Sigma_T \sim 1$; $S_T > 1$ and $\Sigma_T < 1$; $S_T < 1$ and $\Sigma_T > 1$). The two first regimes of particles behavior are similar to the ones predicted by the classical Eulerian approach. The last regime, however, leads to transient segregations of particles, which will tend to gather in zones of least velocity gradient. Resultant particle gathering causes higher particle concentrations that organize in dendritic-like patterns within the flowing mixture (Fig. 4). These ephemeral patterns are *mesoscale structures*, which cannot be resolved by averaging techniques (Agrawal et al., 2001; Zhang and VanderHeyden, 2002).

It is difficult to determine which unsteady scales ΔU and δ control mesoscale structures because turbulence generates a whole range of eddy sizes between L and λ_0 (Fig. 2), and thus a wide range of S_T and Σ_T for a given particle size. Among all scales present in turbulent systems, however, there may be two length scales λ_{S_T} and λ_{Σ_T} that correspond to eddies whose $S_T = 1$ and $\Sigma_T = 1$, respectively. These particular eddy sizes control particle gathering

and dispersal leading to the formation of mesoscale structures (Fig. 4). If the relationship between ΔU and δ is known, one can determine λ_{S_T} and λ_{Σ_T} for a given particle size. An estimate of this relationship can be done using the spectrum of turbulent kinetic energy, which describes the transfer of kinetic energy from large eddies to smaller eddy. Figure 5, for example, shows values of λ_{S_T} and λ_{Σ_T} for various particle size given by a spectrum of the form $\delta^{-8} \cdot exp(\delta^{2})$ (Burgisser and Bergantz, 2002). The possible emergence of mesoscale structures can thus be assessed as a function of particle size if the spectrum of kinetic energy is known.

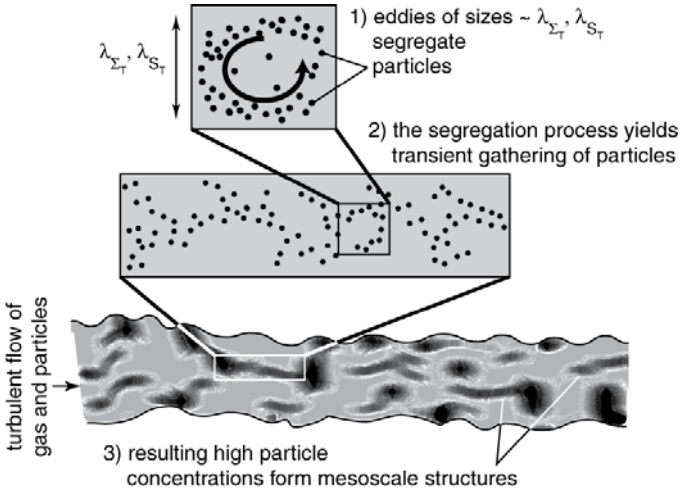

Figure 4. Schematic view of the emergence of mesoscale structures in turbulent dilute mixtures. Eddies whose forces balance particle drag and inertia are of characteristic sizes λ_{S_T} and λ_{Σ_T}. The strong feedback between fluid and particles leads to transient segregations of particles, which tend to gather in zones of least velocity gradient. Particle gathering causes higher particle concentrations that organize in patterns of sizes between particle size and the outer-scale called mesoscale structures. Note these structures may affect flow dynamics and thus have a major effect on processes like particle aggregation and coalescence.

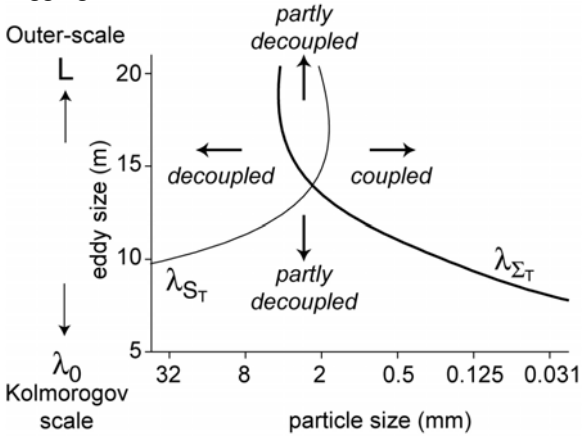

Figure 5. Example of the variations of length scales λ_{S_T} and λ_{Σ_T} with particle size one may expect in a pyroclastic surge. Horizontal turbulent air stream 20-m thick at 15 m s^{-1} loaded with 1000 kg m^{-3} particles. Regimes of multiphase particle transport refer to Fig. 1.

It is possible, however, to narrow the range of length scales at which mesoscale structures are likely to develop in turbulent flows without knowing the specific shape of the spectrum by assuming that only the most energetic eddies control particle sorting. This assumption is less restrictive than using a particular spectrum of kinetic energy because the shape of the energetic end of the spectrum is controlled by the boundary conditions and is thus case-specific. The energy-containing range consists of the largest eddies, say from the size of the current L down to an order of magnitude smaller, which corresponds to 80-90% of the total

kinetic energy (Pope, 2000). Parameters λ_{S_T} and λ_{Σ_T} can be calculated by assuming that the rotation speed of these eddies (ΔU) is on the order of the root-mean-square velocity of the current, which is about 25% of its mean speed U. Therefore, mesoscale effects are likely to be present in a given experiment or natural case if $L<(\lambda_{S_T}, \lambda_{\Sigma_T})<L/10$ when $\Delta U=U/4$.

We stress that when the flow regime is *transitional*, the turbulent spectrum is incomplete. In other words, λ_{S_T} and λ_{Σ_T} are *not* present in any given volume of the flow. Thus, S_T and Σ_T are likely to erratically jump from one value to another, thus leading to an erratic particle sorting. Note that the spatial distribution of vortices below the mixing transition is poorly understood, and thus that particle sorting cannot yet be predicted when $1 < Re < 10^4$.

It has been long known that electrostatic forces can affect up to 50 wt.% of particles expelled by volcanic explosions, causing them to aggregate (e.g., Sparks et al., 1997). Unfortunately, the BBO equation (Equ. 1) only describes the interactions between fluid and particles, whereas electrostatic forces apply between particles. We can predict, however, that mesoscale structures are likely to favor particle aggregation because they tend to rapidly transport concentrations of particles across the plume/current, thereby creating favorable conditions for electrostatic interactions to occur.

4.1. Revisiting experimental work on post-conduit pyroclastic transport

Post-conduit pyroclastic material can be transported by either volcanic plumes or pyroclastic density currents (Fig. 3). For each of these volcanic flows, we estimated the ranges of the multiphase scaling parameters (Re-S_T-Σ_T) for the natural volcanic system and the ranges of the laboratory experiments that address the dynamics of these flows. The comparison of natural ranges and laboratory ranges of Re-S_T-Σ_T help us to address important aspects of the inherent complexity of scaling multiphase mixtures.

Table 2: Common ranges of the dynamic variables of three magmatic systems.

variable	unit	range	volcanic plumes	pyroclastic surges	magmatic liquids
δ	mm	min	0.015	0.015	0.015
		max	32	1024	1
μ	Pa s	min	$3\ 10^{-5}$	$3\ 10^{-5}$	10^3
		max	$3\ 10^{-5}$	$3\ 10^{-5}$	10^8
ρ_f	kg m^{-3}	min	0.1	1	2200
		max	1	1	2800
ρ_s	kg m^{-3}	min	1000	1000	2200
		max	2500	2500	2400
ρ_s/ρ_f		min	25000	2500	1.09
		max	1000	1000	0.79
U	m s^{-1}	min	10	10	0
		max	50	200	1
ΔU [a]	m s^{-1}	min	2.5	2.5	0
L	m	min	1200	10	10
		max	3900	1000	1000
δ [b]	m	min	120	1	10
Re		min	$4.0\ 10^7$	$3.3\ 10^6$	0
		max	$6.5\ 10^9$	$6.7\ 10^9$	$2.8\ 10^3$
S_T		min	$9.4\ 10^{-6}$	$1.1\ 10^{-3}$	0
		max	$2.0\ 10^2$	$9.7\ 10^7$	$1.1\ 10^{-9}$
Σ_T		min	$4.5\ 10^{-5}$	$2.8\ 10^{-6}$	0
		max	$7.7\ 10^4$	$9.7\ 10^9$	$1.1\ 10^5$

[a]Minimum speed of unsteadiness ΔU equals U_{min} if $Re<10^4$ and $U_{min}/4$ if $Re>10^4$.

[b]Minimum size of unsteadiness δ equals L_{min} if $Re<10^4$ and $L_{min}/10$ if $Re>10^4$.

We estimated the natural range of the scaling parameters for volcanic plumes from representative parameters given by 1200 simulated plumes generated for 22 volcanoes in the North Pacific using the 52-years average wind speeds (Table 2; Papp, 2002). The simulations were carried out with a numerical model (PUFF; Searcy et al., 1998) that calculates the dispersion by wind of particles released at various heights above a given vent. Known eruptions were used as a reference for the simulations, from which we derived parameters of Table 2. The laboratory ranges of scaling parameters were taken from 8 experimental studies (Table 1).

We found that most experimental ranges are in the transitional regime, whereas the natural volcanic range of *Re* lies above the mixing transition (Fig. 6A). The experiment that lies in the turbulent regime demonstrates that turbulent conditions are achievable in laboratory. The S_T-Σ_T plot shows that the experimental values fall within the range covered by the natural systems (Fig. 6B). In general, experiments overlap more than one transport regime, and were conducted at low S_T (Fig. 6C).

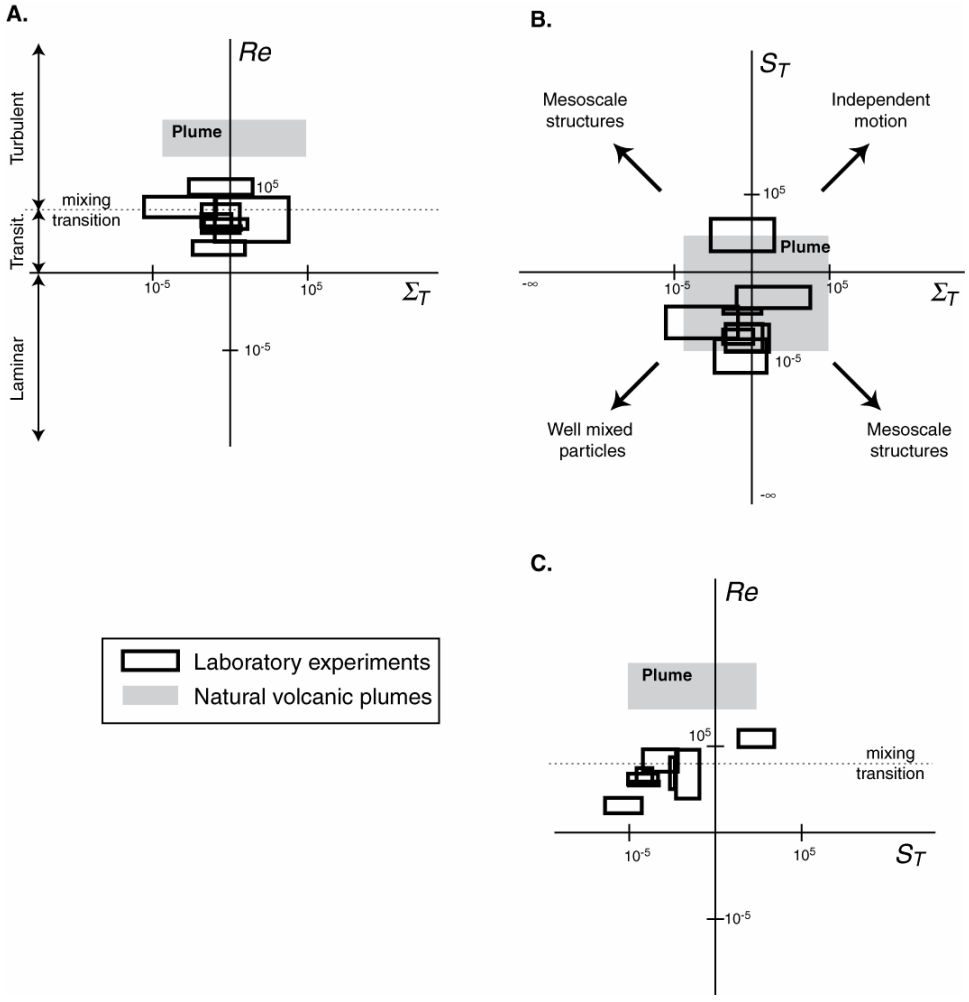

Figure 6. Estimates of *Re,* S_T, and Σ_T for experimental work published in relation with volcanic plumes. Fields of multiphase behavior are indicated (see also Fig. 1). Particles in mesoscale structures are subjected to transient transport and sedimentation. Particles with motions independent from the fluid settle out of the flow. Mixture theory applies to well-mixed particles, the behavior of which can be described with the Rouse number. Note that since axes are in logarithmic units, minus infinity represents a zero-value. Parameters and references of experimental studies are in Table 1.

Pyroclastic density currents are composed of two end-members, dilute surges and dense pyroclastic flows, that are likely to coexist within the same density current (Fig. 3; Fisher, 1983; Valentine, 1987; Burgisser and Bergantz, 2002). We restricted the scaling of the natural volcanic systems to the surge end-member (Table 2), because the analysis proposed herein focuses on dilute systems (i.e. non-colliding particles, Fig. 1). We included the scaling

parameters of a surge that occurred in 1997 at Soufriere Hills, Montserrat (Sparks et al., 2002) and the parameters of a powder-snow avalanche from observations by Bozhinskiy and Sukhanov (1998). The laboratory ranges of scaling parameters were calculated from 10 experiments related to surges and powder-snow avalanches (Table 1).

We note that several experimental studies on surges lie above the mixing transition (Fig. 7A) and thus ensure the adequate scaling of the dynamical state of the carrier phase. The S_T-Σ_T plot shows a nearly complete coverage of the natural range by the experiments, although we note that only two studies focus on a specific transport regime (Fig. 7B). Interestingly, the scaling parameters of a natural snow avalanche overlap with the natural field of surges.

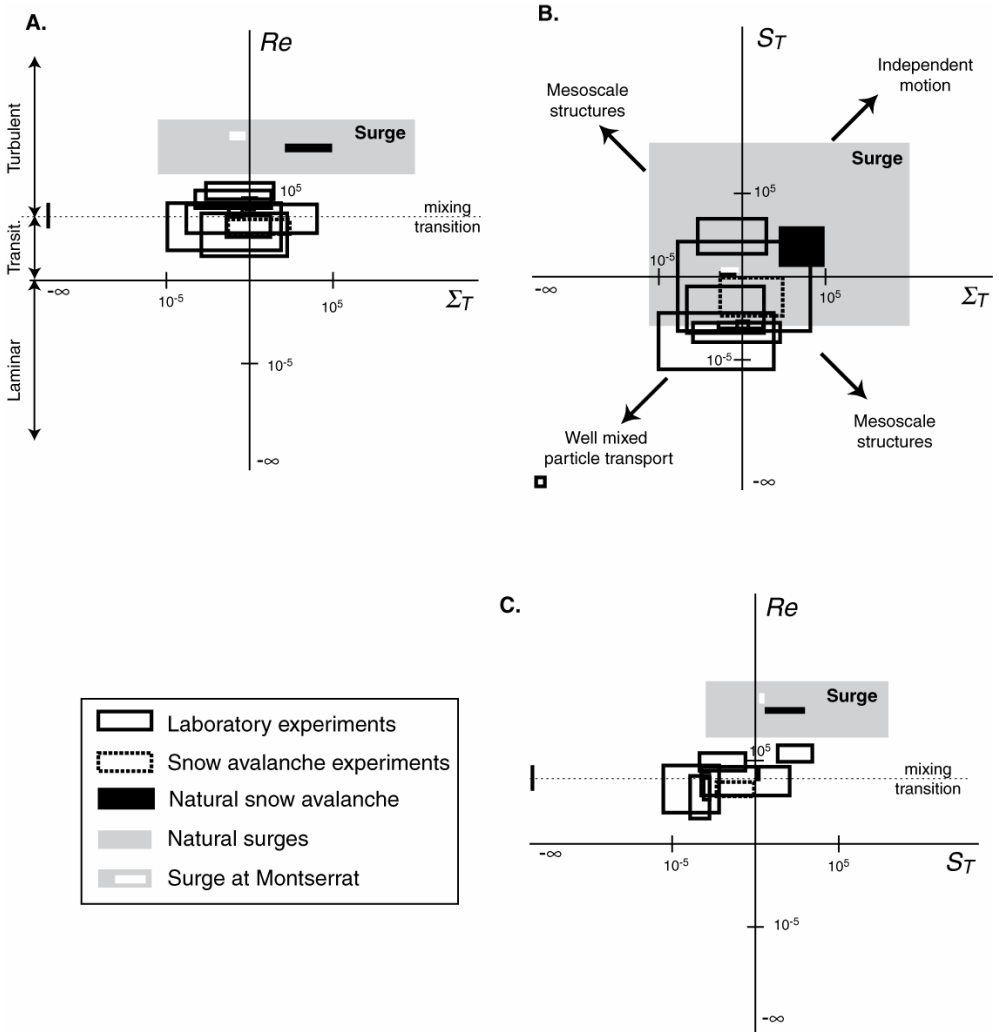

Figure 7. Estimates of *Re*, S_T, and Σ_T for experimental work published in relation with pyroclastic surges. Fields of multiphase behavior are indicated (see also Fig. 1). Particles in mesoscale structures are subjected to transient transport and sedimentation. Particles with motions independent from the fluid settle out of the flow. Mixture theory applies to well-mixed particles, the behavior of which can be described with the Rouse number. Note that since axes are in logarithmic units, minus infinity represents a zero-value. Scaling ranges of the December 26, 1997 Montserrat surge (Sparks et al., 2002) and a powder-snow avalanche (Bozhinskiy and Sukhanov, 1998) are also shown within the natural surge field. Parameters and references of experimental studies are in Table 1.

4.2. Implications for volcanic plumes and pyroclastic surges

Estimates of S_T and Σ_T in volcanic plumes and pyroclastic surges show that a systematic exploration of the mesoscale domain would doubtlessly help to clarify the relation between transport and sedimentation in these systems (Figs. 6B and 7B). Despite the known importance of the Stokes number in volcanic plumes (Kaminski and Jaupart, 1997), none of

the experimental works addressing plume sedimentation report estimates of S_T and Σ_T. This suggests that the role of mesoscale structures has been overlooked despite their likely occurrence in both natural systems (Figs. 6 and 7). Furthermore, when the experimental ranges we report in Figs. 6A and 7A lie below the mixing transition, the observed particle behaviors are, most likely, not representative of the turbulent natural systems. We expect such a discrepancy to occur because the existence of λ_{S_T} and λ_{Σ_T} are only guaranteed above the mixing transition (Fig. 2). Natural powder-snow avalanches seem to have similar kinematics as pyroclastic surges (Fig. 7), and thus experiments related to avalanches are relevant to the study of surges.

Obtaining the natural range of scales in experiments is challenging, due to the large range of S_T and Σ_T present in the natural volcanic systems and the requirement of fully-developed turbulence at the laboratory scale. Our results show that the choice of the continuous phase is crucial, and that some analogue media are more suitable than others for achieving experimental similitude. For example, water is commonly used for experimental studies of surges. Two issues, however, have to be addressed to ensure proper dynamic scaling of such experiments. First, the density contrast between particles and water has to be on the same order as the natural one (10^3), otherwise buoyancy and virtual mass effects will significantly affect particle dynamics (cf. Appendix A). In the experiments using water as carrier liquid (Table 1), the density ratio of particle to water is systematically below 10, two orders of magnitude lower than in the natural volcanic systems. The effect of gravity on transport of the particles is thus underestimated in those experiments. Second, all water-tank studies reported herein are in the transitional regime, suggesting that the velocities required to ensure turbulent conditions are difficult to attain in laboratory-scale water tank. Work conducted on powder snow avalanches, however, uses gas as the continuous phase, and nearly achieves fully turbulent conditions (Fig. 7). These experiments compensated the downscale in size and speed of the gaseous carrier phase by using high-density particles. Thus, the use of gas as the carrier phase eases the scaling of S_T and Σ_T, but is likely to increase the working speeds up to tens of m s^{-1}.

The Rouse number, which is the ratio of the particle terminal velocity over the Eulerian flow speed, has been extensively applied in volcanic systems (e.g., Carey, 1991). The Rouse number arises from a particular case from the diffusion equation known as the Rouse equation (Hunt, 1954; Hunt 1969; Ghosh et al., 1981) and the mixture theory used to derive the Rouse equation applies to scalar quantities advected in turbulent flows. The Rouse number has successfully been applied to tank flume experiments and correctly predicted the sediment concentration at any depth of the turbulent current (Ghosh et al., 1986). Those experiments, which had S_T on order of 10^{-3}, illustrate that low S_T particles can be considered as statistically attached to the fluid. The mixture theory, however, fails to adequately represent the behavior of particles with a large S_T, typical of many natural volcanic systems. Hence, the use of the Rouse number, which derives from this theory, should be restricted to low S_T and Σ_T particles transported by flows at Reynolds number above the mixing transition.

5. Multiphase scaling of mixtures of crystals, bubbles, and magmatic liquid

The dynamics of magma bodies can be complex, with transient open-system processes and a variety of density changes contributing to dynamic behavior. Our intent is not to comprehensively address this complexity, but rather to consider some applications of our scaling approach to simplified magmatic applications. In magmatic mixtures, the density ratio between crystal and liquid approaches unity and the particle Reynolds number is low (i.e., $f \sim 1$). The truncated BBO (Equ. 1) is thus valid if either the magma flows in the laminar regime ($Re < 1$), or if crystals are much smaller than the unsteady structure (e.g., viscous plume). Under these circumstances, S_T and Σ_T can be reduced to:

$$S_T = \frac{3}{2}\tau_v \frac{\Delta U}{\delta} \tag{9}$$

$$\Sigma_T = \frac{g\,\tau_v}{\Delta U}\left(\frac{\rho_p - \rho_g}{\rho_p}\right) \tag{10}$$

Particles with $S_T > 1$ are decoupled from the liquid motions. Buoyancy forces are likely to dominate their behavior, and particle motion can be described by settling in a still fluid (Stokes settling, Fig. 1). Σ_T indicates whether particles settle ($\Sigma_T > 0$), rise ($\Sigma_T < 0$), or are neutrally buoyant ($\Sigma_T = 0$). At vanishing S_T and Σ_T, particles can be considered as passive tracers, and the Reynolds number of the liquid dictates the kinematic behavior of the system. Crystal gathering and dispersal can thus be described as a chaotic advective system, which reduces the problem to a single virtual phase (Aref, 1990; Flinders and Clemens, 1996; Bergantz, 2000; Perugini and Giampiero, 2000; Perugini et al., 2002; Perugini et al., 2003). In other words, the dynamics of a slowly (laminar) convecting system is such that passive tracers drift apart (advect), and that two initially distinct populations of these tracers mix chaotically with time. Such a process is suggested by the simulations of Rudman (1992) and Simakin et al. (1997).

In magmas, the 'background' buoyancy flux is rate-limited by conductive heat loss (Smith, 1988; Marsh, 1989), with transient excursions associated with reintrusion and/or vesiculation (Bergantz and Breidenthal, 2001). Hence the continuous phase is significantly below the mixing transition, leading to two possible dynamic regimes: laminar and transitional. Motion occurs through unsteady structures such as viscous plumes, either positively buoyant (e.g., Jellinek and Kerr, 1999; Snyder, 2000; Couch et al., 2001) or negatively buoyant (e.g., Brandeis and Jaupart, 1986; Marsh, 1988; Simakin et al., 1994; Bergantz and Ni, 1999; Jellinek and Kerr, 2001). Plumes can originate from a boundary layer becoming unstable because of density changes, or because of the injection of new liquid (Fig. 3). In both cases, it is possible to define *Re* as a function of the buoyancy flux:

$$\mathrm{Re} = \frac{B^{1/2} L^2}{\upsilon^{3/2}} \tag{11}$$

where the outer-scale L is the height of the system (magmatic chamber, Fig. 3), υ is the kinematic viscosity of the magmatic liquid, and B is the buoyancy flux, upon which the velocity scale is based (see Appendix B, Equs B2 and B3).

5.1. Revisiting experimental work on multiphase flow in magmas

The estimation of the range of Reynolds numbers that characterizes magmatic systems is not trivial. *Re* is sensitive to the scale studied, whether large-scale chamber dynamics, or small-scale boundary layer problems (e.g., Jaupart and Tait, 1995). Thus, the range of *Re* varies considerably according to the magmatic process of interest. The parameter range we propose (Table 2) is representative of chamber-wide dynamics, neglecting transient local processes that may have higher *Re*, such as sidewall density current caused by crystal landslide or rapid vesiculation (Bergantz and Breidenthal, 2001). We considered that the lower bound of *Re* is zero, as liquid velocity vanishes at the chamber wall. We used Equ. 11 to set the upper bound of *Re*, and we selected viscosities to cover a wide spectrum of magmatic compositions. We used data from Couch et al. (2001) to determine the scaling of the magmatic reservoir feeding the current eruption at Soufriere Hills, Montserrat. We calculated the scaling parameters from 7 published experiments (Table 1).

Scaling parameters of the experiments show a complete coverage of the transitional regime in the *Re*-Σ_T plot, which overlap well with the natural range we defined (Fig. 8A). The majority of the natural field of magmatic chambers is in the chaotic advective regime, in which particles are passive tracers of the flow patterns, whereas most experiments do not overlap this transport regime (Fig. 8B). Along these lines, most experiments have much larger S_T than natural systems (Fig. 8C).

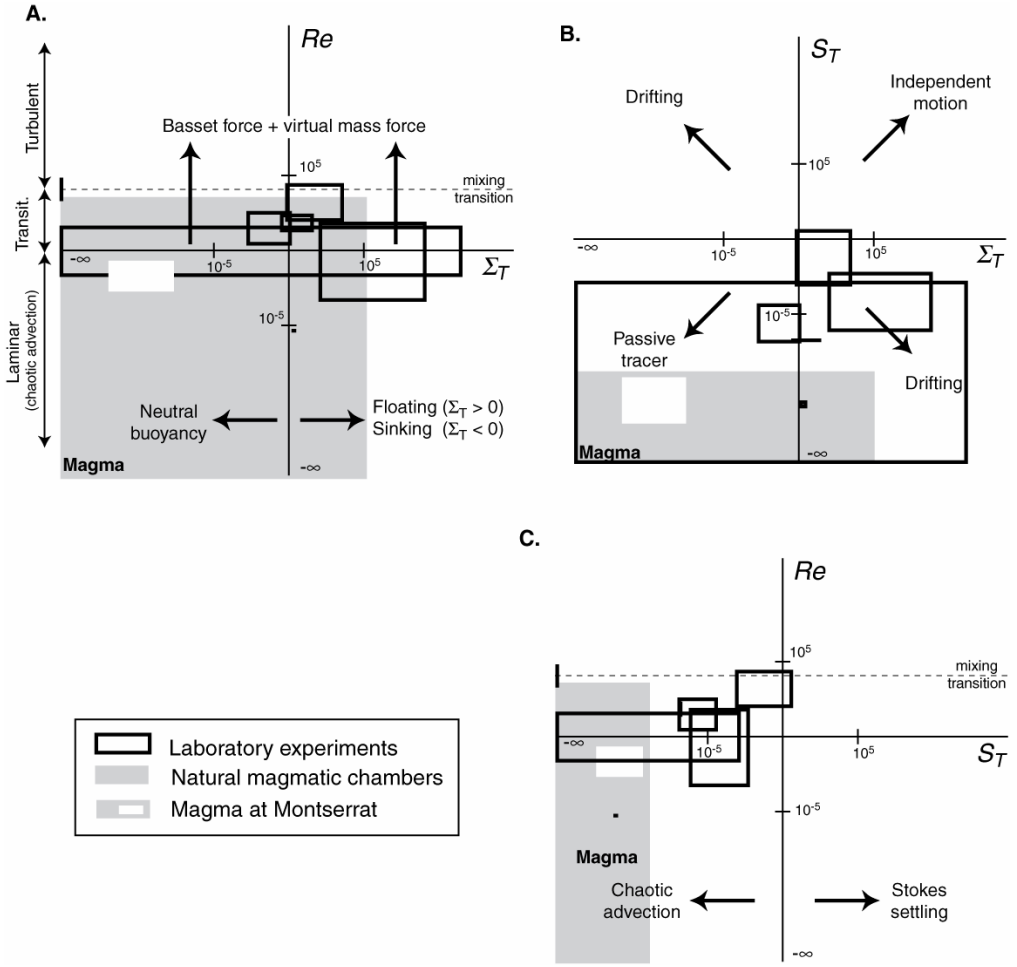

Figure 8. Estimates of *Re*, S_T, and Σ_T for experimental work published in relation with magmatic systems. Fields of multiphase behavior are indicated (see also Fig. 1). Particles with motions independent from the fluid settle out of the flow as if it were still. In laminar regime, particles acting as passive tracer follow the chaotic advection of the fluid. Basset and virtual mass forces may be important when *Re* is transitional, and Σ_T indicates how buoyant particles are. Note that since axes are in logarithmic units, minus infinity represents a zero-value. Scaling ranges of the Montserrat magmatic system (Couch et al., 2001) are also shown within the natural magmatic field. Parameters and references of experimental studies are in Table 1.

5.2. Implications for magmatic systems

Crystal transport in magma chambers has previously been described by using a ratio (S) based on the BBO equation (Marsh and Maxey, 1985; Weinstein et al. 1988; Rudman, 1992). Because S is the ratio of the particle settling velocity to the convective velocity, it corresponds to a stability number Σ_T with the characteristic velocity ΔU based on a Eulerian velocity. In other words, in the viscous regime, $S = \Sigma_T$ because the velocity scale is unique in viscous flows. To characterize the multiple scales of motions present in the inertial regime, however, a range of values of ΔU (velocity of the instabilities driving the flow) needs to be considered. This slightly more general definition gives the proper range of values at any Reynolds number. In any case, care should be taken in working with S_T and Σ_T in the inertial regime, because the simplification of the BBO equation (from Equ. A1 to Equ. 1) is not valid (see Equs. A5-A6). A comprehensive study of crystal behavior when $Re > 1$ thus needs proper scaling of the Basset and virtual mass forces, which is beyond the scope of this paper.

Although we consider that particles with $S_T < 1$ are dynamically attached to the liquid, they will nevertheless have a small 'drift velocity' compared to the carrier phase, unless $S_T = 0$. Marsh and Maxey (1985) concluded that this drift velocity becomes important for the long-term behavior of particles trapped in a periodic flow, because it significantly affects their residence time. An even more general perspective might be that all natural flows are

aperiodic, which often generate better mixing than periodic flows by greatly reducing the size of non-chaotic regions ('regular islands' in 2D laminar periodic flow, Liu et al., 1995; Solomon and Mezic, 2003). As unsteady structures are created, morph, and vanish, the drift velocities of the particles that are associated with each structure are unlikely to cumulate, but rather tend to cancel out. We thus suggest that drift velocities are negligible in the laminar case on the premise that magmatic systems are aperiodic. Note that this aperiodicity does not allow the practice, common in chaotic advection studies, of reducing the degrees of freedom by eliminating time using, for example, Poincaré maps (Ottino, 1990).

With these caveats, the overlap of the advective regime with the field of natural magmatic systems (Fig. 8) suggests that single-phase flows of miscible liquids approximate crystal-liquid mixtures. In other words, understanding the flow field of the liquid also means understanding the motions of the crystals (Perugini and Giampiero, 2000; Perugini et al., 2003). We note, however, the paucity of magma-scaled, unseeded experiments in the laminar regime to understand crystal gathering and dispersal (e.g., Jellinek et al., 1999). On the other hand, the gap of several orders of magnitude of S_T separating the natural field from the Stokes regime confirms the inapplicability of a simple settling law to understand crystal transport in convecting magmas, as discussed by Martin and Nokes (1988). Thus, magmatic liquids cannot be considered as motionless, which forces us to look at magmatic chambers as fundamentally dynamic systems. Hence, experiments underestimate the control of viscous drag because they have S_T larger than the typical range of natural systems (Fig. 8B,C). As a result, the importance of small-scale unsteadiness (or accelerations) that drives crystal gathering and dispersal in magmatic chambers has been underestimated.

5.3. Using the Lagrangian framework in magmas

The Stokes and the stability numbers provide a means for assessing the relative motion between phases and thus whether particles present in a convective melt can separate from the surrounding liquid. We consider two practical cases: 1) particles are crystals and 2) particles are gas bubbles.

Consider the creation of an unstable boundary layer at the floor or roof of a magmatic chamber caused by thermal or compositionally induced density changes. The viscosity contrast between the buoyant instability (plume) and the ambient liquid controls the rate of entrainment at the plume head, and thus the speed at which plumes mix with the ambient liquid (Bergantz and Ni, 1999; Jellinek et al., 1999). We estimated S_T and Σ_T for olivine crystals in the roof or base of basaltic lava lake (Jellinek and Kerr, 2001) because, in this case, the viscosity contrast is small and the buoyancy flux is high (see Appendix B for calculations). Bergantz and Ni (1999) showed that, under the same conditions, plumes engulf ambient liquid at the head and quickly disperse, creating an efficient mixing front with no recognizable structure. Under these conditions both S_T and Σ_T are well below unity (Table 3), which indicates that crystals are unlikely to exit plumes before plume dispersal. Hence, we do not expect situations in which liquids poorly mix, but crystals disperse widely when the viscosity contrast is small.

On the other hand, a system such as Montserrat (Couch et al., 2001) has a high viscosity contrast between the heated plumes and the colder host liquid, and the shape of plumes change little during ascent, inducing slow mixing (Bergantz and Ni, 1999; Jellinek et al., 1999). We found that orthopyroxenes entrained within instabilities of heated andesite have small values of S_T and Σ_T (Table 3). Crystals thus act as passive tracers and are advected in the buoyant plumes. As the width of the plume tail diminishes, S_T increases, but it is only when the plume width, reduced by stretching during the ascent, becomes on the order of the crystal size that S_T approaches unity. At that point, the plume is almost completely incorporated in the convecting liquid. Hence crystals are unable to leave the instabilities until they completely mix. In summary, crystals are entrained within instabilities regardless of the viscosity contrast between the plumes and the ambient liquid, and crystals move by chaotic advection in convecting magma chambers.

Table 3: Estimates of the dynamic variable of two magmatic mixtures.

variable	unit	Olivine in basalt	Orthopyroxene in andesite
ρ_p	kg m^{-3}	3220	3171
d	mm	2 - 4	1 - 2
μ_f	Pa s	50-200	1.2 10^{6}
μ_m	Pa s	85-2200	2.6 10^{5}
ρ_f	kg m^{-3}	2700	2237
ρ_m	kg m^{-3}	2400	2212
L	m	100	1000
B	m^2 s^{-3}	4.1 10^{-8}	6.5 10^{-10}
Re	min.	23	0.13
	max.	9	0.11
S_T	min.	3.4 10^{-7}	3.3 10^{-11}
	max.	1.8 10^{-4}	1.3 10^{-10}
Σ_T	min.	4.7 10^{-3}	9.2 10^{-7}
	max.	1.9 10^{-2}	3.7 10^{-6}

Volatile exsolution can occur at various stages of magmatism. The density contrast between bubbles in the magmatic liquid requires the assessment of their relative motion to understand the style of degassing in magmatic systems (Huppert and Woods, 2002). Under low yield stress, bubbles can be considered as buoyant, rigid spheres (i.e., the capillary number is below unity, Manga et al., 1998) with calculable S_T and Σ_T. Typical Σ_T range from >1 (basalt) to <<1 (rhyolite). For example, 100 μm bubbles will escape from a rising basaltic liquid slower than 3 cm/s (condition $\Sigma_T > 1$), whereas the same bubbles can be considered immobile with respect to a rhyolitic liquid faster than 3×10^{-7} cm/s. In other words, rising basalt stopped in its progression will lose its exsolved volatiles orders of magnitude faster than its rhyolitic counterpart will, possibly creating a foam layer atop (e.g., Thomas et al., 1993).

6. Conclusions

Multiphase mixtures in magmatic systems can display a range of distinct dynamical regimes that can be characterized with a combination of average (Eulerian) properties and instantaneous (Lagrangian) variables. The Lagrangian acceleration of particles is a function of the viscous drag and gravity forces, and from these two forces are derived the Stokes number (S_T) and the stability number (Σ_T), two dimensionless numbers that describe the dynamic behavior of the particles within the mixture. The Eulerian properties of the mixtures yield the Reynolds number (Re), which characterizes the level of unsteadiness in the continuous phase (liquid or gas).

Pyroclasts and gas is a common volcanic mixture that forms most post-conduit flows such as volcanic plumes and pyroclastic surges. Pyroclastic surges and volcanic plumes have high Reynolds number, and therefore all scales of turbulence (i.e. eddy sizes) are present within these systems. The compilation of 17 experimental studies relevant for surges and plumes indicates that there is a need for experiments above the mixing transition ($Re>10^4$) because lower values of Re imply that parts of the flow feature an incomplete set of eddy sizes, which affects particle transport. We expect complex particle sorting to arise within surges and plumes because each eddy size segregates pyroclasts as a function of their size, which span three orders of magnitude. Eddies whose Stokes and stability numbers are close to unity are most likely to control this sorting, which forms patterns known as mesoscale structures. Particles are efficiently mixed by larger eddies (i.e. with S_T and Σ_T <1), whereas particles decouple and sediment out from smaller eddies (i.e. with S_T and Σ_T >1). Results from the compilation of laboratory studies show that there is a need for scaling S_T and Σ_T in

experimental work, as none of the studies report the values of these two dimensionless numbers. Among the particle dynamic regimes, some deserve special attention, such as the role of mesoscale structures on transport and sedimentary processes in plumes and surges, the applicability of turbulence models below the mixing transition, and the consequences of this transition on particle gathering and dispersal. The relevance of snow avalanche studies for surges is a clear example of the links that can be drawn from the multiphase scaling relations proposed herein.

Crystals and silicate melt compose most magmatic mixtures, which are characterized by dynamic regimes ranging from laminar to transitional. The compilation of 7 experimental studies indicates that in the laminar regime, crystals mostly follow the motion of the melt, and thus the physical state of the system can be approximated as single phase. In the transitional regime, magmas can feature spatially heterogeneous distributions of laminar regions and zones with important velocity gradients because not all scales of fluid motion are present. This heterogeneity has a strong potential for crystals sorting, and not only viscous drag and gravity forces affect crystal trajectories, but also Basset and virtual mass forces.

The Re-S_T-Σ_T framework for dilute multiphase flow demonstrates that, despite numerous experimental studies on processes relevant to magmatic systems, some and perhaps most, geologically important parameter ranges still need to be addressed at the laboratory scale. The combined Eulerian-Lagrangian approach provides a quantitative template for the assessment of the adequate scaling of the interplay between particles and the continuous phase in dilute multiphase magmatic mixtures.

Acknowledgments

We would like to thank SJ Lane and an anonymous reviewer for their helpful suggestions. Funding was provided by the NSF grants EAR-0106441 to GWB and EAR-0309703 to AB. AB was also partially supported by the Volcano Hazards Program of the US Geological Survey, through the Alaska Volcano Observatory.

Appendix A: Truncation of the BBO equation

The Bassinet-Boussinesq-Oseen (BBO) equation expresses the Lagrangian acceleration of a spherical particle in an unsteady flow as the sum of the viscous, gravitational/buoyancy, virtual mass, and Basset forces acting respectively on the particle (Maxey and Riley, 1983; Crowe et al., 1997):

$$\left(1+\frac{\rho_g}{2\rho_p}\right)\frac{dv}{dt}=\frac{f}{\tau_v}(u-v)+g\left(1-\frac{\rho_g}{\rho_p}\right)+\frac{3\rho_g}{2\rho_p}\dot{u}+\sqrt{\frac{9\rho_g}{2\pi\rho_p t_v}}\left[\int_0^t\frac{\dot{u}-\dot{v}}{\sqrt{t-t'}}dt'+\frac{(u-v)_0}{\sqrt{t}}\right] \tag{A1}$$

Where u is the carrier phase velocity, v the particle velocity, ρ_g is the carrier phase density, ρ_p is the particle density, d is its diameter, μ is the carrier phase dynamic viscosity, g is the acceleration of gravity, τ_v is the particle velocity response time (Equ. 4), and f is a drag factor valid over the entire subcritical range of particle Reynolds number ($Re_p \leq 10^5$, Clift and Gauvin, 1970):

$$f=1+0.15Re_p^{0.687}+\frac{0.0175}{1+42500Re_p^{-1.16}} \tag{A2}$$

$$Re_p=\frac{U_T\,d}{\upsilon} \tag{A3}$$

where U_T is the particle terminal fall velocity and υ is the kinematic viscosity of the carrier phase. The BBO equation is not solvable analytically for the particle speed, but some simplifications are possible and lead to the simple scaling laws used herein. Compared to the

viscous drag ($F_{viscous\ drag}$), the virtual mass ($F_{virtual\ mass}$) and Basset (F_{Basset}) forces are on the order of (Maxey and Riley, 1983):

$$F_{Basset} \approx \sqrt{\mathrm{Re}}\frac{d}{L}F_{viscous\ drag} \tag{A4}$$

$$F_{vitrual\ mass} \approx \mathrm{Re}\left(\frac{d}{L}\right)^2 F_{viscous\ drag} \tag{A5}$$

From Equs A1, A4, and A5, we deduce that the virtual mass and Basset forces are negligible for either $Re << 1$, $d << L$, or $\rho_p >> \rho_g$. If any of these conditions are satisfied, it is possible to truncate Equ. A1 and use only the viscous drag and the gravity force (Raju and Meiburg, 1995):

$$\frac{dv}{dt} = \frac{f}{\tau_v}(u-v)\left(\frac{2\rho_p}{2\rho_p+\rho_g}\right) + g\left(\frac{2\rho_p - 2\rho_g}{2\rho_p+\rho_g}\right) \tag{A6}$$

Nondimensionalisation by the carrier phase time scale, which is the characteristic speed change of the carrier phase ΔU over the characteristic distance δ, gives Equ. 1.

Appendix B: Crystal settling in magmas

This appendix presents the details of the scaling of crystals in magmatic chambers. Crystals are entrained within unstable plumes that form at the interface between the injected or heated magma and the host magma. We recognize that the rheologic structure of the magma chamber boundary can be complex (Marsh, 1988, 1989), but will not address that complexity here. For our purposes, we address only the mobile portion of the boundary layer. The Lagrangian scaling requires the characteristic length and velocity scales of these plumes. We take the width of the Rayleigh-Taylor plumes as the length scale of the instabilities (Kerr, 1994; Jellinek et al., 1999):

$$\delta = \frac{\sqrt{6.22\mu_m\rho_f B}}{g(\rho_f - \rho_m)} \tag{B1}$$

where μ_m and ρ_m are the viscosities and density of the boundary layer, ρ_f the density of the host magma, and B is the buoyancy flux (Jellinek and Kerr, 2001):

$$B = \frac{q\alpha g}{\rho_f c_p} \tag{B2}$$

where q is the heat flux, α is the coefficient of thermal expansion, and c_p is the heat capacity of the magma. The velocity scale of the plumes is estimated from the buoyancy Reynolds number (Equ. 11):

$$\Delta U = \frac{B^{1/2}H}{\upsilon^{1/2}} \tag{B3}$$

References

Agrawal, K., Loezos, P.N., Syamlal, M., Sundaresan, S., 2001. The role of meso-scale structures in rapid gas-solid flows. J. Fluid Mech. 445, 151-185.

Anilkumar, A.V., Sparks, R.S.J., and Sturtevant, B., 1993. Geological implications and applications of high-velocity two-phase flow experiments, J. Volcanol. Geotherm. Res. 56, 145-160.

Aref, H., 1990. Chaotic advection of fluid particles. Phil. Trans. Royal Soc. London A333, 273-288.

Bagnold, R.A., 1954. Experiments on a gravity-free dispersion of large solid spheres in a Newtonian Fluid under shear, Proc. Royal Soc. London A225, 49-63.

Bergantz, G.W., 2000. On the dynamics of magma mixing by reintrusion: implications for pluton assembly processes. J. Structural Geol. 22, 1297-1309.

Bergantz, G.W., Breidenthal, R.E., 2001. Non-stationary entrainment and tunneling eruptions: a dynamic template for eruption processes and magma mixing. Geophys. Res. Lett. 28, 3075-3078.

Bergantz, G.W., Ni, J., 1999. A numerical study of sedimentation by dripping instabilities in viscous fluids. Int. J. Multiphase Flow 25, 307-320.

Bonnecaze, R.T., Hallworth, M.A., Huppert, H.E., Lister, J.R., 1995. Axisymmetric particle-driven gravity currents, J. Fluid Mech. 294, 93-121.

Bozhinskiy, A.N., Sukhanov, L.A., 1998. Physical modelling of avalanches using an aerosol cloud of powder materials, Annals Glaciology 26, 242-246.

Brandeis, G., Jaupart, C., 1986. On the interaction between convection and crystallization in cooling magma chambers. Earth Planet. Sci. Lett. 77, 345-361.

Breidenthal, R., 1981. Structure in turbulent mixing layers and wakes using a chemical reaction. J. Fluid Mech. 109, 1-24.

Burgisser, A., Bergantz, G.W., 2002. Reconciling pyroclastic flow and surge: the multiphase physics of pyroclastic density currents. Earth Planet. Sci. Lett. 202, 405-418.

Bursik, M.I., Woods, A.W., 1996. The dynamics and thermodynamics of large ash flows. Bull. Volcanol. 58, 175-193.

Cardoso, S.S.S., Zarrebini, M., 2001. Convection driven by particle settling surrounding a turbulent plume, Chem. Engin. Sc. 56, 3365-3375.

Carey, S.N., 1991. Transport and deposition of tephra by pyroclastic flows and surges. In: Fisher, R.V., Smith, G.A. (Editors), Sedimentation in volcanic settings. Soc. Sedimentary Geol. Spec. Publ. 45, Tulsa, 39-57.

Carey, S.N., Sigurdsson, H., Sparks, R.S.J., 1988. Experimental studies of particle-laden plumes, J. Geophys. Res. 93, 15314-15328.

Choux, C.M., Druitt, T.H., 2002. Analogue study of particle segregation in pyroclastic density currents, with implications for the emplacements mechanisms of large ignimbrites, Sedimentology 49, 907-928.

Clift, R., Gauvin, W.H., 1970. The motion of particles in turbulent gas streams. Proc. Chemeca '70, 14-28.

Couch, S., Sparks, R.S.J., Carroll, M.R., 2001. Mineral disequilibrium in lavas explained by convective self-mixing in open magma chambers. Nature 411, 1037-1039.

Crowe, C., Sommerfeld, M., Tsuji Y., 1997. Multiphase flows with droplets and particles. CRC Press.

Dimotakis, P.E., 2000. The mixing transition in turbulent flows. J. Fluid Mech. 409, 69-98.

Dimotakis, P.E., Catrakis, H.J., 1999. Turbulence, fractals, and mixing. In: Chate, H., Villermaux, E., Chomaz, J.-M. (Editors), Mixing, chaos and turbulence. NATO ASI Series B: Physics 373, 59-144.

Ernst, G.G.J., Sparks, R.S.J., Carey, S.N., Bursik, M.I., 1996. Sedimentation from turbulent jets and plumes, J. Geophys. Res. 101, 5575-5589.

Fisher, R.V., 1983. Flow transformations in sediment gravity flows. Geology 11, 273-274.

Flinders, J., Clemens, J.D., 1996. Non-linear dynamics, chaos, complexity and enclaves in granitoid magmas. Trans. Royal Soc. Edinburgh: Earth Sci. 87, 217-223.

Ghosh, J.K., Mazumder, B.S., Saha, M.R., Sengupta, S., 1986. Deposition of sand by suspension currents: experimental and theoretical studies. J. Sediment. Petrology 56, 57-66.

Ghosh, J.K., Mazumdmer, B.S., Sengupta, S., 1981. Methods of computation of suspended load from bed materials and flow parameters, Sedimentology 28, 781-791.

Hazen, A., 1904. On sedimentation, Trans. Am. Soc. Civil Engineers 53, 45-88.

Hogan, R.C., Cuzzi, J.N., 2001. Stokes and Reynolds number dependence of preferential particle concentration in simulated three-dimensional turbulence. Physics Fluids 13, 2938-2945.

Hogg, A.J., Huppert, H.E., 2001. Two-dimensional and axisymmetric models for compositional and particle-driven gravity currents in uniform ambient flows. Spec. Publ. Int. Assoc. Sedimentology 31, 121-134.

Hoyal, D.C.J.D., Bursik, M.I., Atkinson, J.F., 1999. Settling-driven convection: A mechanism of sedimentation from stratified fluids, J. Geophys. Res. 104, 7953-7966.

Hunt, J.N., 1954. The turbulent transport of suspended sediment in open channels, Proc. Royal Soc. London A224, 322-335.

Hunt, J.N., 1969. On the turbulent transport of a heterogeneous sediment. Quarterly J. Mech. Appl. Math. 22, 235-246.

Huppert, H.E., Kerr, R.C., Lister, J.R., Turner, J.S., 1991. Convection and particle entrainment driven by differential sedimentation, J. Fluid Mech. 226, 349-369.

Huppert, H.E., Sparks, R.S.J., Turner, J.S., 1983. Laboratory investigations of viscous effects in replenished magma chambers, Earth Planet. Sci. Let. 65, 377-381.

Huppert, H.E., Woods, A., 2002. The role of volatiles in magma chamber dynamics. Nature 420, 493-495.

Jaupart, C., Tait, S., 1995. Dynamics of differentiation in magma reservoirs, J. Geophys. Res. 100, 17615-17636.

Jellinek, A.M., Kerr, R.C., 1999. Mixing and compositional stratification produced by natural convection 2. Applications to the differentiation of basaltic and silicic magma chambers and komatiite lava flows. J. Geophys. Res. 104, 7203-7218.

Jellinek, A.M., Kerr, R.C., 2001. Magma dynamics, crystallization, and chemical differentiation of the 1959 Kilauea Iki lava lake, Hawaii, revisited. J. Volcanol. Geotherm. Res. 110, 235-263.

Jellinek, A.M., Kerr, R.C., Griffiths, R.W., 1999. Mixing and compositional stratification produced by natural convection 1. Experiments and their application to Earth's core and mantle. J. Geophys. Res. 104, 7183-7201.

Jobson, H.E., Sayre, W.W., 1970. Vertical transfer in open channel flow, Journal of the Hydraulic Division, Proc. Am. Soc. Civil Engineers 96, 703-724.

Jopling, A.V., 1964. Laboratory study of sorting processes related to flow separation. J. Geophys. Res. 69, 3403-3418.

Kaminski, E., Jaupart, C., 1997. Expansion and quenching of vesicular magma fragments in Plinian eruption. J. Geophys. Res. 102, 12187-12203.

Kerr, R.C., 1994. Dissolving driven by vigorous compositional convection, J. Fluid Mech. 280, 287-302.

Konrad, J.H., 1976. An experimental investigation of mixing in two-dimensional turbulence flows with application to diffusion-limited chemical reactions. Ph.D. thesis, California Institute of Technology, Project SQUID Tech. Rep. CIT-8-PU.

Koyaguchi, T., Hallworth, M.A., Huppert, H.E., Sparks, R.S.J., 1990. Sedimentation of particles from a convecting fluid, Nature 343, 447-450.

Liu, M., Muzzio, F.J., Peskin, R.L., 1995. Quantification of mixing in aperiodic chaotic flows. In: Aref, H., El Naschie, M.S. (Editors) Chaos applied to fluid mixing. Pergamon, 125-149.

Manga, M., Castro, J., Cashman, K.V., Loewenberg, M., 1998. Rheology of bubble-bearing magmas. J. Volcanol. Geotherm. Res. 87, 15-28.

Marsh, B.D, 1989. On convective style and vigor in sheet-like magma bodies. J. Petrology 30, 479-530.

Marsh, B.D., 1988. Crystal capture, sorting, and retention in convecting magma. Geol. Soc. Am. Bull. 100, 1720-1737.

Marsh, B.D., Maxey, M.R., 1985. On the distribution and separation of crystals in convecting magma. J. Volcanol. Geotherm. Res. 24, 95-150.

Martin, D., 1990. Crystal settling and in situ crystallization in aqueous solutions and magma chambers, Earth Planet. Sci. Let. 96, 336-348.

Martin, D., Nokes, R., 1988. Crystal settling in vigorously convecting magma chamber. Nature 332, 534-536.

Martin, D., Nokes, R., 1989. A fluid-dynamical study of crystal settling in convecting magmas. J. Petrology 90, 1471-1500.

Martin, J.E., Meiburg, E., 1994. The accumulation and dispersion of heavy particles in forced two dimensional mixing layers. I. The fundamental and subharmonic cases. Phys. Fluids 6, 116-1132.

Maxey, M.R., Riley, J.J., 1983. Equation of motion for a small rigid sphere in a nonuniform flow. Phys. Fluids 26, 883-889.

Niño, Y., Lopez, F., Garcia, M., 2003. Threshold for particle entrainment into suspension. Sedimentology 50, 247-263.

Ottino, J.M., 1990. The kinematics of mixing: Stretching, chaos, and transport, Cambridge Texts in Applied Mathematics, Cambridge University Press, 364 p.

Paiement-Paradis, G., Buffin-Bélanger, T., Roy, A.G., 2003. Scalings for large turbulent flow structures in gravel-bed rivers. Geophys. Res. Lett. 30, 10.1029/2003GL017553.

Papp, K., 2002. An analysis of volcanic ash plume movement and dispersion within the North Pacific. M.S. Thesis, University of Alaska Fairbanks, 162 p.

Perugini, D., Giampiero, P., 2000. Chaotic dynamics and fractals in magmatic interaction processes: a different approach to the interpretation of mafic microgranular enclaves. Earth Planet. Sci. Lett. 175, 93-103.

Perugini, D., Poli, G., Gatta, G.D., 2002. Analysis and simulation of magma mixing processes in 3D. Lithos 65, 313-330.

Perugini, D., Poli, G., Mazzuoli, R., 2003. Chaotic advection, fractals and diffusion during mixing of magmas: evidence from lava flows. J. Volcanol. Geotherm. Res. 124, 255-279.

Pope, S.B., 2000. Turbulent Flows, Cambridge University Press, 771 p.

Raju, N., Meiburg, E., 1995. The accumulation and dispersion of heavy particles in forced two-dimensional mixing layers. Part 2: The effect of gravity. Phys. Fluids 7, 1241-1264.

Rudman, M., 1992. Two-phase natural convection: implications for crystal-settling in magma chambers. Phys. Earth Planet. Interiors 72, 153-172.

Searcy, C., Dean, K., Stringer, W., 1998. PUFF: A high-resolution volcanic ash tracking model. J. Volcanol. Geotherm. Res. 80, 1-16.

Simakin, A., Schmeling, H., Trubitsyn, V., 1997. Convection in melts due to sedimentary crystal flux from above. Phys. Earth Planet. Interiors 102, 185-200.

Simakin, A., Trubitsyn, V., Schmeling, H., 1994. Structure of the upper boundary layer of a solidifying intrusion with crystal sedimentation. Earth Planet. Sci. Lett. 126, 333-349.

Smith, M.K., 1988. Thermal convection during the directional solidification of a pure liquid with variable viscosity. J. Fluid Mech. 188, 547-570.

Snyder, D., 2000. Thermal effects of the intrusion of basaltic magma into a more silicic magma chamber and implications for eruption triggering. Earth Planet. Sci. Lett. 175, 257-273.

Solomon, T.H., Mezic, I., 2003. Uniform resonant chaotic mixing in fluid flows. Nature 425, 376-380.

Sparks, R.S.J., Barclay, J., Calder, E.S., Herd, R.A., Komorowski, J.C., Luckett, R., Norton, G.E., Ritchie, L.J., Voight, B., Woods, A.W., 2002. Generation of a debris avalanche and violent pyroclastic density current on 26 December (Boxing Day) 1997 at Soufriere Hills volcano, Montserrat. In: Druitt, T.H., Kokelaar, B.P. (Editors), The Eruption of the Soufriere Hills Volcano, Montserrat 1995 to 1999. Geol. Soc. London Mem. 21, 409-434.

Sparks, R.S.J., Bursik, M.I., Carey, S.N., Gilbert, J.S., Glaze, L.S., Sigurdsson, H., Woods, A.W., 1997. Volcanic plumes, John Wiley & Sons, 574 p.

Sparks, R.S.J, Carey, S.N., Sigurdsson, H., 1991. Sedimentation from gravity currents generated by turbulent plumes, Sedimentology 38, 839-856.

Sparks, R.S.J., Huppert, H.E., Turner, J.S., 1984. The fluid dynamics of evolving magma chambers. Phil. Trans. Royal Soc. London A310, 511-534.

Stix, J., 2001. Flow evolution of experimental gravity currents: Implications for pyroclastic flows at volcanoes, J. Geology 109, 381-398.

Thomas, N., Tait, S., Koyaguchi, T., 1993. Mixing of stratified liquids by the motion of gas bubbles: application to magma mixing. Earth Planet. Sci. Lett. 115, 161-175.

Turner, J.S., Gustafson, L.B., 1981. Fluid motions and compositional gradients produced by crystallization or melting at vertical boundaries, J. Volcanol. Geotherm. Res. 11, 93-125.

Valentine, G., 1987. Stratified flow in pyroclastic surges. Bull. Volcanol. 49, 616-630.

Weinstein, S.A., Yuen, D.A., Olson, P.L., 1988. Evolution of crystal-settling in magma-chamber convection, Earth Planet. Sci. Let. 87, 237-248.

Woods, A.W., Bursik, M.I., Kurbatov, A.V., 1998. The interaction of ash flows with ridges. Bull. Volcanol. 60, 38-51.

Zhang, D.Z., VanderHeyden, W.B., 2002. The effect of mesoscale structures on the macroscopic momentum equations for two-phase flows. Int. J. Multiphase Flow 28, 805-822.

Experimental Constraints on Degassing and Permeability in Volcanic Conduit Flow

ALAIN BURGISSER
Alaska Volcano Observatory
Geophysical Institute
University of Alaska Fairbanks

JAMES E. GARDNER
Department of Geological Sciences,
The University of Texas at Austin

Publié dans: Bulletin of Volcanology (2005) v. 67, p. 42-56.

Abstract

This study assesses the effect of decompression rate on two processes that directly influence the behavior of volcanic eruptions: degassing and permeability in magmas. We studied the degassing of magma with experiments on hydrated natural rhyolitic glass at high pressure and temperature. From the data collected, we defined and characterized one degassing regime in equilibrium and two regimes in disequilibrium. Equilibrium bubble growth occurs when the decompression rate is slower than 0.1 MPa s^{-1}, while higher rates cause porosity to deviate rapidly from equilibrium, defining the first disequilibrium regime of degassing. If the deviation is large enough, a critical threshold of super-saturation is reached and bubble growth accelerates, defining the second disequilibrium regime. We studied permeability and bubble coalescence in magma with experiments using the same rhyolitic melt in open degassing conditions. Under these open conditions, we observed that bubbles start to coalesce at ~43 vol.% porosity, regardless of decompression rate. Coalescence profoundly affects bubble texture and size distributions, and induces the melt to become permeable. We determined coalescence to occur on a time scale (~180 s) independent of decompression rate. We parameterized and incorporated our experimental results into a 1D conduit flow model to explore the implications of our findings on eruptive behavior of rhyolitic melts with low crystal contents stored in the upper crust. Compared to previous models that assume equilibrium degassing of the melt during ascent, the introduction of disequilibrium degassing reduces the deviation from lithostatic pressure by ~ 25 %, the acceleration at high porosities (> 50 vol.%) by a factor 5, and the associated decompression rate by an order of magnitude. The integration of the time scale of coalescence to the model shows that the transition between explosive and effusive eruptive regimes is sensitive to small variations of the initial magma ascent speed, and that flow conditions near fragmentation may significantly be affected by bubble coalescence and gas escape.

1. Introduction

The dynamics of bubble growth, although occurring on a small scale, directly affect the large-scale behavior of volcanic eruptions. Bubbles are present because water supersaturates in a magmatic liquid rising from depth, and water exsolution into the bubbles is the driving force that controls the growth of bubbles in the volcanic conduit. That growth causes the flow density to decrease, decompression rate to increase, and hence the flow to accelerate, possibly leading to an explosive eruption. Since the early work of Sparks (1978), bubble growth dynamics has been explored through increasingly complex numerical models (e.g., Barclay et al. 1995; Lyakhovsky et al. 1996; Proussevitch et al. 1993a; Proussevitch and Sahagian 1998; Sparks et al. 1994; Toramaru 1989; 1995) and experimental work (e.g., Gardner et al. 1999; 2000; Mangan and Sisson 2000).

Because of the complex interdependences of the variables involved, many of the processes involved in bubbles growth remain unclear. In particular, the relation between growth and decompression rate and the role of bubble coalescence (or connectivity) are two poorly constrained processes that directly affect conduit flow dynamics. The highest decompression rates are suggested to arise in the conduit when bubbles grow in equilibrium with the magmatic liquid (Woods 1995). If equilibrium between bubbles and liquid is not maintained, however, the decrease in density of the mixture is reduced, which in turn reduces the decompression rate and flow acceleration. Bubble coalescence controls magma permeability, and possibly the transition between explosive and effusive eruptive regimes (Yoshida and Koyaguchi 1999). If the magma can become permeable and lose part or all of its gas without fragmenting, it reduces its porosity, thus limiting further acceleration and possibly leading to effusive eruption (Eichelberger et al. 1986).

We conducted experiments on hydrated natural rhyolitic glass at high pressure and temperature, which allowed us to assess the effect of decompression rate on *1)* bubble growth and *2)* bubble coalescence. From experiments run under closed degassing conditions, we defined and characterized one growth regime in equilibrium and two regimes in disequilibrium. From experiments using the same rhyolitic melt in open degassing conditions, we determined the onset of bubble coalescence through its profound effect on bubble texture and size distributions. We determined the rate at which coalescence affects the bubble size distribution and linked coalescence to melt permeability. Finally, we parameterized and incorporated our experimental results into a 1D conduit flow model to explore the implications of our findings on eruptive behavior. We discuss the consequences of disequilibrium degassing for conduit flow dynamics, and the role of connectivity in the transition between effusive and explosive regimes.

2. Methods

We conducted experiments on natural rhyolitic glass from the Panum Crater Dome (PCD; 75.6 wt.% SiO_2 in glass, Mangan and Sisson 2000; Westrich and Eichelberger 1994). Small cores (~ 7 mm length) were filed to fit into 3-mm diameter gold tubing. The tubing was welded shut after adding about 8 wt.% de-ionized water, to ensure saturation at the start of decompression (saturated value: 4.21 wt.% at 825 °C and 150 MPa, this study). Capsules were weighed before and after welding to ensure that no water was lost. Capsules were then placed in an externally heated pressure vessel fitted with a rapid-quench attachment, where they remained at 825 °C and 150 MPa for 5 days to allow the cores to saturate with water (Fig. 1). We ensured that runs quenched after this hydration period were bubble-free (see open-degassing runs below).

After the 5-days hydration, one set of samples (22 runs, Table 1) was decompressed instantaneously to 100 MPa and held for 15 minutes, which ensured the presence of a bubble population in equilibrium with the melt that is not influenced by nucleation kinetics. The samples were then isothermally decompressed from 100 MPa at rates that increased with lower pressure. Decompression rates were obtained by dropping instantly the appropriate

amount of pressure every few seconds in a step-wise fashion to approximate a linear behavior between the pressures of interest. The time step was 20 s for all runs, except for the two fastest rates, 1 and 10 MPa s^{-1}, which were obtained by 10 and 3 s steps, respectively. Lowering the sample into the water-cooled base of the vessel after the final decompression step quenched the samples. Errors on the pressures are less than 0.1 MPa and errors on the decompression rate are less than 5%, except for the fastest rate (20%).

A second set of samples (16 runs, Table 2) was quenched at 150 MPa after 5-days hydration. After inspection under microscope to ensure that the cores were bubble-free, the cores were reloaded into capsules without water, but with either silicate glass (powdered PCD rhyolitic glass) or MgO powder to serve as a sink for expelled water during decompression, allowing open-degassing conditions (Fig. 1). The capsules were then pressurized at 155 MPa and reheated to 825 °C for 5 minutes, decompressed instantaneously to 100 MPa and held for 15 minutes, and finally decompressed at constant rates to lower pressure and quenched. Errors on pressure and decompression rate are the same than that of the first set of runs.

The diameters of all bubbles within a given volume in thin section were measured using digital images (640×480 pixels) acquired in transmitted light. In the case of the deformed bubbles produced by connectivity, the diameter of a volume-equivalent sphere was taken. The size distribution of bubbles (BSD) of each sample (~ 150 bubbles) was constructed with three to six images, depending on bubble size. The number density of bubbles (BND) of each sample was calculated by multiplying the mean bubble volume given by the BSD with the value of porosity obtained for that sample (Gardner et al. 1999). Porosities were measured using similar digital images of thin sections acquired in reflected light. Errors in porosities were estimated from three images for most samples. Bubbles nucleated heterogeneously, in part on the Fe-Ti oxides present in the melt. Replicate runs show that the nucleated bubbles were similar in number in each experiment. We thus use changes in the BND to monitor for further nucleation and degree of coalescence during decompression.

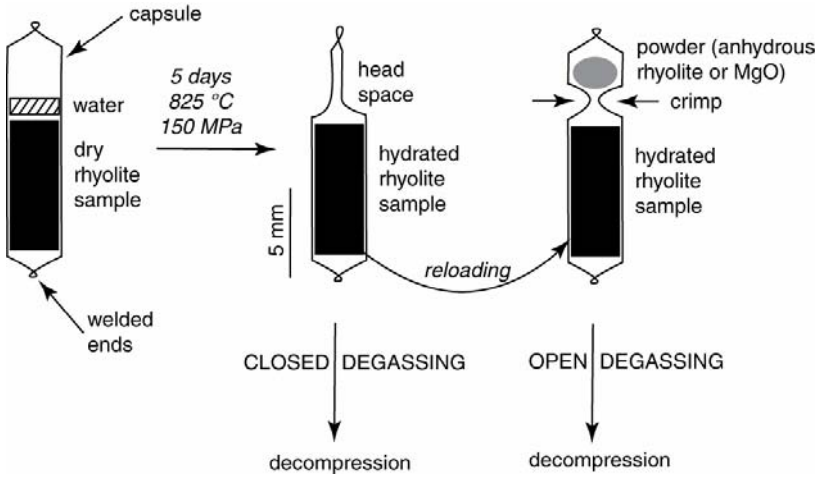

Figure 1 Schematic cross-section of the capsules used in the experimental setup. Rhyolite cores were hydrated for 5 days at high pressure and temperature (left). In closed degassing conditions, samples were decompressed after hydration (center). Open degassing conditions were created by reloading the samples in a new capsule with an anhydrous powder (right) and reheating/pressurizing the capsule before decompression.

Table 1: Experimental conditions for closed degassing experiments

run[a]	decompression rate[b] (MPa s^{-1})	quench pressure (MPa)	porosity[c] (vol.%)	bubble mean diameter[c] (μm)	number of bubbles	BND[d] ($\times 10^5$ cm^{-3})
ABG1	-	100	5.6 (0.2)	35 (7)	149	18
ABG6	0.1	80	13.3 (1.1)	60 (14)	173	10
ABG4	0.15	80	6.4 (0.7)	34 (7)	170	29
ABG2	0.1	60	21.8 (0.8)	60 (11)	127	17
ABG7	0.15	60	17.5 (1.3)	49 (9)	162	25
ABG8	0.1 (100-60)	40	33.0 (2.3)	67 (16)	165	17
ABG3	0.1 (100-60)	40	26.9 (4.5)	103 (16)	163	4
ABG9	0.1 (100-60)	30	49.7 (2.3)	109 (22)	145	6
ABG11	0.1 (100-60)	30	34.5 (2.7)	71 (13)	154	16
ABG20	0.5	90	5.5 (1.2)	34 (7)	169	22
ABG14	0.5	80	6.7 (0.2)	38 (6)	152	22
ABG25	0.5	70	12.3 (1.4)	61 (11)	157	91
ABG15	0.5	60	19.1 (1.3)	63 (9)	163	14
ABG16	0.5	50	23.9 (0.4)	71 (8)	167	11
ABG30	0.5	30	44.2 (0.8)	60 (11)	145	35
ABG32	0.5	10	78.8 (1.7)	140 (32)	48	5
ABG26	1	70	10.4 (0.9)	36 (7)	193	40
ABG27	1	60	17.0 (1.1)	35 (8)	167	56
ABG28	1	50	23.5 (1.2)	56 (8)	163	25
ABG31	1	40	29.3 (1.2)	51 (12)	167	15
ABG29	1	30	42.2 (1.2)	77 (14)	61	32
ABG33	10	40	22.0 (0.8)	59 (11)	183	18

[a] All runs were hydrated at 825 °C for 5 days.
[b] When applicable, decompression rates are given with the corresponding pressure ranges in parenthesis.
[c] Porosities and bubble mean diameters are given with ± 1 σ in parenthesis.
[d] BND are bubble number densities.

Table 2: Experimental conditions for open degassing experiments

run[a]	decompression rate (MPa s^{-1})	quench pressure (MPa)	porosity[b] (vol.%)	bubble mean[b] diameter (μm)	number of bubbles	BND[c] ($\times 10^5$ cm^{-3})
PPE6	0.025	60	39.2 (2.0)	176 (39)	27	1.2
PPE2	0.025	44	46.1 (1.9)	218 (57)	39	0.6
PPE4	0.025	40	51.2 (4.8)	111 (16)	127	5.8
PPE5	0.025	36	52.8	226 (71)	27	0.5
PPE7	0.025	34	63.2	143 (33)	89	3.8
PPE1	0.025	30	30.2 (8.1)	124 (119)	37	0.4
PPE10	0.025	28	62.3 (10.1)	302 (102)	18	0.4
PPE11	0.025	24	85.3 (2.6)	385 (152)	12	0.2
G318	0.1	36	44.0	106 (49)	61	5.4
G322	0.1	30	41.3	90 (108)	50	0.9
G321	0.1	24	43.3 (4.7)	81 (15)	135	13.7
G323	0.1	18	50.1	113 (62)	92	3.0
G300	0.5	30	35.2	77 (25)	107	11.0
G303	0.5	25	42.4 (4.8)	62 (42)	136	8.9
G327	0.5	20	52.9 (4.7)	65 (52)	152	6.8
G328	0.5	15	62.2 (2.0)	72 (77)	166	3.6

[a] All runs were hydrated at 825 °C for 5 days.
[b] When available, porosities and bubble mean diameters are given with ± 1 σ in parenthesis.
[c] BND are bubble number densities.

3. Experimental results

On the basis of run AGB1 (Table 1), we conclude that the instantaneous pressure drop from the saturation pressure of 150 to 100 MPa at the beginning of each run created a unimodal population of bubbles. The melt features about 0.1 vol.% of crystals that are Fe-Ti oxides rods of ~10 μm in length. Both the modest initial super-saturation pressure (50 MPa) and the fact that most of the bubbles are attached to crystals suggest bubbles nucleated heterogeneously at the beginning of each run in both experimental sets (Hurwitz and Navon 1994). The number densities of bubbles in all the decompression runs are between 10^5-10^6 cm^{-3}, which confirm the reproducibility of nucleation conditions (Table 1). Such densities correspond to a mean bubble diameter of ~35 μm at 100 MPa (ABG1, Table 1). The upper part of each sample in both experimental sets contains elongated bubbles (Fig. 2). This region is more pronounced at low pressure, but is always smaller than a quarter of the total sample height. As discussed in *Regimes of Bubble Growth* (below), the likely cause of the elongation is the volumetric expansion of the sample within the gold capsule that forces the melt upward (cf. Fig. 1). We avoided this region when making porosity and BSD determinations.

Figure 2 Reflected light microphotograph of the upper 2 mm of run G318 (Table 2). Bubbles are deformed because the melt has been squeezed up in the capsule headspace by volumetric expansion. Note that this type of extrusion occurs in both open and closed degassing conditions. This open degassing sample illustrates the catalyzing effect of shear on coalescence. Note that the large, coalesced bubbles are restricted to the upper half of the photograph, where the shear was highest.

3.1. Closed degassing runs

We built a set of experiments to assess the maximum decompression rates that permit equilibrium degassing. For each 20 MPa drop, the highest rate that maintained equilibrium was determined (Fig. 3). The porosity at equilibrium is calculated from the difference in water saturation between the initial pressure and a given pressure (cf. Equ. A8 in the *Appendix*). For example, the runs ABG3 and ABG8 both maintained equilibrium porosities at 0.1 MPa s^{-1} down to 60 MPa and were further decompressed to 40 MPa at 0.2 MPa s^{-1} and 0.15 MPa s^{-1}, respectively (Table 1). The former had a value of porosity less than expected from equilibrium, whereas the latter reached equilibrium porosity. The maximum decompression rate for the increment from 60 MPa down to 40 MPa is thus 0.175 ± 0.025 MPa s^{-1}. We find that the maximum rates that guarantee equilibrium degassing range between 0.125 ± 0.025 MPa s^{-1} at high pressure (60-100 MPa) and 0.175 ± 0.025 MPa s^{-1} at low pressure (30-60 MPa, Fig. 3). We note that slower decompressions would all ensure equilibrium because these rates are maxima, and that they correspond to ascent velocities under a lithostatic load of ~6 m s^{-1}.

We then explored the consequences on bubble growth of a constant decompression rate that exceeds the maximum equilibrium rate. After an initial pressure drop to 100 MPa, we decompressed the runs at constant rates (0.5, 1, and 10 MPa s^{-1}, Table 1), quenching samples successively in 10 MPa increments (Figs. 4 and 5). From the successive values of how much porosity deviated from equilibrium, two distinct disequilibrium bubble growth regimes can be defined (Fig. 6). A *slow growth rate* regime occurs as the decompression rate first exceeds that of equilibrium. In this regime, porosity increasingly deviates from equilibrium as pressure decreases, but the magnitude of deviation does not change with decompression rate (Fig. 5). The slow growth can be illustrated by comparing the mean bubble diameter of a run in disequilibrium with its equilibrium counterpart, correcting for the difference in bubble number densities by multiplying the mean diameter by the ratio of the respective BND. At 80 MPa, for example, the mean bubble diameter reaches 38 μm in the slow growth regime (ABG20, Table 1) instead of $60\times(10/22)^{1/3}$=48 μm in equilibrium (ABG6). A *fast growth rate* regime occurs where the magnitude of the deviation from equilibrium diminishes and finally vanishes at high porosities. In this regime, the faster pressure decreases, the faster bubbles grow (Fig. 5).

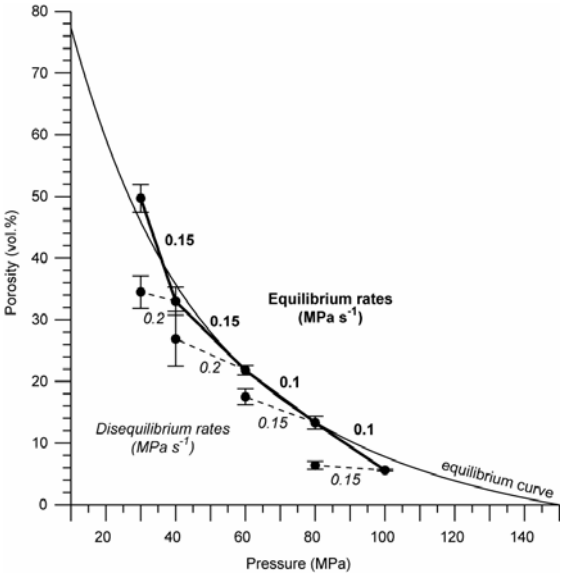

Figure 3 Porosity as a function of quench pressure for variable decompressions rates. Dashed lines indicate disequilibrium degassing over a given pressure interval, and solid lines indicate equilibrium degassing over the interval. The equilibrium degassing porosity curve is calculated from Equ. A8 (see *Appendix* for details). Error bars are omitted when smaller than the symbol size.

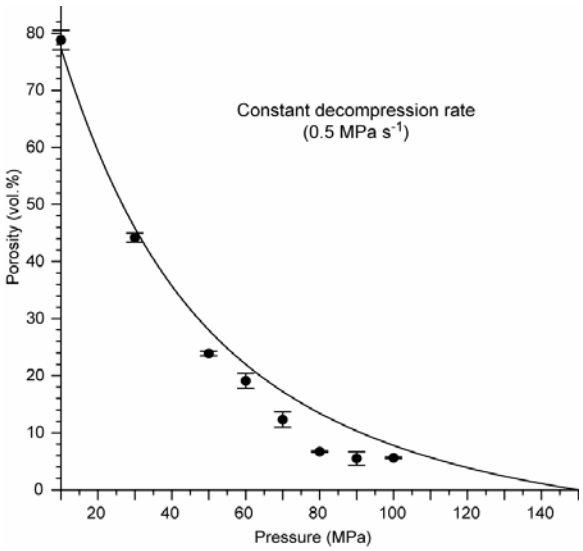

Figure 4 Porosity as a function of quench pressure for a constant decompression rate of 0.5 MPa s^{-1}. The imposed rate forces disequilibrium degassing, as illustrated by the deviation of the sample porosities from the equilibrium curve (Equ. A8 in the *Appendix*). Note that runs with high porosities are back to equilibrium. Error bars are omitted when smaller than the symbol size.

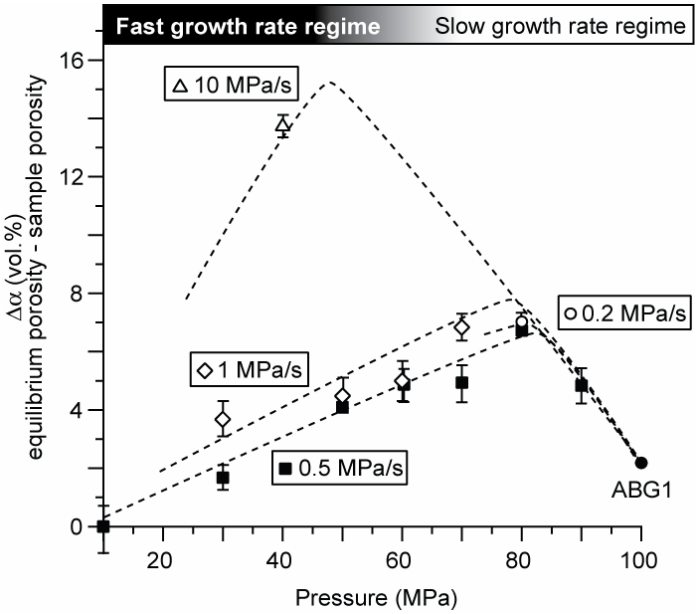

Figure 5 Porosity deviation from equilibrium degassing ($\Delta\alpha$) for various linear decompression rates. The y-axis corresponds to the degree of super-saturation and dashed lines to the regressions used in the model. Regressions were carried out using the linearity of the slow growth regime and the assumption that super-saturation vanishes at atmospheric pressure (see text). Error bars are omitted when smaller than the symbol size.

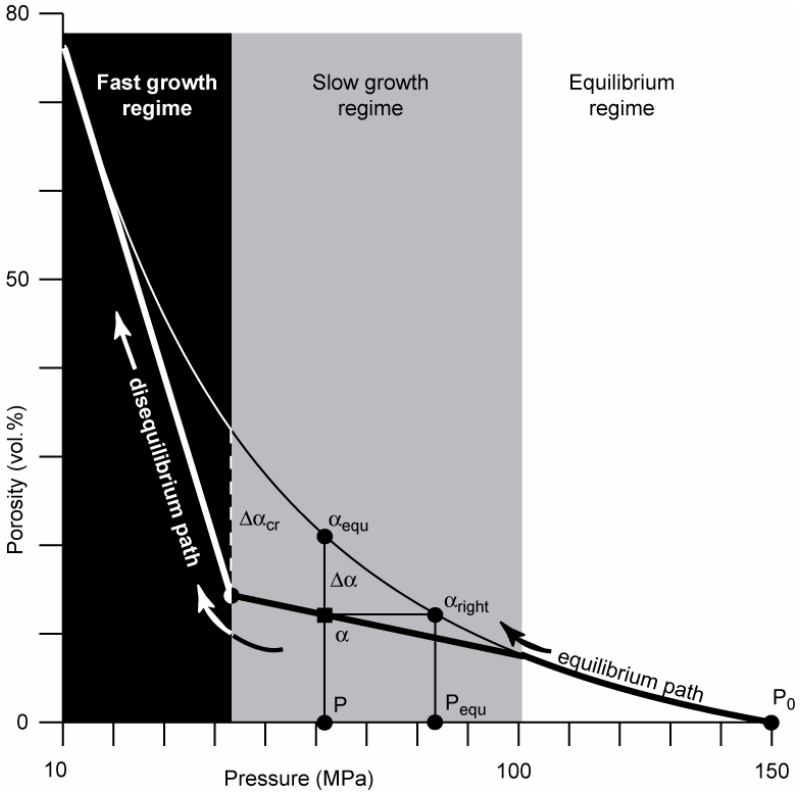

Figure 6 Schematic representation of magma degassing as seen in this study. The different symbols define the variables used in the description of disequilibrium degassing runs and in the conduit flow model. α and P are the respective porosity and pressure at the point of interest, α_{equ} is the equilibrium porosity at a given P, $\Delta\alpha$ is the difference between α_{equ} and α, α_{right} and P_{equ} are the respective equilibrium porosity and pressure at a given α, and $\Delta\alpha_{cr}$ is the critical super-saturation that delimits the fast and slow growth regimes.

3.2. Open degassing runs

We explored the relationship between bubble coalescence and decompression rates, using an experimental setup that allowed open degassing conditions (Fig. 1). At high quench pressure, we observe that bubbles are aligned, forming chains of typically less than 20 unconnected bubbles (40 and 44 MPa runs in Fig. 7a). This spatial distribution differs noticeably from the random distribution of the bubbles present in closed-degassing runs. At low quench pressure, large bubbles have deformed shapes with low curvature surfaces (30 and 28 MPa runs in Fig. 7a). In most cases, these large bubbles are the product of the coalescence of two or more smaller bubbles, the original shapes of which can still be distinguished (e.g., 28 MPa run in Fig 7a). At slow decompression rates (0.025 MPa s^{-1}), this change in bubble texture is dramatic (Fig. 7a), whereas the change is more progressive at higher decompression rates (0.1 MPa s^{-1} and 0.5 MPa s^{-1}, Fig. 7b).

In runs loaded with anhydrous rhyolite powder (Fig. 1), the powder melted during reheating to create a spherule of glass. At low quench pressure (<30 MPa), the spherules had a rim of bubbles, suggesting they absorbed water during the decompression. Since the only available excess water was within the hydrated samples, these rimmed spherules confirm gas was released from those samples. No analysis for absorbed water was conducted on the MgO powder because runs loaded with MgO displayed identical bubble textures than the ones loaded with rhyolite, suggesting a similar gas escape occurred. At a given quench pressure, the porosity values of open degassing runs are lower and more widespread than the ones of closed degassing runs at 0.1 MPa s^{-1} and 0.5 MPa s^{-1}, which is consistent with the melt being permeable (Table 2). Most porosity values at 0.025 MPa s^{-1} are higher than the equilibrium values. Although no satisfying explanation has been found for this shift, we note that the sample quenched just after having coalesced (PPE10) has a porosity 30 vol.% lower than its immediate neighbors, proving the link between coalescence and permeability. Therefore, the evidence of released water, the abundant coalesced bubbles, and the congruent decrease in porosity indicate that the melt was permeable at low pressure.

Bubble sizes record quantitatively the profound textural changes caused by connectivity (Fig. 8a). If we define the start of coalescence when the ratio of mean bubble diameter to the standard deviation of the BSD is close to unity, it occurs between 34 and 30 MPa (41 and 46 vol.%) at 0.025 MPa s^{-1}, between 36 and 30 MPa (40 and 46 vol.%) at 0.1 MPa s^{-1}, and between 30 and 25 MPa (44 and 50 vol.%) at 0.5 MPa s^{-1}. It thus appears that connectivity starts at 43 ± 3 vol.%, regardless of decompression rate or run duration.

Bubble size distributions change dramatically from disconnected to connected runs (Fig. 8a). At low porosity, we note that the size distributions of bubbles in open degassing runs have a similar Gaussian shape, but a broader distribution than observed in closed system runs (Fig. 8b). At higher porosity, large bubble sizes appear in the distribution, the large end of which can be better described with a power law spanning up to one order of magnitude (Fig. 8c). The absence of the original peak around 200 μm in the distribution (Fig. 8a) leads us to qualify those runs as *completely connected* (<30 MPa). Size distributions of samples with porosities above 60 vol.% are uncertain, because of the low number of bubbles present (Table 2). The size distribution thus shifts from Gaussian to power-law as coalescence progresses, but unfortunately, the exact shape of the distribution of completely connected samples cannot be determined with certainty. Nevertheless, the size distributions of completely connected runs seem unchanged by further decompression, despite the high porosities reached (Fig. 8a). The bubble number densities of open-system equilibrium runs are similar to closed-system runs and do not significantly vary with coalescence (Table 2).

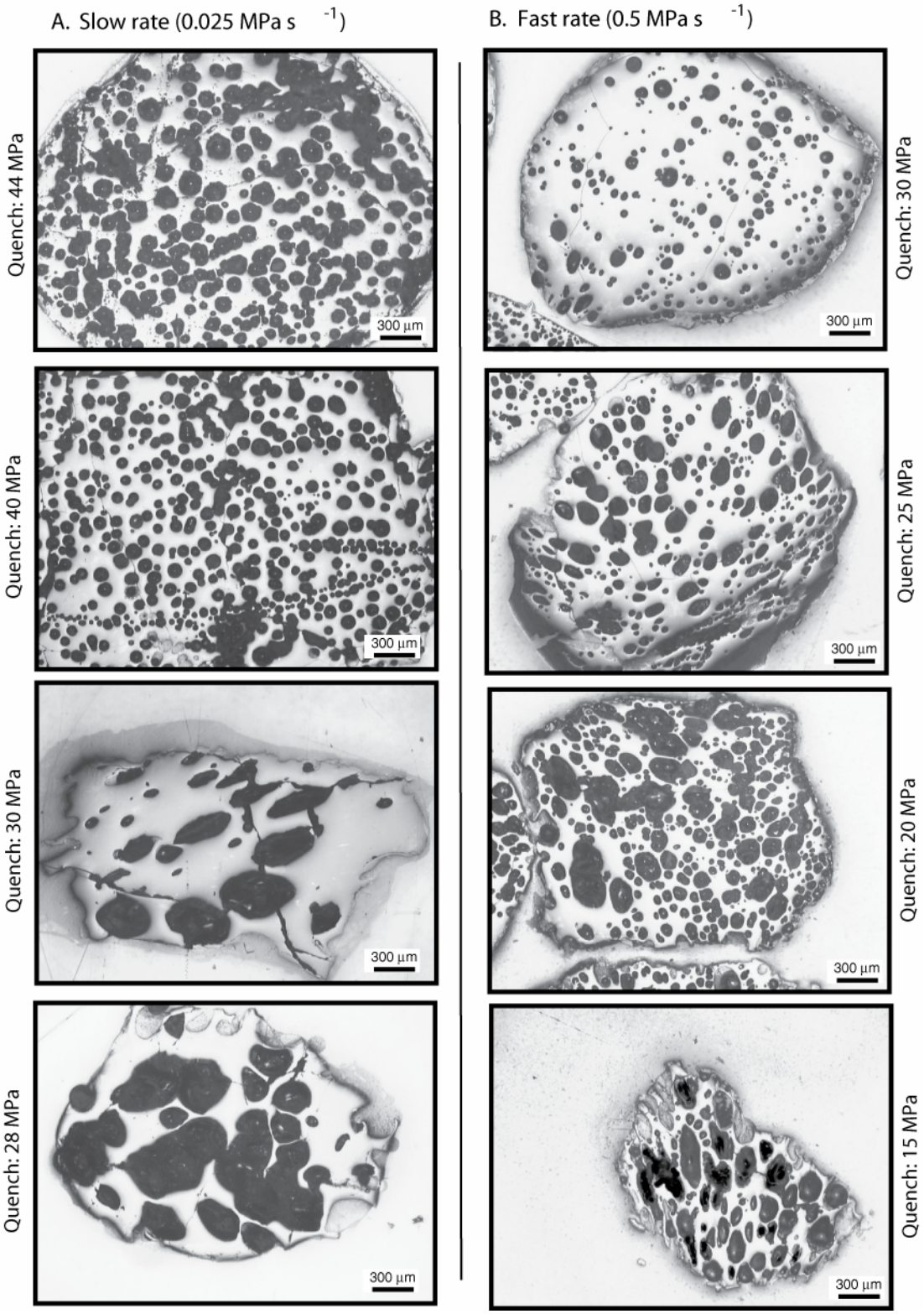

Figure 7 Microphotographs of thin sections in reflected light showing decompression runs with open-degassing conditions. **a.** Linear decompression rate of 0.025 MPa s^{-1}. Bubble coalescence is responsible for the textural change occurring between 40 and 30 MPa. **b.** Linear decompression rate of 0.5 MPa s^{-1}. Note that coalescence occurs progressively because of the faster decompression.

The pressure range over which connectivity becomes complete increases as the decompression rate increases (Fig. 9). At 0.025 MPa s^{-1}, connectivity is complete within an interval of 4 MPa, whereas at 0.5 MPa s^{-1}, connectivity is incomplete after 15 MPa decompression. The completion time for connectivity can be retrieved from the

decompression rates and the pressure range. This time seems to be rate-independent and lies between 160 and 180 s (Fig. 9). Although coalescence is homogeneous within the main body of a given sample, we observe coalescence to begin at higher quench pressure in the top part of the samples, where elongated bubbles occur (Fig. 2). This earlier onset of coalescence of the elongated bubbles occurs regardless of decompression rate.

Similarly sized bubbles seem to coalesce in two phases. During the first phase, neighboring bubbles start to deform during growth, creating a planar film of liquid between them (Fig. 10). The second phase occurs when the thinning film between the bubbles fails. Our smallest measured film thickness is on the order of 1 μm (G303), which suggests that the film disrupts when it reaches a thickness less than 1 μm (Klug and Cashman 1996; Navon and Lyakhovsky 1998). The coalesced bubbles present a deformed shape with low curvature surface. We did not observe the relaxation of coalesced bubbles to spherical shape, most likely because the time needed for such relaxation is on the order of hours at the viscosities considered herein (our calculations follows Toramaru 1995).

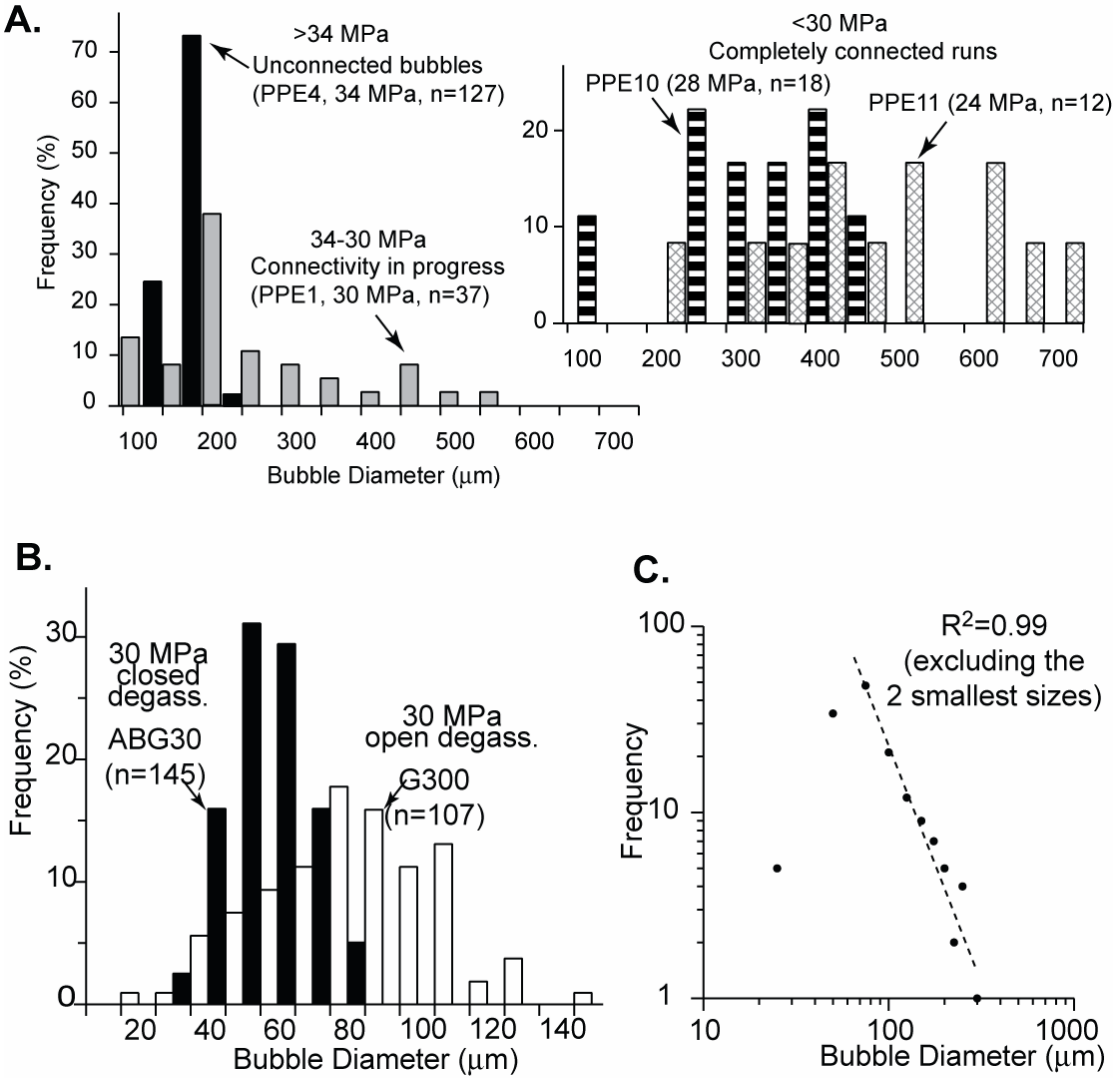

Figure 8 Bubble size distributions (BSD) of open degassing experiments showing the effects of coalescence. **a.** Coalescence from inception (PPE4) to in-progress (PPE1) to completion (PPE10) at low decompression rate (0.025 MPa s^{-1}). Note the few changes induced by further decompression after complete connection (PPE11), and the low bubble count of connected samples due to large bubbles. **b.** Open degassing conditions produce broader distributions (G300, 0.5 MPa s^{-1}, median diameter = 77 μm, σ = 25, BND = 11×10^5 cm^{-3}) than closed degassing conditions (ABG30, 0.5 MPa s^{-1}, median diameter = 60 μm, σ = 11, BND = 35×10^5 cm^{-3}). **c.** Coalescence creates large bubbles and produces a distribution that mostly fits a power-law (G327, 0.5 MPa s^{-1}).

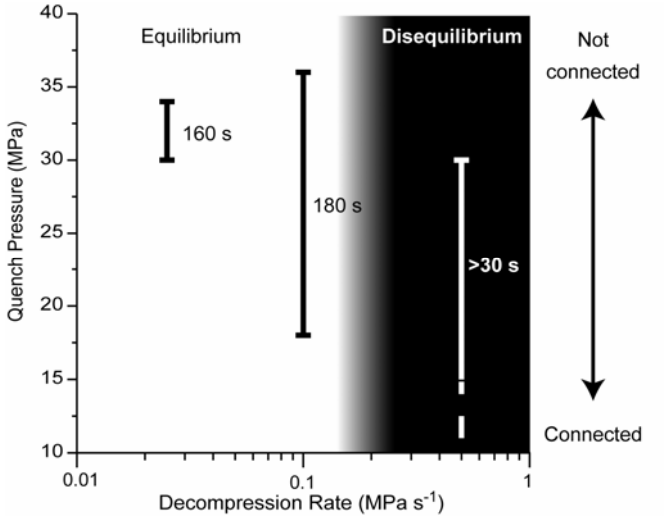

Figure 9 Coalescence start and completion in function of the quench pressure. Also shown are time estimates to complete connectivity for various decompression rates.

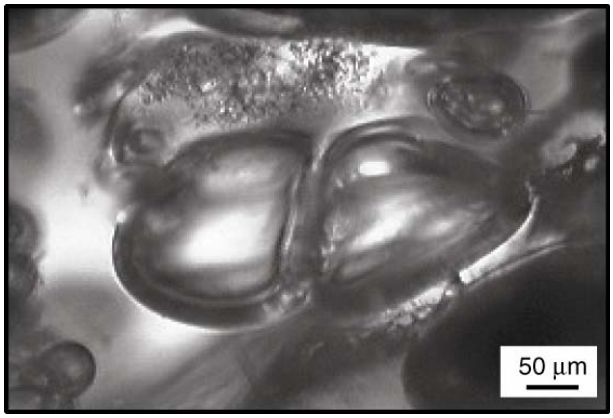

Figure 10 Typical bubble pair shortly before coalescence. Note the planar shape of the thin separation wall between the bubbles (G303, Table 2).

4. Discussion

4.1. Regimes of bubble growth

The complexity of bubble growth in reaction to a sudden pressure drop is well established (e.g., Proussevitch and Sahagian 1998). Growth caused by a constant decompression rate, however, can be approximated from our experiments by two simple disequilibrium regimes (*slow* and *fast* growth rates, Fig. 5). This suggests that one of the main variables (sample volume, melt viscosity, bubble time delay, super-saturation, and porosity) controls the system at a given time. Decompression causes a volumetric expansion of the sample within the gold capsule, which squeezes the melt into the headspace of the capsule (Figs 1 and 2). We attribute the elongated bubbles present in the upper part of the samples to the shear accompanying this extrusion. Because the effect of the shear is confined to a small region of the samples (< 25 vol.%), we conclude that the sample expansion does not influence the average bubble growth. We estimate the melt viscosities in our experiments to range between 5.9×10^4 Pa s at 100 MPa and 1.5×10^6 Pa s at 30 MPa (at 825 °C under water saturation, Hess and Dingwell 1996), which are well below the values that affect bubble growth (~$10^{8\text{-}9}$ Pa s, Gardner et al. 2000). Our data provide an indirect measure of the amount of water super-saturation, because super-saturation increases with the difference ($\Delta\alpha$) between the equilibrium porosity and the sample porosity (Fig. 6). In the slow growth rate regime, super-saturation ($\approx\Delta\alpha$) increases linearly with decreasing pressure regardless of decompression rate (Fig. 5). We note that Gardner et al. (1999) also observed this linearity, and we used it to infer values of $\Delta\alpha$ for the 1 and 10 MPa s^{-1} rates. Above a critical value ($\approx\alpha_{cr}$), however, bubble

growth accelerates and switches from slow to fast growth regime, quickly becoming faster than the equilibrium rate. This behavior is consistent with the well-known relationship between super-saturation and growth: growth is strongly driven by the amount of excess water, because the rate of water diffusion into the bubble increases with the concentration gradient between the melt and the bubble (Sparks 1978; Proussevitch and Sahagian 1998).

Is super-saturation the main process controlling the occurrences of the two disequilibrium regimes? We stress that the critical porosity observed in our experiments is a proxy for the level of super-saturation away from the bubbles because the critical value (α_{cr}) results from the integration of all the processes at play during growth. With this simplification in mind, we note two situations where the far-field super-saturation alone cannot explain our data. First, the fastest decompression rate (10 MPa s^{-1}) has a critical value much larger than the other rates, whereas α_{cr} should not depend on decompression rate (Fig. 6). We note that the time to reach the critical value is only 4 s for the 10 MPa s^{-1} rate and more than 40 s for the other rates. Bubble time delay, which is a very slow initial growth rate due to unfavorable transport properties of the melt next to the bubble walls, may play a role at large decompression rates. Proussevitch and Sahagian (1998) calculated the bubble time delay for a rhyolitic melt instantly decompressed from 100 MPa to be ~2 s. Our fast rate approximates the instantaneous decompression simulated by Proussevitch and Sahagian (1998), which suggests that the bubble time delay affected the 10 MPa s^{-1} run because of its short duration (4 s). Second, super-saturation alone cannot force $\Delta\alpha$ to vanish at high porosities, thus re-equilibrating melt and bubbles. We suggest this re-equilibration occurs because the spaces between bubbles are reduced at high porosities. In other words, the shell defined by the super-saturation gradient around a given bubble starts to interact with its neighbors, thereby canceling the gradients, as illustrated in the model by Proussevitch et al. (1993a). The influence of porosity is therefore confined to the latest stages of the decompression (at low pressure and high porosity), when there is competition between the large decompression rate, which forces disequilibrium degassing, and small bubble spacing, which reduces the length over which water must diffuse.

4.2. Coalescence

We can use our experiments to identify some of the parameters that govern coalescence. Most likely, coalescence is incomplete for the faster decompression rate (Fig. 9) because the time allowed for connection decreases as decompression rate increases whereas the time needed for bubbles to coalesce is finite. Thus, the process of coalescence itself is time dependent (~180 s), whereas the inception of coalescence is porosity dependent (~43 vol.%). We note that the decompression rate does not influence the values of time and porosity, suggesting these two parameters do not depend on the speed of magma ascent (see *Implications for Volcanic Eruptions*). The porosity dependence is consistent with the sharp increase in permeability with porosity noted by Westrich and Eichelberger (1994) on high-silica melts. We note that their permeability increase occurs at a higher porosity (60 vol.%) than the one we observed. This difference is probably caused by the closed degassing conditions Westrich and Eichelberger (1994) used in their experiments. This well-defined beginning of permeability in high temperature silicate melts contrasts with the continuous relationship between permeability and porosity found in cold natural products (Klug and Cashman 1996). This discrepancy suggests inferences carried from measurements made on solid clasts to the properties of hot melt are somewhat limited. Another parameter regulating coalescence is the amount of shear applied to the melt, as suggested by the early coalescence observed in the upper part of the samples. This relationship is not surprising, as the catalyzing role of shear on coalescence is well known (Stasiuk et al. 1996). Considering that the natural system is flowing whereas our experiments are static, we expect the values of the controls of coalescence (porosity and time) to be equal or lower in volcanic conduits than in our experiments because we expect the magma to go under significant shear during ascent in the conduit.

A perhaps more fundamental problem is to identify the cause(s) of coalescence in the open degassing runs. The importance of viscosity and the spatial arrangement of bubbles as controlling factors of coalescence and permeability have been discussed by many authors (e.g., Proussevitch et al. 1993a; Gaonac'h et al. 1996; Blower 2001). Viscosities are expected to be similar for both open and closed degassing samples, but coalescence is manifest only in the open degassing set. Our experiments generate similar BSD and BND at high pressure for both sets (Fig. 8b). Hence, we expect similar nucleation and growth kinetics. The major difference between the two sets seems to be the volatile concentration gradient at the sample free surface that extends on a much larger scale than the average bubble diameter. The effect of this concentration gradient on coalescence will be the object of a further study.

Our observations of coalescence have various implications for the study of bubble size distribution in high-silica melts. We observe that power-law BSD, although limited to one order of magnitude, result from bubble coalescence (Fig. 8c). Previously, two possible mechanisms have been proposed to explain the formation of a power-law BSD: cascading coalescence, where successive coalescence events occur through binary collisions of similarly sized bubbles (Gaonac'h et al. 1996) and continuous bubble nucleation (Blower et al. 2001). While the former is accepted for low-viscosity magmas, the latter has been proposed to explain natural size distributions in high-viscosity systems. In our experiments, all runs in closed degassing conditions display unimodal bubble size distributions below 100 MPa. Since the open degassing runs followed similar decompression paths as the runs in closed degassing conditions, we deduce that bubbles did not continuously nucleate during decompression below 100 MPa. Instead, the concurrence of bubble coalescence (Fig. 10) with the shift from Gaussian to power-law size distributions suggest that cascading coalescence also operates in high-viscosity melts.

Coalescence generates broad bubble size distributions with large bubbles coexisting with bubbles 20 times smaller. To assess whether the widening of the BSD is entirely caused by coalescence, we compare the BSD between closed degassing runs and the equivalent open degassing runs at the inception of coalescence (both produce similar Gaussian shapes, Fig. 8b). The two runs (ABG30 and G300) have a ~17 μm difference in median bubble diameter, which results from differing bubble number densities. To carry out the comparison, we add this difference to each bubble size of the smaller-sized run (ABG30). The BSD of the closed degassing run is narrow, with a standard deviation less than 20%, and no measured bubbles below 35+17=52 μm or above 88+17=105 μm. In contrast, the BSD of the open degassing run has a deviation greater than 30% with bubbles as small as 14 μm, and as large as 147 μm. Whereas the larger bubbles are produced by coalescence, the smaller bubbles could result from either nucleation of new bubbles, Ostawald ripening, or hindered growth. The occurrence of a new nucleation event during decompression is unlikely, because of the unimodality of the closed-run BSD and the low decompression rates applied. Ostwald ripening is the tendency of large bubbles to grow at the expense of smaller neighbors because of the diffusive gas exchange driven by the pressure difference *between the bubbles*. In order to determine whether this process may influence the changes in BSD, we calculated the time scale t for Ostwald ripening to occur after (Proussevitch et al. 1993b):

$$t = \frac{P\delta}{4RTD\sigma x}\left(r_0^2 - r_1^2\right)$$

where r_0 and r_1 are the initial and final bubble radii, R is the gas constant, D is water diffusivity (5.8×10^{-12} m^2 s^{-1}, Zhang et al. 1991), T is temperature (825 °C), P is the quench pressure (30 MPa for G300), σ is the surface tension between bubble and melt (0.06 N m^{-1}, Epel'baum et al. 1973), x is the water solubility in the melt (Equ. A5), and δ is the distance between neighboring bubbles: $\delta=2r_m((0.78/\alpha)^{1/3}-1)$ where α is the sample porosity and r_m the mean bubble radius. The time needed for the smallest bubbles (r_0= 14 μm) in the open degassing run G300 (α=0.35, Table 2) to contract from the mean bubble size (r_1= 77 μm) is 4.5 hour, which is much longer than the decompression duration (140 s). We also note that the

time for the largest bubble (r_0= 147 μm) to ripen from the mean bubble size (r_1= 77 μm) is 12.5 hour. Thus, Ostwald ripening is not likely to affect bubble sizes in any of our experiments because run durations are always less than 50 minutes. Hindered growth is related to the concentration gradient field around each bubble caused by decompression and it occurs when the concentration gradient around *a single bubble* affects the growth of its neighbors. Experimental work showed that in melts containing bubbles with large size difference (ratio 1:4), large bubbles tend to damper the growth of smaller neighboring bubbles, possibly decreasing their sizes (Larsen and Gardner 2000). In our experiments, the size ratio between the small bubbles and their coalesced neighbors is on the order of 1:100. Thus, hindered growth seems the most likely process to control the emergence of small bubbles.

Does the permeability that develops in our experiments represent that of a magmatic liquid? Permeability arises only when enough bubbles connect and form chains (e.g., 40 MPa run, Fig. 7a) that reach a free surface. If the sample size is less than 10 times larger than the bubbles it contains, however, the chains are only a few bubbles long and affect the permeability of the sample (Blower 2001). This undesirable effect does not occur in our experiments because samples are 100 times larger than the bubbles when connectivity starts and ~20 times larger when connectivity is complete. We note, however, that the time required for coalescence might depend of the sample size.

It is likely that high porosities were achieved even at low decompression rates (e.g., 85 vol.% for PPE11, Table 2), because the amount of gas that could escape was finite, given the finite volume of the capsule headspace and the limited capacity of absorption of the anhydrous powder. This suggests that the melt created an open network of bubbles while coalescing (e.g., 30 MPa run in Fig. 8a), but quickly came back to an impermeable foam (e.g., 24 MPa run in Fig. 8a). As a result, after bubbles collapse to distorted shapes when they release a fraction of their gas, the melt is ready for a second coalescence event. If our experiments can be believed to represent a larger batch of magma, we can transpose this reasoning to the size of a volcanic conduit. In this light, the magma can release only a fraction of its gas during a coalescence event because the conduit also has a limited permeability (e.g., Jaupart and Allegre 1991). Further decompression can thus increase the remaining porosity enough to trigger another coalescence event. Thus, the magma might be affected by several coalescence events before reaching the surface. Since each of these events profoundly modifies the bubble size distribution, variable amount of coalescence would reshape the size distribution of the eruptive products. In other words, coalescence restricts our ability of using eruptive products to discern other degassing processes. We note that shear, fragmentation, and post-fragmentation processes may also change the bubble size distribution, adding difficulty to interpreting BSD of natural samples.

5. Implications for volcanic eruptions

5.1. Modeling magma degassing

Water exsolution into bubbles drives bubble growth, and whether exsolution occurs in equilibrium influences conduit flow dynamics. Although one study explored the consequence of disequilibrium degassing on bubble overpressure (Melnik 2000), no quantitative assessment of the dynamic effects of disequilibrium has been performed. Qualitatively, in disequilibrium the density decrease and viscosity increase caused by bubble growth are diminished, which reduce the decompression rate and flow acceleration. Our experimental results for closed degassing relate decompression rates and degassing style. We have thus used a one-dimensional model of magma ascent before fragmentation to explore further the consequences of disequilibrium degassing.

Our model of magma ascent is based on the model *Conflow* developed by Mastin and Ghiorso (2000), and details of the implementation are given in the *Appendix*. The model assumes steady, isothermal, and homogeneous flow in a vertical cylindrical conduit (e.g., Wilson

1980; Dobran 1992; Papale and Dobran 1993; Woods 1995). Following Mastin and Ghiorso (2000), we solve the momentum equation along the conduit as magma rises, allowing viscosity to vary. We introduce new empirical relations between pressure, decompression, and porosity for each regime of bubble growth (Equs. A10 and A13; Fig. 6), thus allowing disequilibrium degassing. We tested the robustness of our numerical scheme by forcing equilibrium degassing at all times, which produced outputs undistinguishable from the ones of *Conflow*.

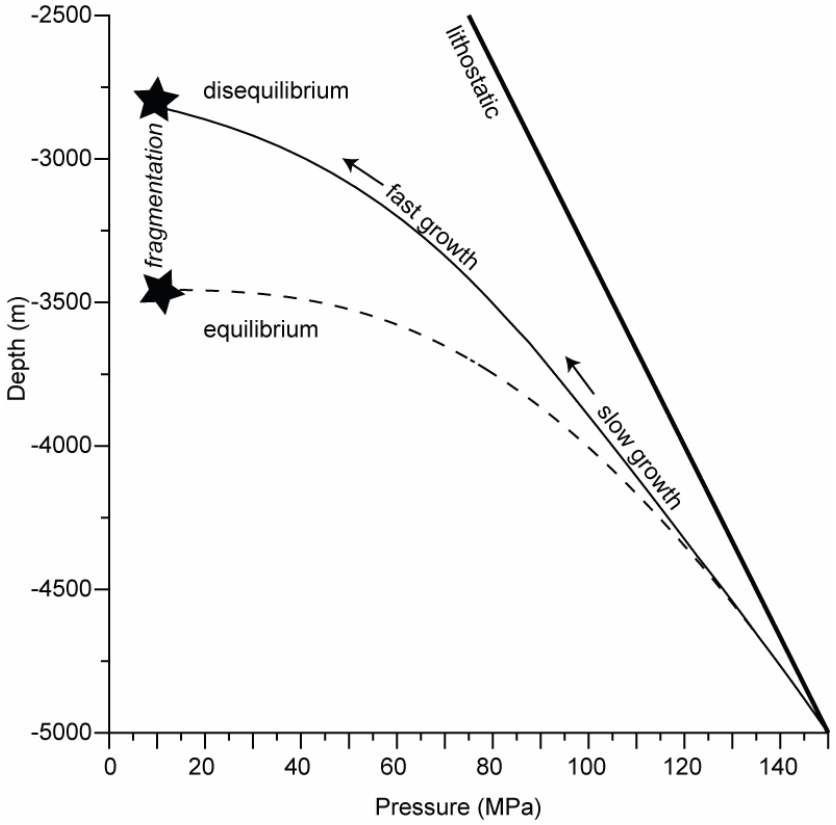

Figure 11 Comparison of pressure-depth variations of 1D conduit flow simulations with and without equilibrium degassing. The solid line represents equilibrium degassing, the stippled line is disequilibrium degassing, the thick line is the lithostatic pressure gradient, and stars are the loci of fragmentation for each run. As the magma rises in steady state (i.e., with a fixed mass flux) along the volcanic conduit, its porosity increases, and the run is stopped when the magma reaches fragmentation at a fixed porosity of 64 vol.%. In the equilibrium run, the combined effect of decreasing porosity and increasing viscosity as the magma rises causes an important deviation from lithostatic pressure. Disequilibrium degassing greatly reduces this deviation and, as a result, fragmentation occurs 1 km higher in the conduit. Zones where particular regimes of bubble growth (slow and fast) occur are also mentioned on the disequilibrium curve. Initial conditions are the same for both runs: P_0 = 150 MPa, ρ_l = 2154 kg m^{-3}, T = 825 °C, $Q = 2.19\times10^6$ kg s^{-1}, R = 10 m.

5.2. Effects of disequilibrium degassing

The comparison between a run of the model with forced equilibrium degassing and with disequilibrium degassing according to our empirical relations is shown in Fig. 11. Initial conditions for both runs are the same as in the experimental sets (825 °C, 150 MPa, water-saturated, 2154 kg m^{-3} from Mastin and Ghiorso 2000). A representative mass flux (2.19×10^6 kg s^{-1} for 20-m diameter conduit) was determined by running *Conflow* (Mastin and Ghiorso 2000) with a boundary condition at atmospheric pressure at the vent because, unlike our model, *Conflow* simulates flow conditions after fragmentation. In the equilibrium degassing run, we note strong accelerations at high porosities (e.g., 4.7 m s^{-2} at 60 vol.%; 30 m s^{-2} at 70 vol.%) and associated large decompression rates (e.g., 15.4 MPa s^{-1} at 60 vol.%; 47.6 MPa s^{-1} at 70 vol.%). These decompression rates force the magma to degas, increasing both porosity

and viscosity, which in turn drives the pressure to drop further, causing the familiar deviation from lithostatic pressure found in similar works (Dobran 1992; Papale 1999; Mastin and Ghiorso 2000). As expected, disequilibrium degassing produces only modest accelerations at high porosities (e.g., 0.97 m s^{-2} at 60 vol.%; 5.4 m s^{-2} at 70 vol.%) and greatly reduces decompression rates (e.g., 3.1 MPa s^{-1} at 60 vol.%; 6.8 MPa s^{-1} at 70 vol.%), thus reducing the deviations from lithostatic pressure. The effect of disequilibrium degassing is best seen at porosities above 60 vol.%, and these reductions of flow acceleration and decompression rate are more important if the values are compared at a given pressure instead of a given porosity.

Disequilibrium degassing causes flow conditions near fragmentation to be not as extreme as previously thought (Dobran 1992; Sparks et al. 1994), and we need to assess whether fragmentation criterions defined by flow conditions occur at a different porosity. First, in the case of sudden decompression of highly viscous magma (e.g., dome failure), fragmentation has experimentally been determined to require a pressure drop on order of 10^2-10^4 MPa s^{-1} with a magma viscosity between 10^8 and 10^{10} Pa s (Alidibirov and Dingwell 2000). We predict both decompression rates and viscosities one to two orders of magnitude below the required values, confirming the inapplicability of this fragmentation criterion in the case of a conduit-driven eruption. Overpressure in bubbles has also been proposed to cause fragmentation (e.g., Navon and Lyakhovsky 1998; Zhang 1999). We calculated (equation 6 in Melnik 2000) with the initial conditions used in Fig. 11 that an overpressure of 10 bar is reached at 87 vol.% porosity in the equilibrium degassing case, and at 83 vol.% in the disequilibrium case. Fragmentation can also occur when the strain rate applied to the magma exceeds its capacity to dissipate the stress by viscous deformation (e.g., Papale 1999). Using the elastic modulus given by Papale (1999), we calculated with the initial conditions used in Fig. 11 that magma viscous dissipation is overcome at 80 vol.% porosity in both equilibrium and disequilibrium cases. Thus, despite significant changes in flow conditions at high porosity, the porosity at which fragmentation occurs is insensitive to the degassing style.

The depth of fragmentation, however, is significantly shallower with disequilibrium degassing, regardless of the fragmentation criterion (e.g., 1 km higher in Fig. 11, fragmentation defined by a fixed value of porosity, 64 vol.%, Gardner et al. 1996). We also note that an estimate of the effect of delayed nucleation (or melt super-saturation, Woods 1995) had a similar effect. Fragmentation depth is thus highly sensitive to the rate at which the different processes that control degassing occur in the conduit.

The robustness of our empirical approach of disequilibrium degassing can be assessed by comparing the effects produced by two independent sets of internally consistent data. For example, the decompression experiments of Gardner et al. (1999) were run under similar conditions as our closed degassing experiments. High-silica rhyolite with low crystal content (< 1 vol.%) was heated at the same temperature (825 °C) and linearly decompressed at various rates. The higher initial confinement pressure (200 MPa) allows a qualitative extension of our model to a broader range of initial conditions. Keeping in mind that the Gardner et al. (1999) decompressions start from initial, water-saturated pressure, and therefore that these runs include nucleation kinetics, we can extend the empirical formulation of the slow growth rate regime (Equ. A10). A regression including both experimental sets gives a coefficient (A_z) 20 % higher than the one determined from 150 MPa, and slightly increases the correlation coefficient (Table 3). The regression of both sets on the boundary between the slow and fast growth regimes (Equ. A14) changes the coefficients (a_1 and b_1) by less than 1 %, and slightly lowers the correlation coefficient (Table 3). The extension of the comparison to the fast growth regime is not possible due to the lack of data towards lower pressures for runs initiated at 200 MPa. Runs of the disequilibrium model with identical initial conditions, but with the coefficients determined from both data sets, are indistinguishable on the scale of Fig. 11. Thus, our empirical approach shows little sensitivity to initial confining pressure, nucleation kinetics at low crystal volume fraction, and small differences in melt composition.

Table 3: Empirical constants used to assess disequilibrium degassing

	A_z	R^2	a_1	b_1	R^2	a_2	b_2	R^2
this study	-5.3×10^{-6}	0.73	0.256	1.567	0.95	2.36×10^{-11}	6.46×10^{-10}	0.99
this study & Gardner et al. (2000)	-6.8×10^{-6}	0.98	0.258	1.549	0.75	n.a.	n.a.	n.a.

5.3. Effects of connectivity

In a volcanic conduit, the creation of an open network would allow gas to escape from the magma. The ensuing diminution of porosity would reduce flow acceleration and possibly lead to effusive eruption (Eichelberger et al. 1986; Jaupart and Allegre 1991). On the other hand, the high porosities needed for fragmentation may only be reached if bubble connection is incomplete. Thus, it seems that fast decompression rates are required for explosive eruption (see sections *Open degassing runs* and *Connectivity*). We therefore used the conjunction of our model and the experimental results on connectivity to assess the transition between effusive and explosive regimes.

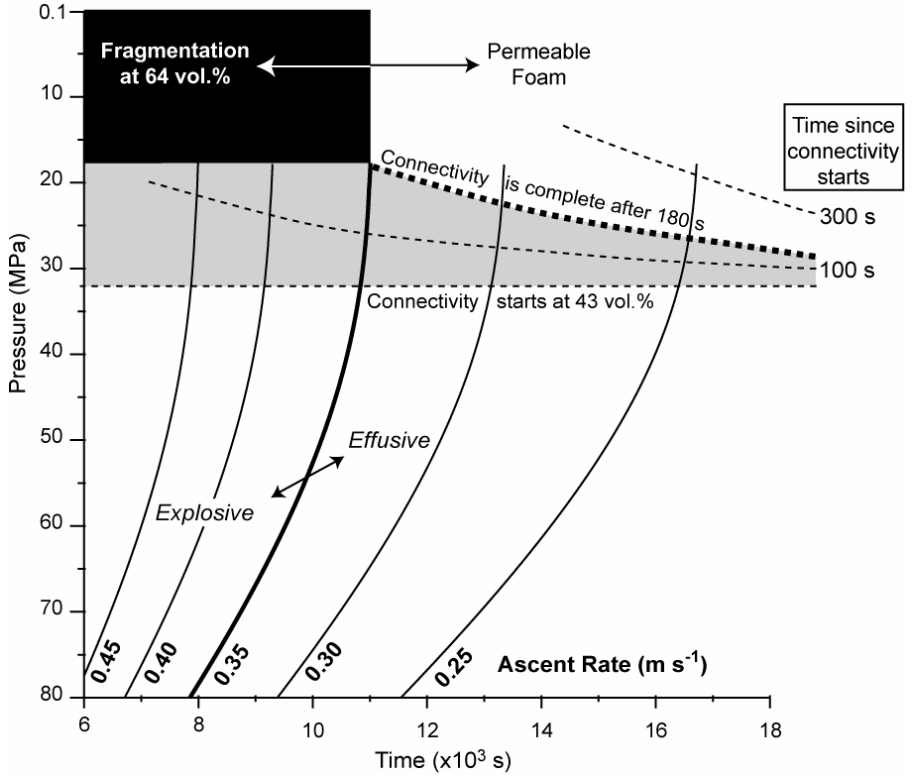

Figure 12 The effect of magma initial ascent rate on the transition between effusive and explosive eruption. Values of the x-axis correspond to the time since the beginning of magma ascent, whereas the y-axis is the magma pressure. Labels next to each curve give the initial ascent rate of the magma, so that each curve gives the pressure of a batch of magma as a function of elapsed time since its release from depth at that initial ascent rate. Bubble connectivity occurs at 43 vol.% porosity (32 MPa in equilibrium degassing) and is complete after 180 s. Completion of connectivity before 64 vol.% porosity allows the gas to escape from the magma and leads to an effusive eruption, whereas incomplete connectivity at 64 vol.% porosity leads to magma fragmentation because gas remains in the melt. Note that a small change in the initial ascent rate (i.e. mass flux because of the steady state condition) controls the effusive/explosive transition. Initial conditions for all curves are: P_0 = 150 MPa, ρ_l = 2154 kg m^{-3}, T = 825 °C, and R = 10 m.

We performed numerical runs varying only the initial ascent speed of magma (Fig. 12), and superimposed the results of the connectivity experiments. From the open degassing experiments, we consider that connectivity is rate-independent, begins at 32 MPa (43 vol.% porosity in equilibrium), and is complete after 180 s. We set the fragmentation porosity to 64 vol.% to begin with, because it matches the vesicularity of most pumice (Gardner et al. 1996). Thus, if the magma reaches 64 vol.% porosity more than 180 s after reaching 43 vol.%, then it erupts effusively.

We find that the critical ascent rate is modest, 0.35 m s^{-1}, which corresponds to a mass flux of 2.4×10^5 kg s^{-1} for a 20-m diameter conduit (2154 kg m^{-3}, water-saturated magma at 825 °C and 150 MPa), and that only runs below 0.30 m s^{-1} occur completely in the equilibrium-degassing regime. At those conditions, a variation of 0.1 m s^{-1} reduces or expands the time allowed for complete connection by about one minute, with a roughly linear dependence between initial ascent rate and connectivity completion. Although we set the fragmentation porosity to 64 vol.%, raising it to the values suggested by the strain-rate criterion, the bubble overpressure criterion, or commonly used values (67-80 vol.%: Sparks 1978; 75 vol.%: Mastin and Ghiorso 2000) would only increase slightly the initial magma ascent rate, but not change this linear dependence. Thus, the dependence between ascent rate and connectivity suggests that the transition from effusive to explosive regime is very sensitive to initial ascent rate, regardless of the exact formulation of fragmentation.

Because our model does not allow the gas to escape from the magma, the numerical runs are minimum estimates of ascent speeds for open degassing systems. The effect of connectivity, however, can be assessed with an open-system conduit flow where the gas can flow within bubble chains (Yoshida and Koyaguchi 1999). After adjusting the parameters of the model (Equ. 37 in Yoshida and Koyaguchi 1999) to match our values of porosity and pressure at the onset of connectivity, the pressure reached at fragmentation porosity (64 vol.%) if the gas escapes from the bubbles is 6 MPa instead of 17 MPa. The magma takes about 100 s more to reach this former pressure. The linear relationship between ascent rate and connectivity indicates that our closed-degassing model underestimates the critical ascent rate by 0.2 m s^{-1} (+57%). Therefore, the value of the critical ascent rate highly depends on the exact influence of permeability on flow dynamics. This limitation, however, does not affect our conclusions regarding the sensitivity to initial conditions displayed by the transition between explosive and effusive regimes.

Superimposing the results of the open degassing experiments to our model leads to two additional conclusions. First, the assumption of closed-system for conduit model can be applied at large magma ascent speeds and high mass fluxes (e.g., Plinian eruptions), but should be restricted to high pressures (> 32 MPa) and low gas volume fractions (< 43 vol.%) at low ascent speeds (e.g., lava dome). Second, our estimate of ~43 vol.% porosity for the onset of connectivity is a maximum, because the shear present in the conduit enhances the efficiency of coalescence, which increases the time for gas to escape. The time scale of 180 s given for connectivity is thus a maximum, and hence flow conditions near fragmentation may significantly be affected by connectivity and gas escape.

6. Conclusions

Decompression experiments performed on rhyolitic melt hydrated at 150 MPa and sub-liquidus temperature lead us to define three distinct bubble growth regimes. An *equilibrium growth regime* occurs when the melt initially decompresses slow enough (< 0.1 MPa s^{-1}) to allow water to completely diffuse from melt to bubbles. The *slow growth rate regime* occurs when the melt decompresses faster than equilibrium (> 0.2 MPa s^{-1}). In this regime, porosity evolves linearly with pressure, regardless of decompression rate. A *fast growth rate regime* occurs when the super-saturation reaches a critical value, which depends on decompression rate, and accelerates bubble growth. The fast growth diminishes the porosity deviation from equilibrium linearly with pressure decrease.

We assessed the consequences of the three growth regimes on conduit flow dynamics by a one-dimensional model of magma ascent fitted by the experimental data. Compared to previous models that assume equilibrium degassing of the melt during ascent, the introduction of disequilibrium degassing reduces the deviation from lithostatic pressure by ~ 25 %, the acceleration at high porosities (> 50 vol.%) by a factor 5, and the associated decompression rate by an order of magnitude. Importantly, flow conditions near fragmentation are not as extreme as previously thought. Comparison with other published decompression experiments (Gardner et al. 1999) shows that our empirical approach is valid for rhyolitic (10^4 – 10^7 Pa s) melts with low crystal contents (< 1 vol.%) stored in the upper crust (< 200 MPa).

Experiments run under open degassing conditions show that bubbles start to coalesce around 43 vol.% porosity. The fact that this value is independent of decompression rate suggests that coalescence might happen at *all* eruptive regimes. The process of coalescence, however, is time-dependent and occurs in a matter of minutes (~ 180 s). Thus, coalescence may not reach completion in the more violent (Plinian) eruptive regimes. Coalescence generates broad bubble size distributions with large bubbles coexisting with bubbles 20 times smaller. Thus, the occurrence of coalescence in a volcanic conduit profoundly reshapes the bubble size distribution, possibly restricting our ability of using eruptive products to differentiate various degassing processes. Introduction of these results into our conduit flow model shows that the transition between explosive and effusive regime is sensitive to small variations of initial magma ascent speed (on the order of 0.01 m s^{-1} for a conduit 20 m in diameter). The assumption of closed-system for conduit flow models must be restricted to porosities lower that 43 vol.%, but can be extended to higher porosities in the case of high mass fluxes. Flow conditions near fragmentation, however, may significantly be affected by coalescence and gas escape.

Acknowledgments

We would like to thank P.J. Shamberger for helping us running the coalescence experiments, while he was a REU intern at the Geophysical Institute and M. Wahlen for letting us use his digital microphotography equipment. Discussions with L. Mastin helped to clarify many mysteries of conduit flow modeling. Thorough reviews by M. Mangan and D. Sahagian greatly improved the manuscript. Funding was provided by the NSF grant EAR-0087853 to J.E.G. and by the Volcano Hazards Program of the US Geological Survey, through the Alaska Volcano Observatory to A.B.

Appendix

Our simple model of magma ascent trough a conduit before fragmentation is based on the approach first developed by Wilson (1980). We closely follow Mastin and Ghiorso (2000)'s solution, so that when the decompression rates are small enough to allow degassing to occur in equilibrium, the output of our model is undistinguishable from the one of Mastin and Ghiorso (2000). The novelty we introduce is the effect of disequilibrium degassing, for which we develop empirical relations between pressure, decompression rate, and porosity for the regimes of bubble growth, and their respective range of applicability (Equs. A10-A15). The model is one-dimensional and thus flow properties are averaged across the (constant) cross-sectional area of the conduit at any given depth. The flow is considered isothermal and homogeneous (i.e., bubbles rise at the same speed as the magma), the conduit is a vertical cylinder with impermeable rigid walls, and the gas phase is H_2O. Although those assumptions are not strictly applicable to the natural system, they have been widely used to provide a reasonable approximation of magma velocities in a conduit during an eruption. We consider that the mass flux Q remains constant, so that:

$$Q = \rho \pi r^2 v \qquad \text{(A1)}$$

where ρ is the mixture density, v its speed, and r the conduit radius. The flow below fragmentation is laminar, thus the steady-state conservation of mass and momentum read (e.g., Woods 1995):

$$\frac{d(\rho v)}{dz} = 0 \tag{A2}$$

$$\rho v \frac{dv}{dz} = -\frac{dP}{dz} - \rho g - f \tag{A3}$$

where P is the magma pressure, g is the acceleration of gravity (9.81 m s^{-2}), z is the height within the conduit, and f a friction factor given by (Mastin and Ghiorso 2000):

$$f = \frac{8\mu v}{r^2} + 0.0025\frac{\rho v^2}{r} \tag{A4}$$

where μ is the magma viscosity. The presence of bubbles in the magma causes viscosity to change as a function of gas fraction and shear (e.g., Pal 2003), but these complex changes cannot be fully evaluated a model that uses depth-averaged quantities. Thus, following Mastin and Ghiorso (2000), we use the pure melt viscosity in Equ. A4 (Hess and Dingwell 1996). When bubbles are in equilibrium with the liquid, the solubility law gives the weight fraction x of water remaining in the liquid (e.g., Woods 1995):

$$x = \kappa\sqrt{P} \tag{A5}$$

with Henry's constant $\kappa = 3.44\times10^{-6}$ $kg^{0.5}$ $m^{0.5}$ s^{-1} determined from the best-fit parameters of the second-order polynomial regression of our experimental set in equilibrium (Table 1). The difference with the value determined by Mangan and Sisson (2000) for the same PCD rhyolite (4.15×10^{-6}) is mainly due to the form of the regression equation they used (non-zero intercept second order polynomial regression). The mixture density ρ is calculated using the perfect gas law:

$$\rho = \alpha\rho_g + (1-\alpha)\rho_l = \alpha\frac{M}{RT}P + (1-\alpha)\rho_l \tag{A6}$$

Where ρ_l is the liquid density, ρ_g is the gas density, α its volume fraction, M is the water molecular weight (18×10^{-3} kg mol^{-1}), T is the mixture temperature, and R is the universal gas constant (8.3144 J $mole^{-1}$ $°K^{-1}$). Combining the derivative of Equ. A6 with Equs. A1-A3 leads to:

$$\frac{dP}{dz} = \left[\frac{d\alpha}{dz}v^2\left(\frac{MP}{RT} - \rho_l\right) - \rho g - f\right]\left[1 - \alpha\frac{v^2 M}{RT}\right]^{-1} \tag{A7}$$

The evolution of pressure in the conduit is thus controlled by the degassing rate $d\alpha/dz$, which has to be determined for each experimentally determined regime: equilibrium, slow growth, and fast growth. In the equilibrium regime, the gas volume fraction α_{equ} (Fig. 6) is calculated from the difference between the maximum amount of water that can be dissolved in the magma at a given pressure P and the original water content at the initial pressure P_0:

$$\alpha_{equ} = \frac{\beta}{MP + \beta} \qquad \text{with} \qquad \beta = RT\rho_l\kappa\left(\sqrt{P_0} - \sqrt{P}\right) \tag{A8}$$

The derivative of Equ. A8 gives the equilibrium-degassing rate:

$$\left(\frac{d\alpha}{dz}\right)_{equ} = \frac{dP}{dz}M\left(-\beta - \frac{\sqrt{P}}{2}\right)(MP + \beta)^{-2} \tag{A9}$$

The slow growth regime is a linear function of α and P (Fig. 5; see Table 3 for empirical constant value):

$$\left(\frac{d\alpha}{dz}\right)_{slow} = A_z \frac{dP}{dz} \tag{A10}$$

In the fast growth regime, $\Delta\alpha$ is given by the linear regression for each decompression rate (Fig. 5):

$$\frac{d(\Delta\alpha)}{dz} = A_s \frac{dP}{dz} \tag{A11}$$

where A_s varies in function of the decompression rate according to:

$$A_s = a_2 \frac{dP}{dt} + b_2 \tag{A12}$$

Hence the derivative of α with depth becomes:

$$\left(\frac{d\alpha}{dz}\right)_{fast} = \left(\frac{d\alpha}{dz}\right)_{equ} - A_s \frac{dP}{dz} \tag{A13}$$

Note the differential form of Equ. A10 allows a melt to reach atmospheric pressure super-saturated. We also need to determine the boundaries between each regime of degassing. Experimental data (Fig. 3) show that the critical decompression rate between the equilibrium and the slow growth regimes varies little between high and low pressure, so we used a unique median value of 0.15 MPa s^{-1}. The boundary between the slow growth and the fast growth regimes is reached when the difference between the disequilibrium (α) and the equilibrium (α_{equ}) porosities $\Delta\alpha$ is greater than a critical value $\Delta\alpha_{cr}$ (Fig. 6). The relation between $\Delta\alpha_{cr}$ and the decompression rate is given by the regression:

$$\ln(\Delta\alpha_{cr}) = a_1 \ln\left(\frac{dP}{dt}\right) + b_1 \tag{A14}$$

Experimental data were used for the regression when available and interpolated between the slow and fast growth curves when no data point fell on $\Delta\alpha_{cr}$ (Figs. 5 and A1). The nonlinear form of Equ. A14 has been preferred over a linear form to ensure a realistic (asymptotic) behavior of the critical porosity at large decompression rates. In disequilibrium degassing, the melt viscosity is calculated from the water content at P_{right} (Equ. A5, Fig. 6), because the amount of water in bubbles at a given pressure corresponds to the equivalent equilibrium value α_{right}. P_{right} is obtained using Equ. A8:

$$MP_{right}\alpha_{right} + TR\kappa\rho_l\left(\alpha_{right} + 1\right)\left(\sqrt{P_{right}} - \sqrt{P_0}\right) = 0 \tag{A15}$$

The degassing behavior of Equ. A7 is thus given by $(d\alpha/dz)_{equ}$ (Equ. A9) if dP/dt<0.15 MPa s^{-1}; $(d\alpha/dz)_{slow}$ (Equ. A10) if dP/dt>0.15 MPa s^{-1} and $\alpha > \alpha_{cr}$; and $(d\alpha/dz)_{fast}$ (Equ. A13) if dP/dt>0.15 MPa s^{-1} and $\alpha > \alpha_{cr}$ with the porosity α being calculated from the previous distance step. Equ. A7 is solved using a fourth-order Runge-Kutta algorithm with a constant distance step of 0.5 m below 50 vol.% porosity and 0.05 m above.

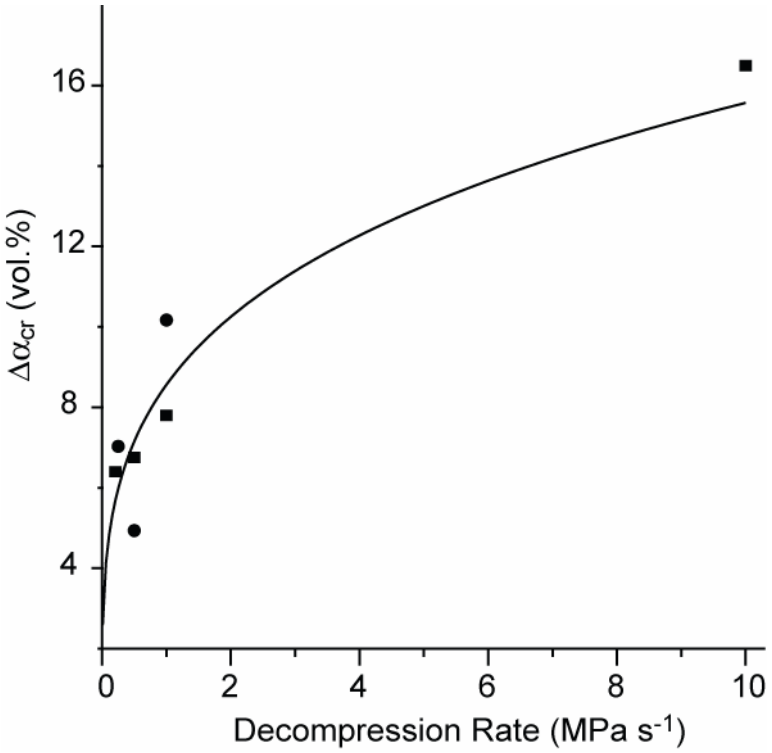

Figure A1 Nonlinear regression of $\Delta\alpha_{cr}$ (maximum porosity deviation from equilibrium degassing) in function of the decompression rate. Circles are data from Gardner et al. (1999) and squares are data from this study.

References

Alidibirov M, Dingwell, DB (2000) Three fragmentation mechanisms for highly viscous magma under rapid decompression, J Volcanol Geotherm Res 100:413-421

Barclay J, Riley DS, Sparks RSJ (1995) Analytical models for bubbles growth during decompression of high viscosity magmas, Bull Volcanol 57:422-431

Blower JD (2001) Factors controlling permeability-porosity relationships in magma, Bull Volcanol 63:497-504

Blower JD, Keating JP, Mader HM, Phillips JC (2001) Inferring volcanic degassing processes from vesicle size distributions, Geophys Res Let 28:347-350

Dobran F (1992) Nonequilibrium flow in volcanic conduits and application to the eruptions of Mt. St. Helens on May, 18, 1980, and Vesuvius in AD 79, J Volcanol Geotherm Res 49:285-311

Eichelberger JC, Carrigan CR, Westrich HR, Price RH (1986) Non-explosive silicic volcanism, Nature 323:598-602

Epel'baum MB, Babashov IV, Salova TP (1973) Surface tension of felsic melt at high temperature and pressures, Geokhimiya 3:461-464.

Gaonac'h H, Lovejoy S, Stix S, Scherzter D (1996) A scaling growth model for bubbles in basaltic lava flows, Earth Planet Sci Lett: 139:395-409

Gardner JE, Thomas RME, Jaupart C, Tait S (1996) Fragmentation of magma during Plinian volcanic eruptions, Bull Volcanol 58:144-162

Gardner JE, Hilton M, Carroll MR (1999) Experimental constraints on degassing of magmas: isothermal bubble growth during continuous decompression from high pressure, Earth Planet Sci Lett 168:201-218

Gardner JE, Hilton M, Carroll MR (2000) Bubble growth in highly viscous silicate melts during continuous decompression from high pressure, Geochim Cosmochim Acta 64:1473-1483

Hess K-U, Dingwell DB (1996) Viscosities of hydrous leucogranitic melts: A non-Arrhenian model, Am Mineralogist 81:1297-1300

Hurwitz S, Navon O (1994) Bubble nucleation in rhyolitic melts: Experiments at high pressure, temperature, and water content, Earth Planet Sci Lett 122:267-280

Jaupart C, Allegre C (1991) Gas content, eruption rate and instabilities of eruption regime in silicic volcanoes, Earth Planet Sci Lett 102:413-429

Klug C, Cashman KV (1996) Permeability development in vesiculating magmas: implications for fragmentation, Bull Volcanol 58:87-100

Larsen JF, Gardner JE (2000) Bubble-bubble interactions in rhyolitic melts: applications to the evolution of bubble size distributions, Earth Planet Sci Lett 180:201-214
Lyakhovsky V, Hurwitz S, Navon O (1996) Bubble growth in rhyolitic melts: experimental and numerical investigation, Bull Volcanol 58:19-32
Mangan M, Sisson T (2000) Delayed, disequilibrium degassing in rhyolite magma: decompression experiments and implications for explosive volcanism, Earth Planet Sci Lett 183:441-455
Mastin LG, Ghiorso MS (2000) A numerical program for steady-state flow of magma-gas mixtures through vertical eruptive conduits, Open-File Report of the USGS, pp 1-53
Melnik OE (2000) Dynamics of two-phase conduit flow of high-viscosity gas-saturated magma: large variations of sustained explosive eruption intensity, Bull Volcanol 62:153-170
Navon O, Lyakhovsky V (1998) Vesiculation processes in silicic magmas, in: Gilbert JS, Sparks RSJ (eds), The physics of explosive volcanic eruptions, Geol Soc Spec Pub, London, 145:27-50
Pal R (2003) Rheological behavior of bubble-bearing magmas, Earth Planet Sci Lett 207:165-179
Papale P, Dobran F (1993) Modeling of the ascent of magma during the Plinian eruption of Vesuvius in AD79, J Volcanol Geotherm Res 55:101-132
Papale P (1999) Strain-induced magma fragmentation in explosive eruptions, Nature 397:425-428
Proussevitch AA, Sahagian DL (1998) Dynamics and energetics of bubble growth in magmas: Analytical formulation and numerical modeling, J Geophys Res 103:18223-18251
Proussevitch AA, Sahagian DL, Anderson AT (1993a) Dynamics of diffusive bubble growth in magmas: Isothermal case, J Geophys Res 98:22283-22307
Proussevitch AA, Sahagian DL, Kutolin AT (1993b) Stability of foams in silicate melts, J Volcanol Geotherm Res 59:161 178
Sparks RSJ (1978) The dynamics of bubble formation and growth in magmas: a review and analysis, J Volcanol Geotherm Res 3:1-37
Sparks RSJ, Barclay J, Jaupart C, Mader HM, Phillips JC (1994) Physical aspects of magma degassing I. Experimental and theoretical constraints on vesiculation, *in*: Carroll MR, Holloway JR (eds) Volatiles in magmas, Rev Mineralogy 30:413-445
Stasiuk MV, Barclay J, Carroll MR, Jaupart C, Ratte JC, Sparks RSJ, Tait SR (1996) Degassing during magma ascent in the Mule Creek vent (USA), Bull Volcanol 58:117-130
Toramaru A (1989) Vesiculation process and bubble size distributions in ascending magmas with constant velocities, J Geophys Res 94:17523-17542
Toramaru A (1995) Numerical study of nucleation and growth of bubbles in viscous magmas, J Geophys Res 100:1913-1931
Westrich HR, Eichelberger JC (1994) Gas transport and bubble collapse in rhyolitic magma: an experimental approach, Bull Volcanol 56:447-458
Wilson L (1980) Relationships between pressure, volatile content and ejecta velocity in three types of volcanic explosion, J Volcanol Geotherm Res 8:297-313
Woods AW (1995) The dynamics of explosive volcanic eruptions, Rev Geophysics 33:495-530
Yoshida S, Koyaguchi T (1999) A new regime of volcanic eruption due to the relative motion between liquid and gas, J Volcanol Geotherm Res 89:303-315
Zhang Y, Stopler E, Wasserburg G (1991) Diffusion of water in rhyolitic glasses, Geochim. Cosmochim. Acta 55:441-456.
Zhang Y (1999) A criterion for the fragmentation of bubbly magma based on brittle failure

Physical volcanology of the 2050 BP caldera-forming eruption of Okmok Volcano, Alaska

ALAIN BURGISSER
Alaska Volcano Observatory
Geophysical Institute
University of Alaska Fairbanks

Publié dans: Bulletin of Volcanology (2005) v. 67, p. 497-525.

Abstract

In the Aleutian volcanic chain (USA), the 2050 ± 50 BP collapse of Okmok caldera generated pyroclasts that spread over 1000 km^2 on Umnak Island. After expelling up to 0.25 km^3 DRE of rhyodacitic Plinian air fall and 0.35 km^3 DRE of andesitic phreatomagmatic tephra, the caldera collapsed and produced the 29 km^3 DRE Okmok II scoria deposit, which is composed of valley-ponding, poorly sorted, massive facies and over-bank, stratified facies with planar and cross bedding. Geological and sedimentological data suggest that a single density current produced the Okmok II deposits by segregating into a highly concentrated base and an overriding dilute cloud. The dense base deposited massive facies, whereas the dilute cloud sedimented preferentially on hills as stratified deposits. The pyroclastic current spread around Okmok in an axisymmetric fashion, encountering topographic barriers on the southwest, and reaching Unalaska Island across an 8-km strait on the east, and reaching the shoreline of Umnak in the other directions. A kinematic model (Burgisser and Bergantz, 2002, Earth Planet. Sci. Lett. 202:405-418) was used to show how decoupling of the pyroclastic current was triggered by both sea entrance and interaction with the topography. In the former case, the dense part of the current and the lithics transported by the dilute cloud went underwater. In the latter case, topographical barriers noticeably decelerated both parts of the decoupled current and favored sedimentation by partial or complete blocking. The resulting unloading of the dilute current drastically reduced the runout distance by triggering an early buoyant lift-off.

Introduction

Okmok volcano forms the northeastern part of Unmak Island, which lies in the middle of the Aleutian volcanic chain (Alaska, USA). With a volume of 400-500 km^3, the Okmok shield is among the largest volcanic centers in the Aleutian arc. Okmok's predominantly basaltic eruptive style was punctuated by catastrophic silicic-magma-bearing eruptions (Okmok I and II) that produced two nested, 10-km diameter calderas at the summit (Black 1975; Miller and Smith 1987). Intracaldera activity following the younger Okmok II caldera event formed numerous basaltic cones and lava flows. On-going deformation of the caldera floor has been recognized by SAR interferometry (Lu et al. 2000), and the most recent eruption was in 1997. Although numerous geologic (Byers, 1959) and geochemical observations (Byers, 1961) have been collected at Okmok, most were aimed at the questions of arc petrogenesis (e.g., Kay and Kay 1994) and physical processes of specific volcanic events to date have not been explored systematically.

The focus of this study is on the latest caldera-forming eruption, Okmok II, with the goal of establishing the physical parameters related to this volcanic event. The eruption has been dated at 2050 ± 50 BP (Wolfe 2001) and its deposits covered some 1000 km^2 of Umnak Island (Fig. 1). The products of this eruption consist of minor fall tephra overlain by voluminous, non-welded pyroclastic density current deposits. The bulk composition changes dramatically from rhyodacite in the first part of the fall deposits to basaltic andesite throughout the rest of the eruptive sequence (Larsen and Nye in review).

In this study, geological and sedimentological data of the fall deposits are utilized to reconstruct the eruptive dynamics of the earliest phase of the eruption, whereas data from the two facies of the pyroclastic density current deposits constrain the nature of the current. Interactions between the pyroclastic current and its surroundings (hills and sea) elucidate important characteristics of the current, such as internal particle concentration and thickness. These characteristics can be best explained by the kinematic model by Burgisser and Bergantz (2002), and this model is employed to infer the mean speed of the current at a given location and to determine whether the current was in sub- or supercritical regime.

Methods and theory

The topographic map was based on the 10-m resolution DEM of the USGS, and the geologic map of Byers (1959) was used for reference. Samples were localized by GPS (Fig. 1). In the fall deposits and stratified facies, most samples were bulk samples over the entire thickness of the unit, and some samples were of individual layers. The coarsest clast sizes of the stratified facies are much smaller than the sampling volume and are thus properly represented in the sieve data. In the massive facies, the sample volume was 10×10×10 cm. Because the sampling area was limited, the 3 largest clasts within a 2 m^2 area around the sampling area were also measured to ensure that the sampling properly represented the coarsest sizes. For all samples, the average diameter of those clasts is at most 1 ϕ size larger than the maximum clast size within the sampled material.

Most samples were dry-sieved and counted in the field for the coarsest fraction (> -2 ϕ). The remainder of the material was wet-sieved in the laboratory to 4.5 ϕ in intervals of 0.5 ϕ. The finer fraction (<4.5 ϕ) was collected in 2-gallon water buckets and dried. The size distributions of the fine fraction were determined to 7 ϕ using a Spectrex ILI-1000 laser particle counter. Although the particle counter gives wt.% between 4.5 and 10 ϕ, those values were normalized to sizes between 4.5 and 7 ϕ because the distilled water used to dilute the fine fraction contained impurities below 7 ϕ. Particle counter and sieve data were combined to obtain normalized grain size distributions. The error in the weight of each size fraction is estimated to less than 5 g for the field-sieved fraction and less than 0.1 g for the finer sizes. The error in the weight percent is thus estimated to 0.2% for the field-sieved fraction and 0.1% for the finer sizes. Grain sizes are given in ϕ units ($-\log_2$(mm)) and the parameters used in this study are the Inman median size M_d (50 wt.%) and sorting σ (Inman 1952; Cas and Wright 1987). Those parameters are accurate to ±0.1 ϕ. The componentry of samples was

obtained by manually separating and weighing a statistically significant number of the different clast types for sizes coarser than 0 ϕ, and by counting 500 particles per class size with a binocular microscope for the smaller sizes down to 2 ϕ (4 ϕ for some samples). Conversion to weight fraction was done using the average weight of each particle type. Errors on the normalized proportions are on the order of 0.1%. For each sample, the mean particle density is calculated to the nearest 100th of kg m^{-3} using the bulk component data with 1000, 2500, 2000 and 2500 kg m^{-3} being the respective densities of scoria, lithic, glass and crystal.

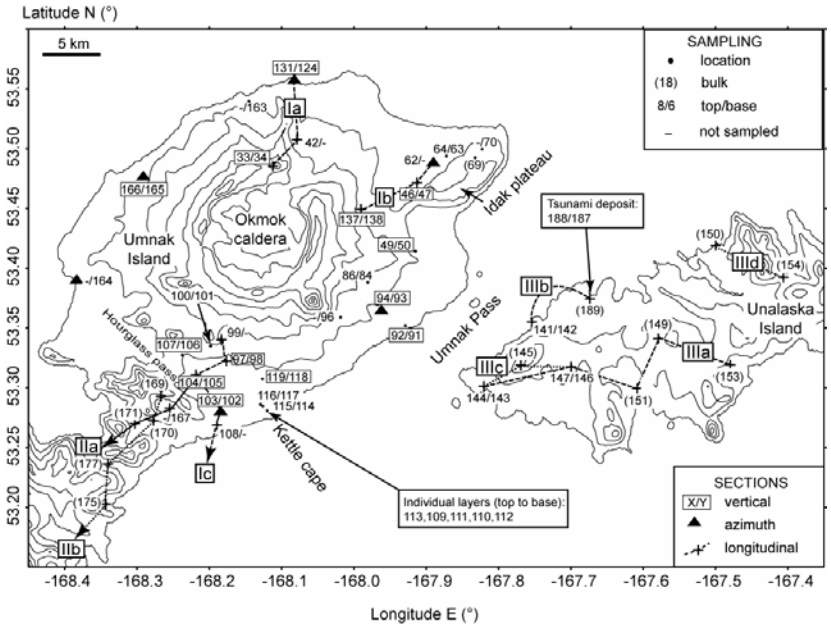

Figure 1 Sample localities of the pyroclastic current deposits. Geographic names are also indicated and contours intervals are 150 m. Localities with an asterisk have been used to study local vertical variations and the corresponding grain size data are reported in Fig. 8. Data of the azimuth section are in Fig. 10, sections Ia-c in Fig. 11, Kettle Cape in Fig. 12, sections IIa-b in Fig. 14, sections IIIa-b in Fig. 15, and sections IIIc-d in Fig. 17.

A brief summary of the model by Burgisser and Bergantz (2002) follows because it was used to derive dynamic parameters of the pyroclastic density current. In this kinematic template, the multiphase interactions of particles within the dilute part of the current are characterized with two dimensionless numbers: the Stokes (S_T) and stability (Σ_T) numbers. The Stokes number measures the coupling between gas and particles and is the ratio of the response time of particles (U_T/g, particle reaction to unsteady forcing by gas turbulence) to the rotation time of the most energetic eddies ($\delta_t / \Delta U_i$):

$$S_T = \frac{U_T \, \Delta U_i}{g \delta_i} \tag{1}$$

where U_T is the particle terminal fall velocity, g the acceleration of gravity, δ_t is the eddy diameter, and ΔU_i is the eddy rotation speed. ΔU_i can be related to both the root-mean square of the gas velocity U_{rms} and the mean current speed U by (Pope 2000):

$$\Delta U_i = \frac{\sqrt{88}}{e^2} U_{rms} \cong \frac{\sqrt{88}}{4e^2} U \tag{2}$$

The stability number assesses the steady gravitational forcing on particles and is a measure of the particle residence within an eddy:

$$\Sigma_T = \frac{U_T}{\Delta U_i} \tag{3}$$

The combination of S_T and Σ_T defines three main particle behaviors within the cloud: sedimentation ($S_T > 1$ and $\Sigma_T > 10^{-0.5}$), where particles are not sustained by turbulence and fall out; transport ($S_T < 1$ and $\Sigma_T < 10^{0.5}$), where particles are well mixed within the flow; and transient (other cases), where particles gather and disperse in a transient way. The buoyancy frequency ($\pi \Delta U_i / \delta_i$), which controls the rotation time of the most energetic eddies, can be combined with current height H and speed U to frame the Froude number F_R of the current:

$$F_R = \frac{U \delta_i}{4\pi H \Delta U_i} \qquad (4)$$

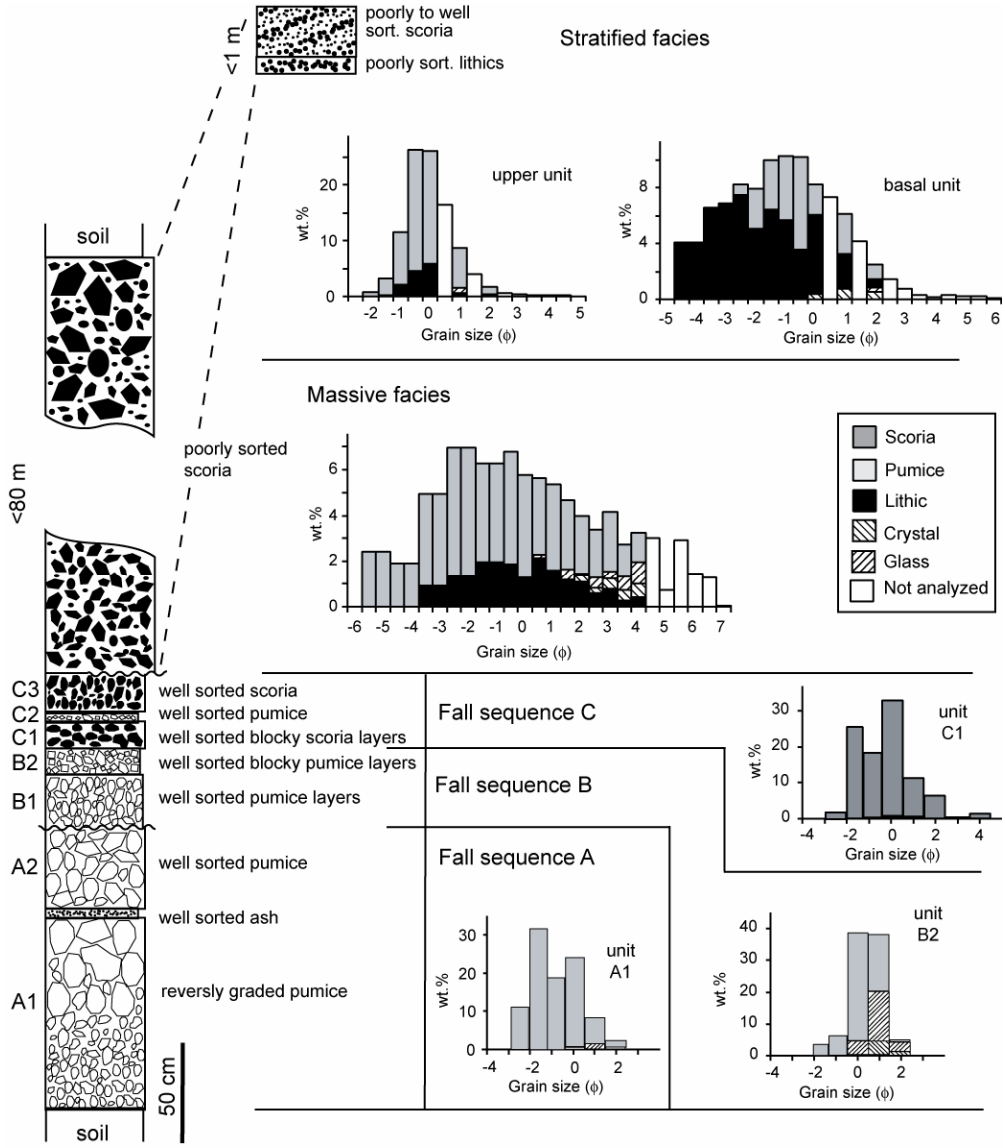

Figure 2 Composite stratigraphic section of the Okmok II eruptive products. Filled symbols are scoria; open symbols are pumice. Fall deposits are scaled to their maximum thickness, whereas the massive and stratified facies are not to scale. Representative grain-size distribution with components are given for the fall sequences A (A1, AOK6), B (B2, AOK22), C (C1, AOK10), the massive facies (AOK104), and the stratified facies (AOK117 for the basal unit and AOK70 for the upper unit). Samples AOK6 and AOK10 are at the location AOK131 while the sample AOK22 is at the location AOK86 (see Fig. 1).

Stratigraphy of the Okmok II eruption

The stratigraphy of the latest caldera-forming activity in Okmok shows that there were two major eruptive phases. The first phase produced three tephra fall sequences (A, B, and C, Fig. 2), whereas the second generated a voluminous ignimbrite. Enough locations were found to

reconstruct the distribution of the fall deposits, although the fall deposits are often buried underneath the pyroclastic current deposits. The initial fall sequence mostly covers the northern sector of the volcano (Fig. 3), whereas the two other sequences occur east, extending to the nearby Unalaska Island (Figs. 4 and 5). The method of Pyle (1989) was used to estimate tephra volumes, and two type sections were used to reconstruct the fall stratigraphy. The first type section is located ~9 km north of the caldera rim near the shore (star symbol in Fig. 3) and the second is located ~12 km east of the caldera rim (star symbol in Fig. 4). Each fall sequence has been divided into several units (A1-2, B1-2, and C1-3) illustrated in Fig. 2. This eruption produced both scoria and pumice with distinct compositions. Tan pumices, composing the bulk part of the fall deposits, are rhyodacitic in bulk composition, whereas black scoria, composing the pyroclastic current deposits, are basaltic andesite (Larsen and Nye, in review).

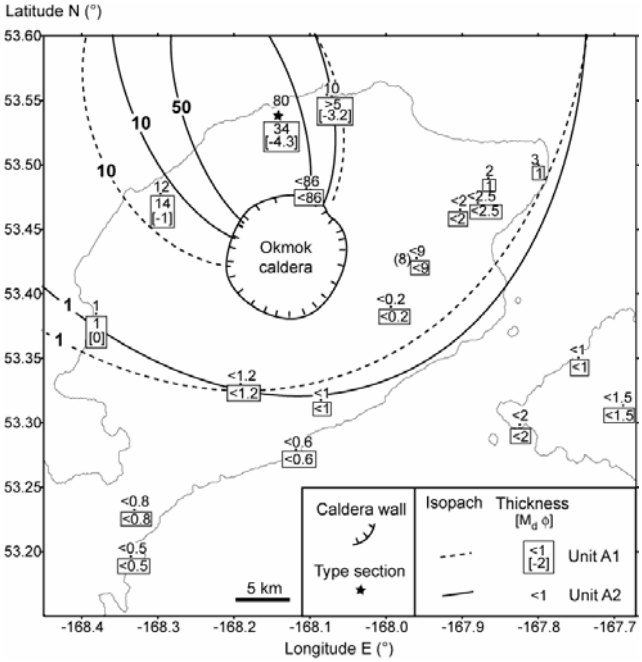

Figure 3 Thickness distribution of fall sequences A1 and A2. Signs > and < indicate minimum and maximum thickness, respectively. Isopachs for each sequence are in centimeters; the star indicates the type section, and the median grain size M_d (ϕ) is given for some locations.

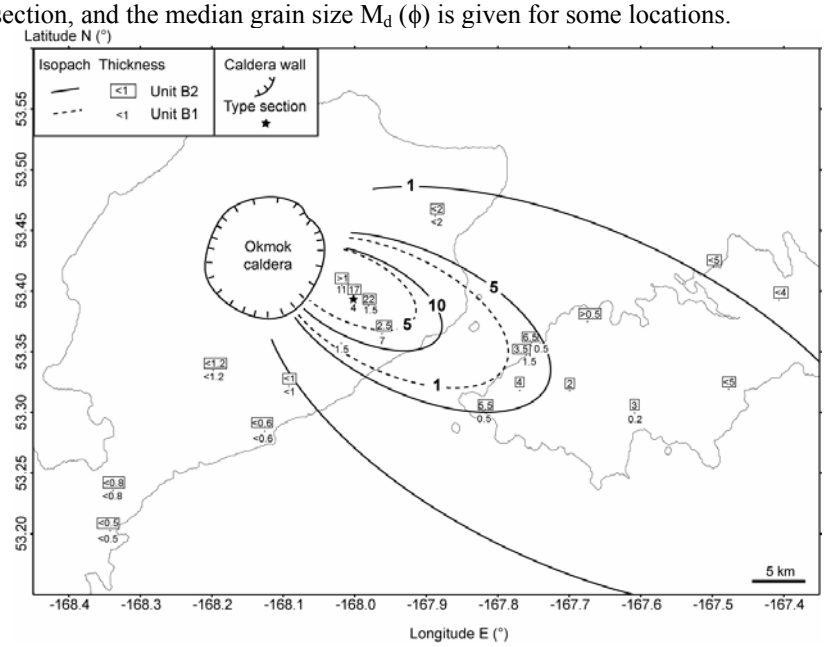

Figure 4 Thickness distribution of fall sequences B1 and B2. Signs > and < indicate minimum and maximum thickness, respectively. Isopachs for each sequence are in centimeters and the star indicates the type section.

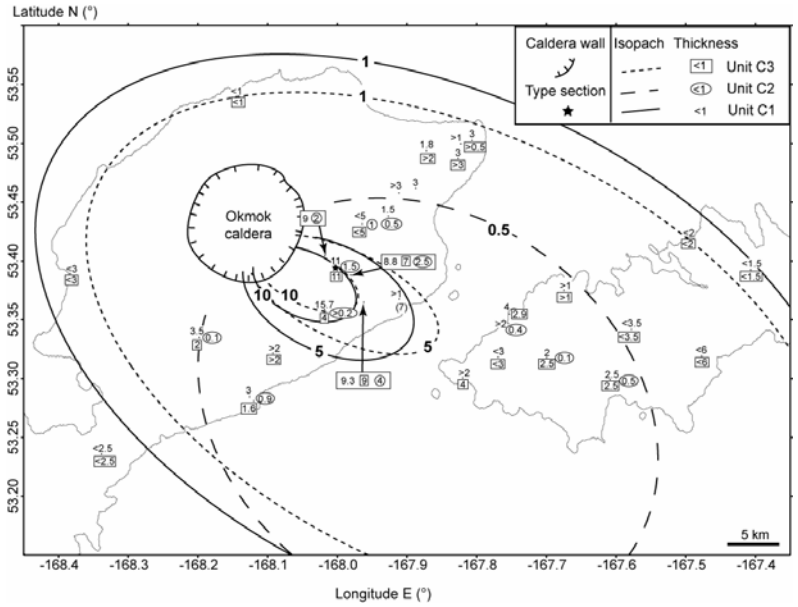

Figure 5 Thickness distribution of fall sequences C1, C2, and C3. Signs > and < indicate minimum and maximum thickness, respectively. Isopachs for each sequence are in centimeters and the star indicates the type section.

Fall deposits

Fall sequence A is the lowermost unit of the Okmok II eruptive sequence and consists of tan pumice lapilli with rare lithics. It commonly overlies a thick (>30 cm) soil with carbonized plant remains at the contact. Some carbonized weeds were in their original living position within unit A1. Sequence A is up to 114 cm thick at the reference section (Fig. 3) and it can be subdivided into a reversely graded layer (A1, Fig. 2) varying from fine ash (median grain size M_d=0 ϕ) to coarse lapilli (M_d=-4.3 ϕ), and an ungraded layer of lapilli A2 (M_d=-1 ϕ). Both units are well sorted (σ=0.6), and are separated by a fine ash deposit (M_d=3.8 ϕ) that is only present near the reference locality. The distribution map of A1 and A2 indicates a NNW dispersal axis (Fig. 3) with a total volume of ~0.4 km^3. Median grain sizes of unit A1 are indicated at four localities, and density measurements reveal that the coarsest pumices average 500 kg m^{-3}.

Fall sequence B is finely stratified and consists of brown pumice lapilli. The sequence is up to 21 cm thick with M_d=0.5 ϕ at the reference section (Fig. 4) and two groups of layers can be recognized based on pumice morphologies. The basal group of layers (unit B1) contains vesicular pumices with irregular shapes, similar to the ones from sequence A, whereas the upper group (unit B2) consists of poorly vesicular pumices with blocky shapes (Fig. 2). Up to 50 wt.% of these blocky pumices is vesicle-free glass. The distribution map of B1 and B2 indicates an easterly dispersal axis with a volume of ~0.05 km^3 (Fig. 4). A small amount of erosion or reworking exists between the sequences A and B, but there is little evidence for a significant time break at this horizon, such as would be marked by soil development or abundant reworking by water.

Fall sequence C can be found on the northeast part of Umnak Island and on most of Unalaska Island, but it has been eroded from many exposed locations. The sequence is up to 20 cm thick at the reference section (Fig. 4), where up to 10 layers can be recognized, with grain sizes that vary from fine ash (M_d=3 ϕ) to fine lapilli (M_d=-0.5 ϕ). Although sequence C consists mainly of black scoria lapilli layers, one layer contains vitric and blocky pumice ash. All layers have rare lithics. The pumice-bearing layer delimits three groups of layers within sequence C: 8 layers of scoria at the base (unit C1), the pumice layer (unit C2), and a scoria layer atop (unit C3, Fig. 2). The distribution map of C1, C2, and C3 indicates an easterly dispersal axis and a volume of ~0.4 km^3 (Fig. 5).

Pyroclastic current deposits

Pyroclastic current deposits from the Okmok II eruption blanket the northeast part of Umnak Island, forming plateau surfaces around the volcano that are cut by modern stream channels (Fig. 6). These black, scoria-rich deposits generally overlie fall sequences with a sharp contact, and occasionally present an erosive contact with underlying soil or older deposits. Most of the deposits are several tens of meters thick and present a massive, poorly sorted facies. Another facies with low angle cross-stratification or planar bedding, and improved sorting occurs on hills and paleohighs (e.g., Idak plateau), where deposits are only up to a few decimeters. A similar stratified facies is systematically found on Unalaska Island, where deposits vary in thickness from one meter on the western shore to a few centimeters inland (Fig. 6). Clasts composing the pyroclastic deposits can be divided into four types: juvenile scoria, lithics, crystals and glass. Black scoria is the most abundant type. Lithics comprise mostly aphyric basalt, minor basement clasts, hydrothermally altered clasts, and red oxidized scoria lithics that are frequently found in the pre-caldera stratigraphic sequence. Crystals are mostly plagioclase, with minor olivine and pyroxene. Most crystals are unbroken, and some crystals have adhering glass. Glass is mostly juvenile, but also includes some aphyric basalt, from which the distinction is difficult.

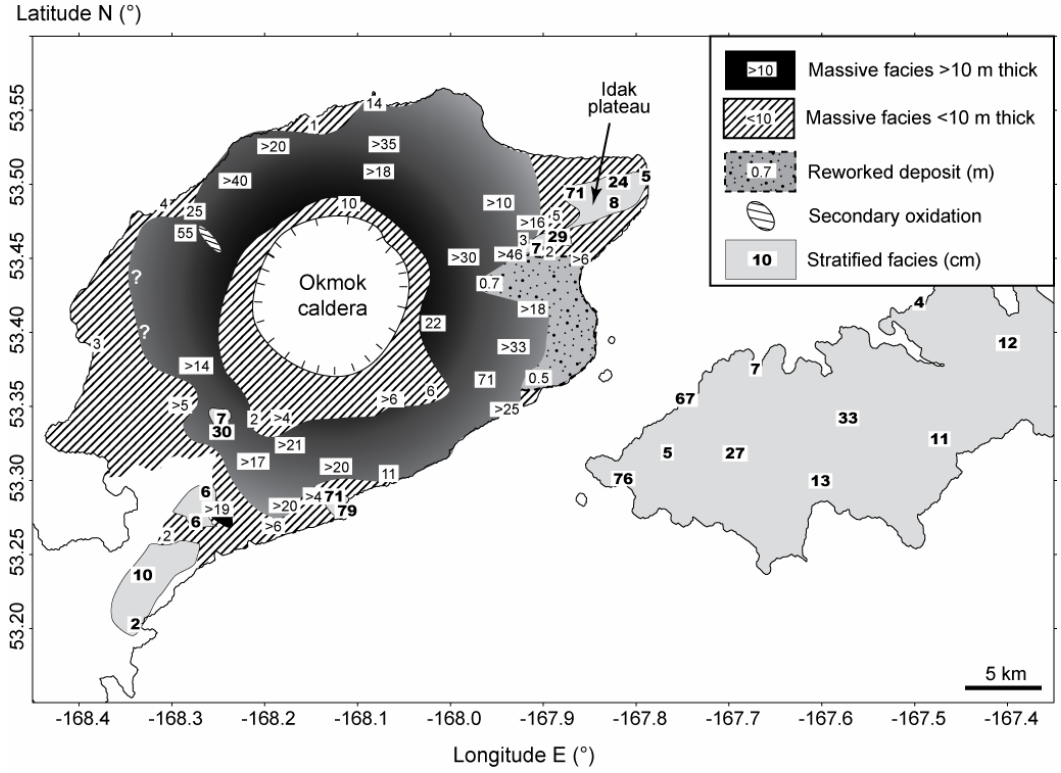

Figure 6 Thickness distribution of the pyroclastic current deposits. Massive facies, stratified facies, and post-depositional reworking are indicated. Massive facies thickness is in meters, whereas stratified facies thickness is in centimeters (bold numbers). The sign > indicates minimum thickness.

The total volume of pyroclastic deposits on land is estimated at 24 km^3, and the massive facies accounts for >99.8% of the total volume. Assuming a Dense Rock Equivalent of 2500 kg m^{-3}, and a deposit average density of 1450 kg m^{-3} from the massive facies componentry, this volume translates into ~14 km^3 DRE. Preliminary surveys of the Okmok I deposits and the intra-caldera geology suggest that the volume of the preexisting caldera left by Okmok I is similar to the volume of infillings by post-caldera basalt and tephra. It is thus reasonable to assume that the post-Okmok II infillings balance the volume of the pre-Okmok II caldera, and that the current volume of the caldera (40 to 60 km^3) is representative of the total volume of erupted material during Okmok II. Okmok II thus erupted ~50 km^3 (~29 km^3 DRE), half of which was deposited on land.

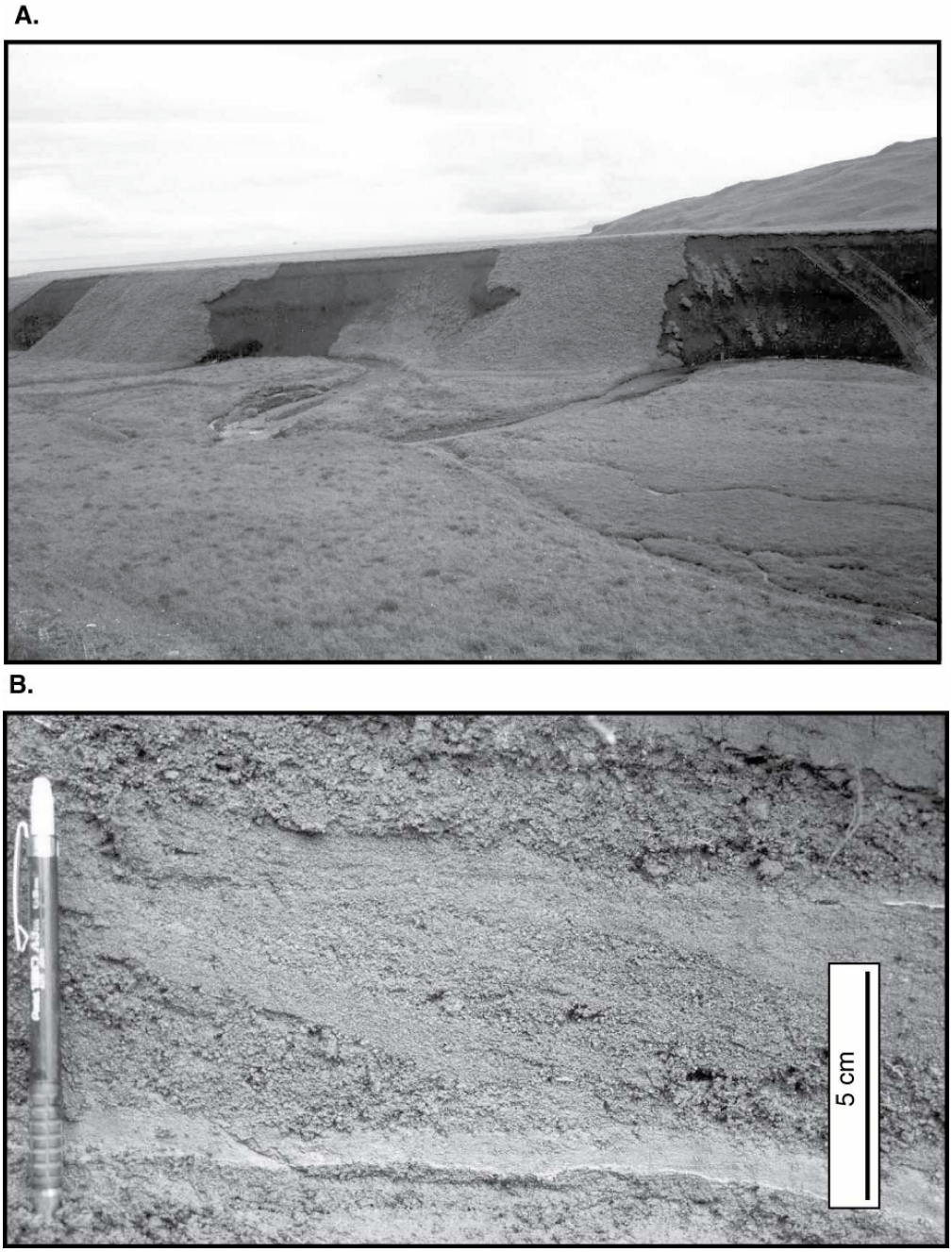

Figure 7 Field examples of the pyroclastic deposits. **a.** Massive facies near Hourglass Pass (AOK 103, see Fig. 1 for locations). Note the flat upper surface of the ~ 25 m thick deposit. **b.** Stratified facies at locality AOK69. Note the cross bedding inclined from the upper left to the lower right of the photograph.

Massive facies of the pyroclastic current deposits

The thickness of the massive facies varies greatly, but the integration of visual estimates and tape measurements suggests that the thickness averages from ~ 60 m proximally to ~ 30 m at shore, at about 10 km from the caldera rim (Fig. 6 reports tape measurements). The top surface of the deposits forms a gently inclined plateau (Fig. 7), whereas the base is more irregular, revealing the jagged nature of the paleorelief. Thus, most thickness variations of the massive deposit result from the wavy paleotopography. Deposits are primary, with the exception of two regions that have been reworked (Fig. 6). The first region is located east of the caldera and features thick outcrops with rounded scoria, over-sized (>1 m) rounded lithic boulders, and numerous crude planar stratifications. These outcrops and several localities with thin (<1 m) volcano-sedimentary deposits suggest a subsequent reworking of the pyroclastic deposits with water on the eastern part of the island. The second region lies northwest of the

caldera, where deposits display abundant red oxidized scoria with a few lithic pipes. These regions were avoided for the reconstruction of the eruptive dynamics. Although the most of the massive facies is uniform, occasional crude stratifications are observed where thickness variations are important. Common accumulations of coarse scoria occur where the deposit thins to about one meter, and scarce occurrences of a thin (<10 cm) lithic-rich unit at the base were found on the lee side of paleohighs. On average, the massive facies consists of 69 wt.% juvenile scoria, 26 wt.% lithics, and 5 wt.% glass and crystals (Fig. 2), with median grain sizes ranging between –2.5 and 0 ϕ and poor sorting (σ~3, Fig. 8). Crystals are generally smaller than 1 ϕ and glass becomes more abundant below 0 ϕ, whereas scoria and lithics occur at all grain sizes.

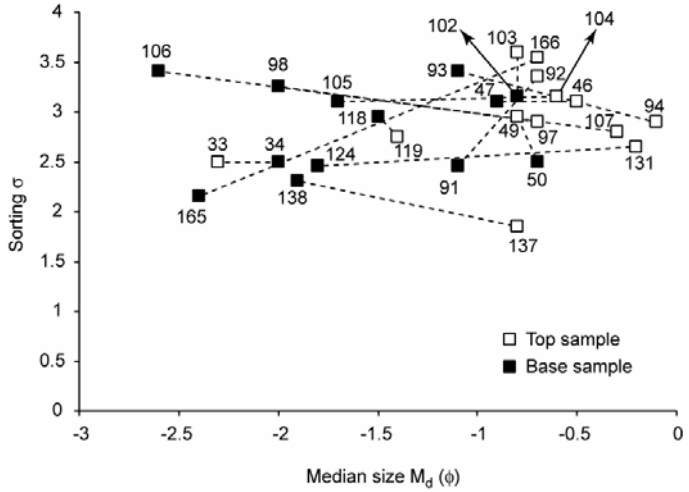

Figure 8 Changes in sorting (σ) with median grain size for sample pairs within the massive facies of the pyroclastic current deposits. Basal samples (filled symbols) are linked to the top samples (open symbols) of the same locality.

Local vertical variations of the massive facies were characterized by determining grain-size distributions and components of samples from the base and the top of various localities around the volcano (Fig. 1). Median grain sizes usually decrease by 1 ϕ size towards the top of the deposit with no change in sorting (Fig. 8). Bulk lithic contents vary by up to 20 wt.%, regardless of stratigraphic position (Fig. 9). To examine if a particular size class is responsible for these bulk variations, the difference in normalized lithic proportion between two neighboring samples are plotted for each grain size. By convention, the component data of the sample appearing to the right is always subtracted from the component data of the sample to the left of the diagram. For example, the bulk componentry of the sample AOK98 at the base of the deposit contains 17 wt.% more lithics than the sample AOK97 at the top (Fig. 9). The line labeled ‘lithics’ between these two samples indicates the arithmetic difference in lithic content for each grain size indicated on the x-axis (i.e. lithic wt.% in AOK98 minus lithic wt.% in AOK97 for each size class). This graphic representation shows that the difference in lithic bulk content between these two samples is caused by a higher lithic content of AOK98 between -5 and –1 ϕ (Fig. 9). From the four localities represented on Fig. 9, it is apparent that the vertical variations of lithic content within the deposit are caused by the coarsest clast fraction (above -2 ϕ). Vertical variations of crystal and glass proportions are small regardless of grain size.

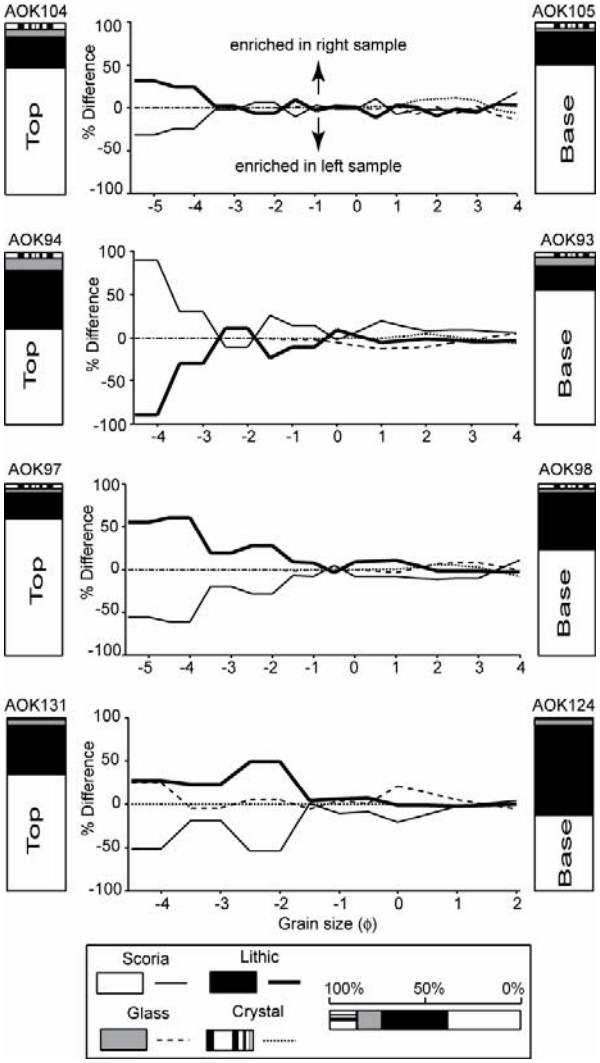

Figure 9 Component variations with grain size within the massive facies of the pyroclastic current deposits. Samples on the left-hand side are from the top of the deposit, whereas samples on the right-hand side are from the base (Fig. 1 for sample locations). Component data at each grain size of the sample displayed on the left is always subtracted from the comparative size class of the sample to the right. Each line thus corresponds to the difference in wt.% normalized to 100% for that component (lithic, scoria, crystal, or glass).

Twenty-six samples taken at various azimuths around the caldera, 8 to 12 km from the rim, were analyzed to study radial variations of the massive facies. Six representative samples located at regular intervals of azimuth around the caldera were selected for component determination (triangle symbols on Fig. 1). Sorting and median sizes display weak variations around the volcano (Fig. 10A). As in the vertical sections, small componentry changes are due to the coarse fraction (Fig. 10B). Lithic proportions vary between 9 and 38 wt.%, with smallest values on the west of the volcano. Note that the lowest lithic content occurs at a locality (AOK164) that displays depletion in lithics regardless of grain size. Both this depletion and the improved sorting (σ=2.4) of this thin (2.5 m) locality reflect a frequent pattern occurring when deposits thin because of important paleo-relief. There is indeed a general correlation between thinness and the presence of very crude stratification, and locally some strata feature better sorting in size and density than others.

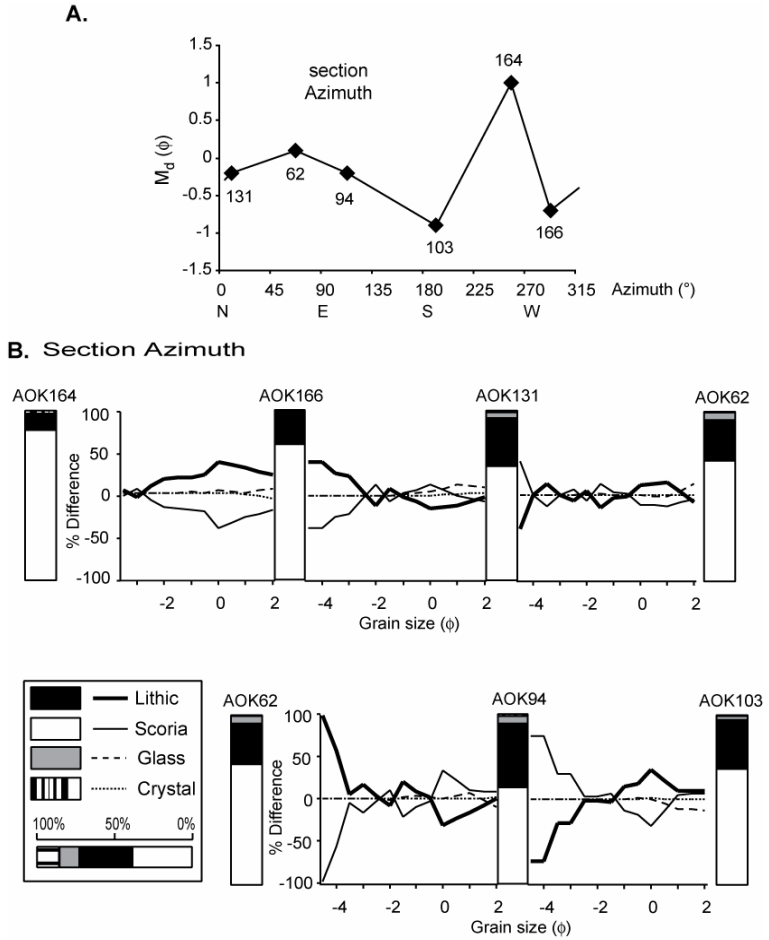

Figure 10 Grain size and component variation with grain size of the azimuth section (see Fig. 1). **a.** Changes in median grain size with azimuth from the caldera center (0° is North). **b.** Component variation with grain size. Component data at each grain size of the sample displayed on the left is always subtracted from the comparative size class of the sample to the right.

Eleven samples from three longitudinal sections around the volcano were analyzed to study proximal-to-distal variations of the massive facies (sections Ia-c on Fig. 1). In the northern section Ia, median grain sizes decrease by 2 ϕ units with distance from source with no change in sorting (Fig. 11a). Lithic contents increase by 20 wt.% with distance because of the coarse fraction, and glass contents rise slightly (Fig. 11b). In the northeastern section Ib, there is a modest decrease in median grain sizes by 1 ϕ unit (Fig. 11a). Whereas the proximal sample is moderately sorted (σ=1.9), more distal samples display the characteristic poor sorting of the massive facies. Bulk lithic contents decrease markedly (50 wt.%) with distance and the variations are mostly concentrated in the coarsest fraction (Fig. 11c). In the southern section Ic, median grain sizes decrease by 2 ϕ units, with no change in sorting (Fig. 11a). Bulk lithic contents vary by less than 25 wt.% with no systematic trend and the variations are mostly concentrated in the coarsest fraction (Fig. 11d). In all sections, crystal and glass proportions do not significantly vary.

In summary, the characteristics of the massive facies have similar trends regardless of azimuth despite its variable thickness. On a local scale, the base of the deposit is coarser and more variable than the top (Fig. 8), whereas in all sections there is a decrease in median grain size with distance from source without significant change in sorting. Lithic contents vary by about 20 wt.%, with most of the variation concentrated in the coarsest sizes (>-2 ϕ) of the distribution, which creates a general trend of coarse-tail grading, with lithic-rich base and scoria-rich top. Changes in components between intermediate and distal locations are irregular and often less pronounced than vertical variations recorded at a given location.

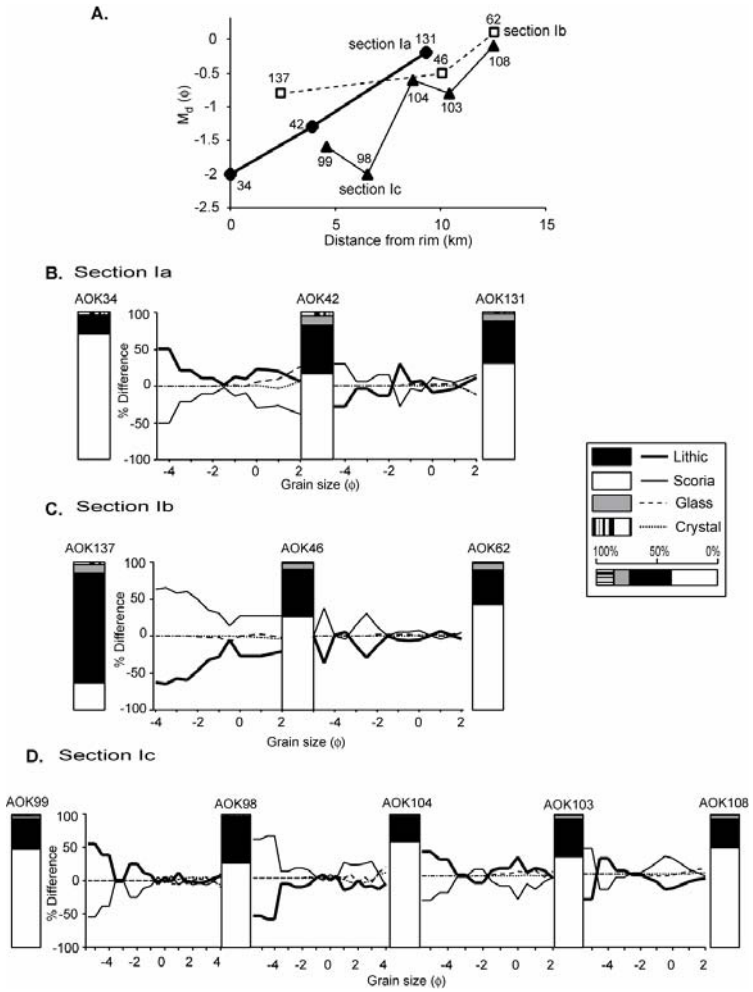

Figure 11 Grain size and componentry of the massive facies with distance from source. Component data at each grain size of samples to the left of the diagram is subtracted from the comparative size class of samples to the right. **a.** Changes in median grain size with distance from the caldera rim for sections Ia-c (see Fig. 1). **b.** Component variation with grain size of section Ia. **c.** Component variation with grain size of section Ib. **d.** Component variation with grain size of section Ic.

Stratified facies of the pyroclastic current deposits

The thickness of the stratified facies varies between 30 and 70 cm proximally and averages about 20 cm at ~20 km from the caldera rim (Fig. 6). The stratified facies is found only on tops of hills, such as Kettle Cape to the south, or elevated plateaus, such as Idak to the northeast (Fig. 1), and many locations display evidence of erosion. These areas are exposed to the high winds common in the Aleutian Islands, and the loose nature of these relatively thin deposits accounts for their low preservation potential. Although many thickness measurements are minimum values because of erosion, it is likely that the stratified facies thins with distance. The thickness of the stratified facies is more uniform than that of the massive facies.

The stratified facies can generally be divided in two units based on components. The basal unit is richer in lithics, with an average of 60 wt.% scoria, 35 wt.% lithics, and 5 wt.% glass and crystals, whereas the upper unit is richer in scoria with an average of 79 wt.% scoria, 15 wt.% lithics, and 6 wt.% glass and crystals (Fig. 2). Scoria and lithics occur at all grain sizes, whereas crystals are generally smaller than 1 ϕ and glass becomes more abundant below 0 ϕ.

The basal unit is generally massive and poorly sorted (σ=2) around the volcano, and varies little in grain size with distance (Fig. 12a). Grain size distributions show that it is generally coarser and better sorted than the upper unit (Fig. 12b). Differences in componentry with size between the two units show that fractions coarser than –0.5 ϕ are the source of lithic enrichment (up to 30 wt.%) of the basal unit (Fig. 12c).

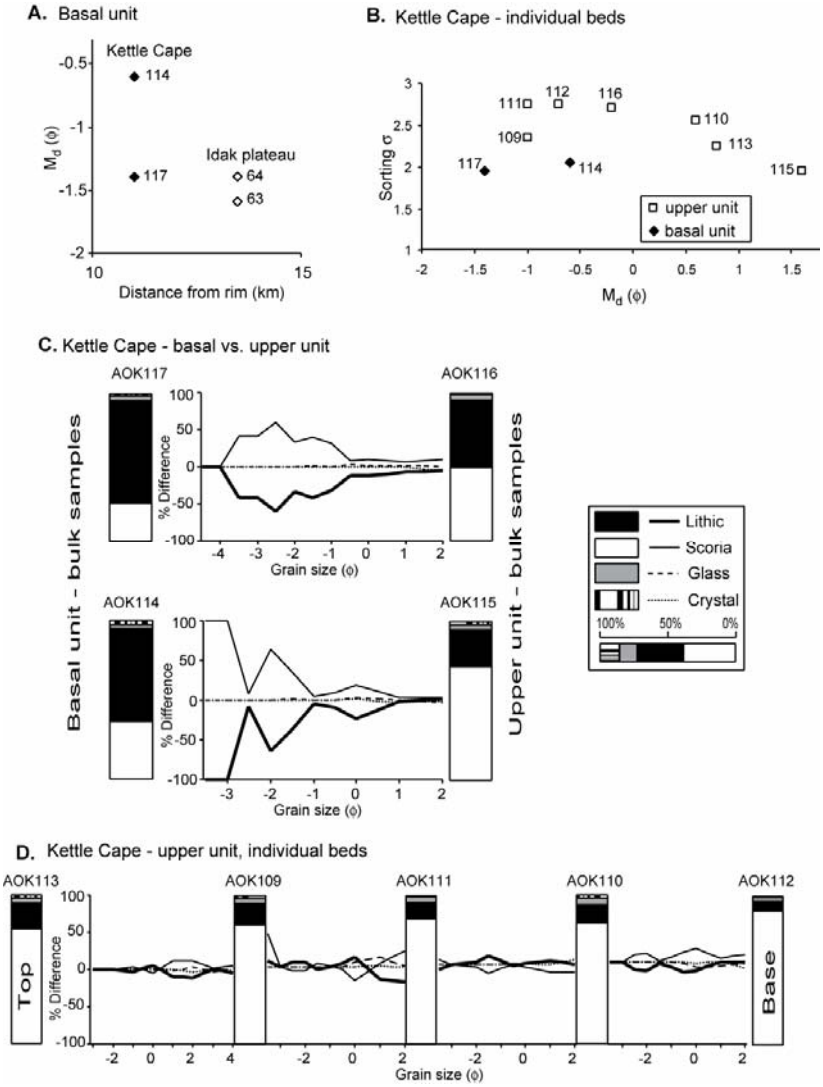

Figure 12 Grain size and componentry of the stratified facies on Umnak Island. **a.** Changes in median grain size with distance from the caldera rim for the basal, lithic-rich unit. **b.** Changes in sorting with median grain size of individual layers within the stratified facies at Kettle cape. **c.** Component variation with grain size of the basal unit vs. the upper unit at Kettle cape. Component data at each grain size of samples to the left of the diagram is subtracted from the comparative size class of samples to the right. **d.** Component variation with grain size of individual layers within the upper unit at Kettle Cape.

The upper unit exhibits alternating planar stratification, absence of stratification, and low-angle cross bedding with gradational or sharp transitions between individual beds. No systematic variations, either vertically or horizontally, between these various patterns could be found, most likely because of the paucity of outcrops. The stratified nature of the deposits implies a large local variability of sorting and median size that depends on the exact size and position of the bulk sample. This variability can be illustrated by the change in median size of individual layers within the upper unit at Kettle Cape (Fig. 12b). The componentry between individual layers from the same locality does not vary significantly (Fig. 12d).

Relationship between massive and stratified facies

The transition between massive and stratified facies systematically occurs at the flanks of prominent ridges. The massive deposit usually thins uphill from tens of meters to meters with the occasional appearance of crude stratifications and laterally changes to stratified facies within meters. Stratigraphic correlations on the south side of Idak plateau (Fig. 13a) and at Hourglass Pass indicate that massive and stratified facies are a lateral variation of the

pyroclastic deposits, rather than a vertical succession (see composite cross section in Fig. 13b). A lithic-rich unit is often present at the base of the stratified facies, but more rarely at the base of the massive facies, where it is preserved only on the lee side of paleohighs (e.g., north of Kettle Cape). Accumulations of coarse scoria are regularly found around the volcano where the deposit thins to about one meter while remaining massive in texture. These accumulations display a sharp peak of coarse scoria (Fig. 13b), whereas the fine tail has a componentry similar to the main body of the massive facies. Importantly, a scoria accumulation near Hourglass Pass occurs at the facies transition between massive and stratified (AOK100, Fig. 1).

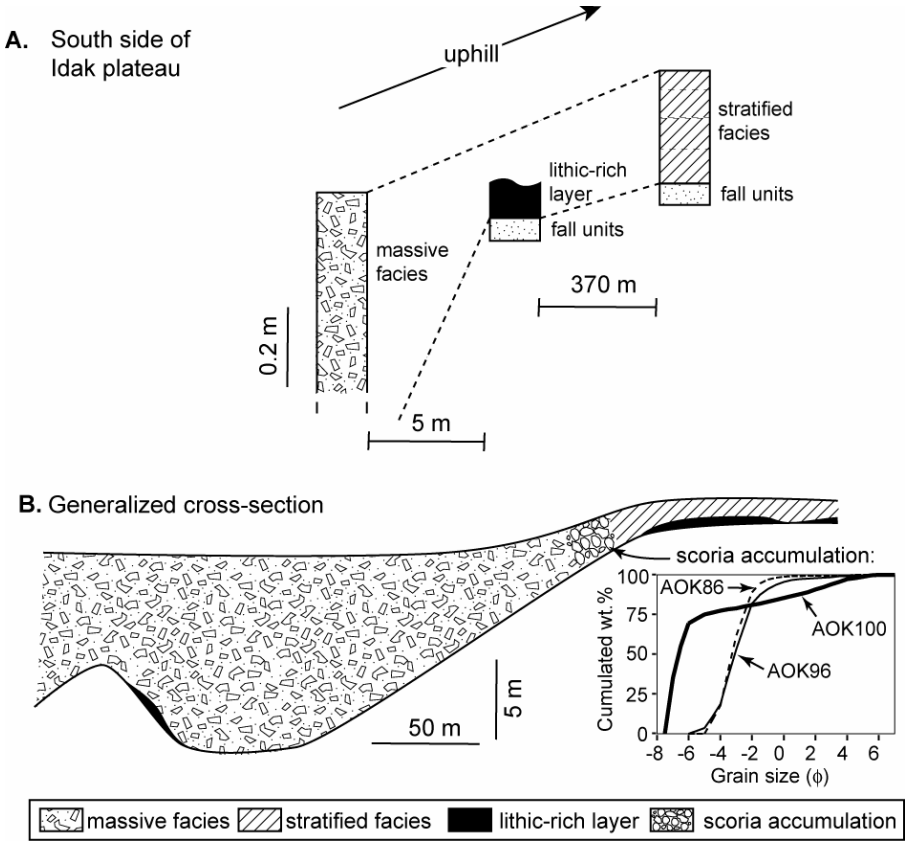

Figure 13 Lateral (cross-stream) facies variations within the pyroclastic current deposits. **a.** Stratigraphic correlation between massive and stratified facies on the south side of Idak plateau. The stratified facies has been eroded at the middle section and no scoria accumulation has been found at that location. **b.** Schematic interpretation of the lateral changes in facies at Okmok. The inset shows cumulative grain size distribution of 3 samples of scoria accumulations (Fig. 1 for sample locations).

Southwestern Ridges

Okmok peninsula is linked to the southwest part of Umnak Island by an isthmus with rugged topography, where altered Tertiary volcanic rocks form a succession of northwestward ridges (Byers 1959). To study the relationship between pyroclastic current deposits and topography across these ridges, two transects were collected within massive (IIa) and stratified (IIb) facies, respectively (Figs. 1 and 14a).

The massive facies is thicker than 20 m before and after the first ridge, and thins rapidly to a few meters after the second ridge. The median grain size decreases with distance at the same rate before and across the two ridges, with similar poor sorting (Fig. 14b). Componentry changes little with distance: lithic contents oscillate by less than 10 wt.% because of the coarse fraction (Fig. 14c).

The stratified facies has a variable thickness of about a decimeter across the three first ridges, but thins to a few centimeters after the fourth ridge (Fig. 14a). The median grain size decreases slowly with distance across the first three ridges, and diminishes rapidly after the fourth ridge, whereas the sorting remains good (σ~1.5) regardless of distance (Fig. 14b). The componentry does not change across the two first ridges (NE-SW), but lithics of all sizes increase by 20 wt.% across the third ridge and glass clasts of all sizes (i.e. <0.5 ϕ) considerably increase by 35 wt.% across the fourth ridge, at the most distal locality (Fig. 14d).

In summary, the proximal rate of decrease in grain size is similar in both facies. Interestingly, size distributions of stratified facies at a given location match the coarse half of massive facies at the same location (Fig. 14b). This relationship seems true in general, because it is also verified on the north side of the Idak plateau and at Kettle Cape.

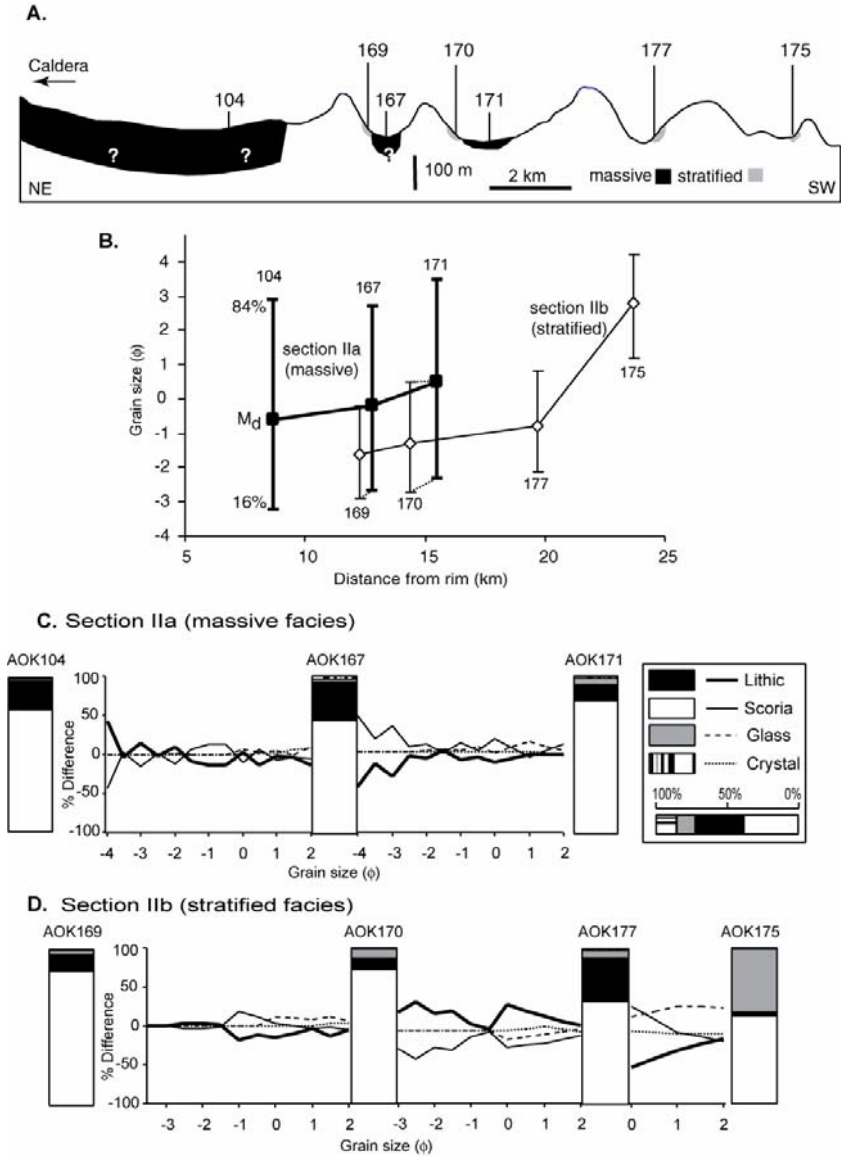

Figure 14 Grain size and componentry of the massive and stratified facies on the southwest of Okmok. Massive and stratified facies data are grouped in sections IIa and IIb, respectively (see Fig. 1). Component data at each grain size of samples to the left of the diagram is subtracted from the comparative size class of samples to the right. **a.** Cross section following the position of section IIb across four ridges with sample locations. **b.** Changes in median grain size with distance from the caldera rim. **c.** Component variation with grain size of the massive facies. **d.** Component variation with grain size of the stratified facies.

Unalaska Island

Pyroclastic deposits cover over half of the western part of Unalaska Island, which is separated from Umnak Island by an 8-km wide strait (Umnak Pass, Fig. 1). They occupy the same stratigraphic position as the ones on Umnak, directly overlying the fall deposits. These deposits vary from ~70 cm proximally to ~10 cm distally and they are generally structureless with discontinuous crude planar bedding. Unlike on Umnak Island, these stratified facies can generally be divided into a thin lithic-rich upper layer (78 wt.% scoria, 14 wt.% lithics, and 8 wt.% glass and crystals) and a lithic-poor basal layer (88 wt.% scoria, 5 wt.% lithics, and 7 wt.% glass and crystals). The distinction between the two layers is only apparent from the component data and cannot be ascertained in the field. Taking in account that the respective thickness of each layer is only constrained by the sampling interval, the upper layer forms about a third of the total thickness. Some outcrops present slight post-depositional disturbances probably linked with the high void fraction of the basal layer that may favor downward migration of small, denser lithics from the upper layer. To compare trends between localities with similar path history (land or water), the localities on the plateau inland (sections IIIa and c, Fig. 1) were separated for each layer from the ones directly at the shore (sections IIIb and d, Fig. 1).

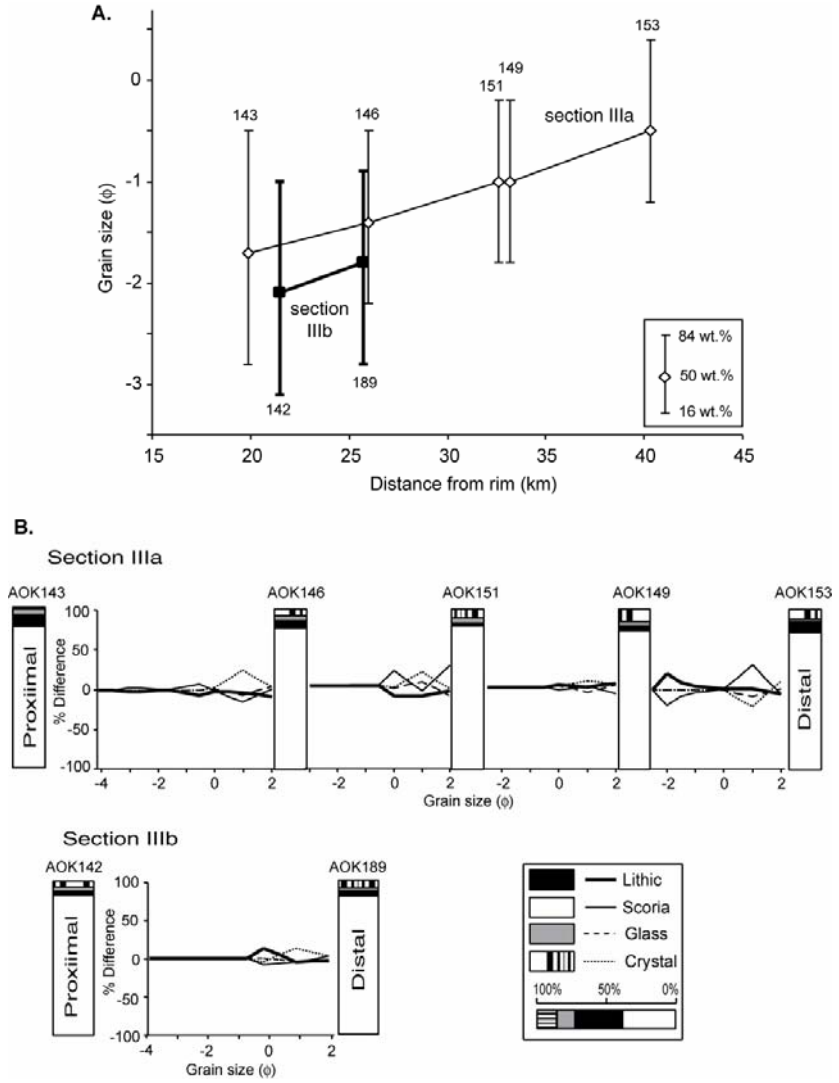

Figure 15 Grain size and componentry of the basal unit of the stratified facies on Unalaska Island. Data are grouped into section IIIa at shore and IIIb on the plateau (see Fig. 1). Component data at each grain size of samples to the left of the diagram is subtracted from the comparative size class of samples to the right. **a.** Changes in median grain size with distance from the caldera rim. **b.** Component variation with grain size.

The thickness of the basal layer decreases rapidly on the western coast (section IIIa) and thins gently across the plateau (Fig. 6). Grain size distributions are unimodal and the sorting improves slightly with distance (Table 1). Grain sizes decrease gently with distance both along the shore and across Unalaska's plateau (Fig. 15a). Interestingly, grain sizes sharply decrease between equidistant localities at shore (section IIIa) and on the highlands (section IIIb). The componentry of the basal layer remains remarkably constant over all locations (Fig. 15b).

The thickness of the upper layer is hard to survey because it has been partially reduced by erosion. The basal layer is always present below the upper layer except at one locality (AOK145), where only the upper layer crops out. Size distributions are bimodal near the shoreline, causing large sorting coefficients (Table 1), but the bimodality diminishes away from shore (Fig. 16). After remaining constant near the coast (section IIIc), median grain sizes decrease sharply inland (Fig. 17a). The componentry of the upper layer significantly varies across all grain sizes regardless of distance or location (Fig. 17b).

Some localities near the shore, generally below 15 m in altitude, exhibit erosion of the stratified deposit, which is overlain by a decimeter of fine sand in turn capped by a meter of a similar sand layer (Fig. 18, Table 1). The two sandy units are separated by an erosive contact. The lower sand unit is well sorted ($\sigma = 0.85$) with a median size of 0.5 ϕ, whereas the upper unit is bimodal with the same mode as the lower layer plus a coarser mode of -1 ϕ. Both sandy units contain clast types similar to the stratified deposits: 80 wt.% lithics, 14 wt.% scoria, and 6 wt.% glass and crystals.

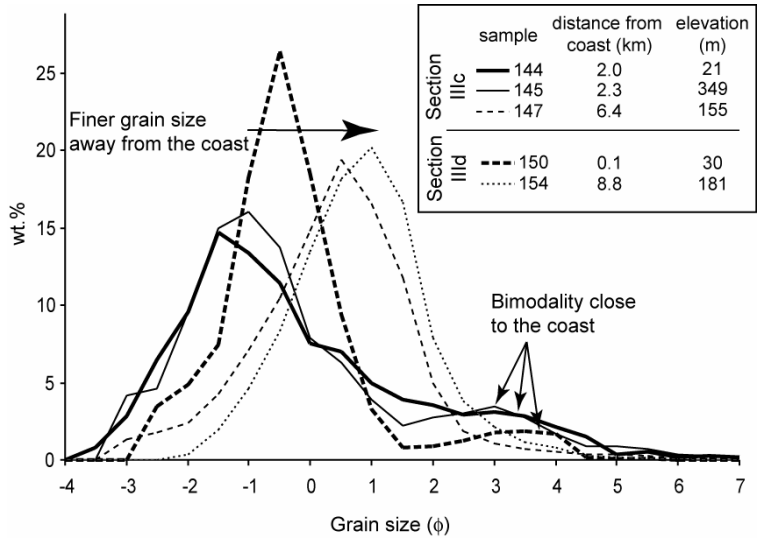

Figure 16 Grain size distribution of the upper unit of the stratified facies on Unalaska Island. Note that the bimodality of the coarser samples coincides with their proximity to the coast.

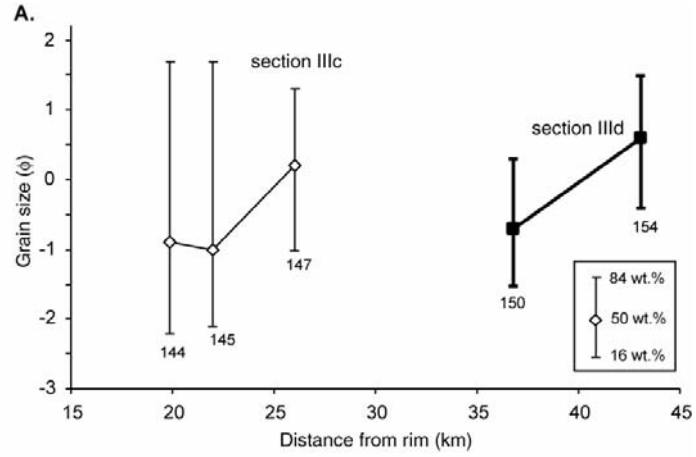

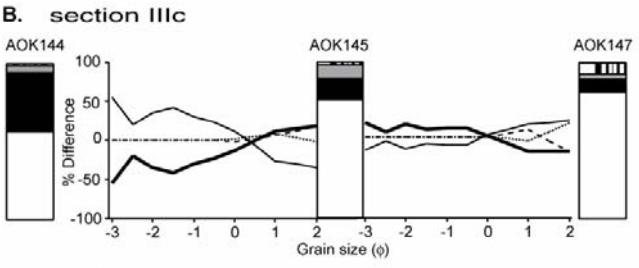

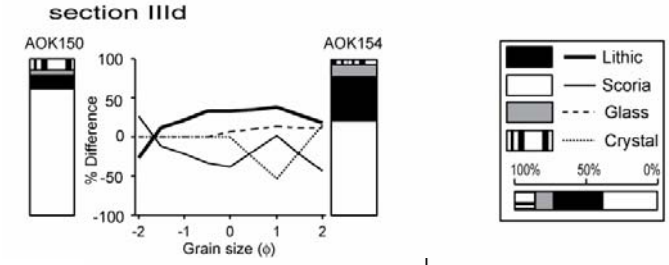

Figure 17 Grain size and componentry of the upper, lithic-rich unit of the stratified facies on Unalaska Island. Data are grouped in section IIIc at shore and IIId on the plateau (see Fig. 1). Component data at each grain size of samples to the left of the diagram is subtracted from the comparative size class of samples to the right. **a.** Changes in median grain size with distance from the caldera rim. **b.** Component variation with grain size.

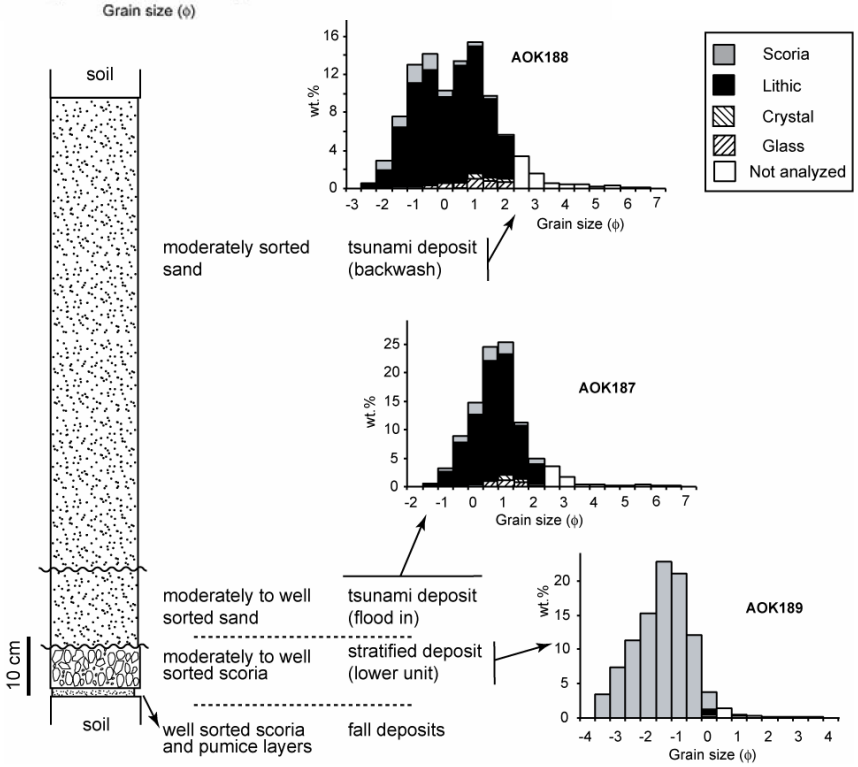

Figure 18 Stratigraphy of the western coast of Unalaska with representative grain size distribution and componentry. The two upper sandy units were only found below 15 m of altitude (Fig. 1 for samples location).

Table 1 Grain size parameters for the stratified facies.

sample	5 wt.% (ϕ)	16 wt.% (ϕ)	50 wt.% (ϕ)	84 wt.% (ϕ)	95 wt.% (ϕ)	sorting (σ)	distance from rim (km)
Idak plateau							
AOK63	-4.8	-3.7	-1.6	0.5	2	2.1	13.5
AOK64	-4.8	-3.6	-1.4	0.5	1.6	2.05	13.5
AOK69	-0.8	0.5	2	3.4	4.3	1.45	16.6
AOK70	-1.4	-1	-0.3	0.5	1.3	0.75	17.5
Kettle Cape – basal unit							
AOK117	-4.4	-3.4	-1.4	0.5	1.7	1.95	11
AOK114	-3.2	-2.4	-0.6	1.7	3.2	2.05	11
Kettle Cape – upper unit							
AOK116	-3.2	-2.4	-0.2	3	4.8	2.7	11
AOK115	-1.1	-0.3	1.6	3.6	4.6	1.95	11
AOK111	-3.4	-2.9	-1	2.6	4.2	2.75	11
Section IIb							
AOK169	-3.6	-2.9	-1.6	-0.2	0.8	1.35	12.3
AOK170	-3.4	-2.7	-1.3	0.5	2	1.6	14.4
AOK177	-2.9	-2.1	-0.8	0.8	2.7	1.45	19.7
AOK175	0.6	1.2	2.8	4.2	5.5	1.5	23.7
Section IIIa – upper unit							
AOK143	-3.4	-2.8	-1.7	-0.5	0.7	1.15	19.9
AOK146	-2.9	-2.2	-1.4	-0.5	0.3	0.85	26
AOK151	-2.3	-1.8	-1	-0.2	0.2	0.8	32.6
AOK149	-2.3	-1.8	-1	-0.2	0.1	0.8	33.2
AOK153	-1.9	-1.2	-0.5	0.4	0.6	0.8	40.3
Section IIIb – upper unit							
AOK142	-3.8	-3.1	-2.1	-1	-0.2	1.05	21.5
AOK189	-3.2	-2.8	-1.8	-0.9	-0.2	0.95	25.7
Section IIIc – basal unit							
AOK144	-2.9	-2.2	-0.9	1.7	3.5	1.95	19.9
AOK145	-2.9	-2.1	-1	1.7	3.5	1.9	22
AOK147	-2.1	-1	0.2	1.3	2	1.15	26
Section IIId – basal unit							
AOK150	-2.4	-1.5	-0.7	0.3	2.7	0.9	36.8
AOK154	-1.2	-0.4	0.6	1.5	2.5	0.95	43.1
Tsunami unit							
AOK187	-1.9	-1.3	0.1	1.3	2.3	1.3	25.7
AOK188	-0.9	-0.4	0.5	1.3	2.3	0.85	25.7

Discussion

Eruption dynamics

The thick soil underlying the fall deposits suggests that the 2050 BP Okmok II eruption occurred after a multiyear period of quiescence because soil formation is slow in Arctic regions like the Aleutians Islands (J. Beget, pers. comm. 2000). Both the charred vegetation in its living position within the fall unit A1 and the preservation of the reverse grading of this unit suggest that the ground was mostly free of snow at the time of the eruption. The eruption started as an increasingly vigorous Plinian column of rhyodacitic fall tephra, the umbrella of which was diverted to the NNW by strong winds. The distribution map of the associated fall deposits shows that the vent was located in the northern part of the caldera. After a second steady pulse that produced unit A2, the column faded and the eruption stopped as indicated by the small amount of reworking between fall sequences A and B. Interruption of the eruptive activity was long enough to gently rework the fresh deposit, but not sufficient to develop significant water drainage, suggesting an interval of days to months.

The second part of the eruption started from a vent located in the eastern part of the caldera with the wind blowing to the east. Unfortunately, the distribution map of the associated fall deposits is not sufficient to indicate whether the various fall sequences originate from one or several source vents. High proportions of glassy and blocky clasts, the internal discontinuous layering of the deposit, and the likely presence of abundant water within the caldera left by Okmok I, suggest that unsteady phreatomagmatic explosions generated these deposits. As the explosive venting suddenly changed composition from dacitic to andesitic, fewer phreatomagmatic events occurred, but the wind continued to blow eastward. Interestingly, the drastic compositional shift from rhyodacite to basaltic andesite occurred without noticeable changes in eruptive style or vent location. The presence of a short phreatomagmatic dacitic event is noted within the sequence C (pumice-bearing unit C2). After expelling up to 0.5 km^3 of dacite (~0.25 km^3 DRE) and 0.35 km^3 of andesite (~0.17 km^3 DRE), the eruptive regime dramatically increased, three orders of magnitude in volume, and generated deposits that completely covered the northeast part of Umnak Island. Most likely, the pyroclastic current deposits are responsible for the charred vegetation buried underneath the fall deposits because the fall deposits were not hot enough to char vegetation when they were deposited (Thomas and Sparks 1992). The pyroclastic deposits, however, were not hot enough to cause welding or scoria oxidation, which suggests that their temperature was between 200 and 600 °C (Riehle 1973).

The climactic phase expelled about 50 km^3 (~29 km^3 DRE) of material, half of which was deposited on Umnak as a massive facies, and a fraction of which was deposited as a stratified facies on Unalaska and some hills of Umnak. The dramatic increase in both eruptive strength and lithic content suggests a temporal link between the emplacement of these deposits and the initiation of caldera collapse. Unfortunately, the style of caldera collapse cannot be inferred from the present sedimentological study because the characteristics of the massive facies have similar trends regardless of azimuth despite its variable thickness. The wavy nature of the bottom contact and the flat surface defined by its top (Fig. 7a) indicate that the massive facies filled in previous topography, which was probably a rugged plateau with deeply incised gullies. The poor sorting, massive appearance, and distribution of the massive facies suggest that it formed by deposition from a dense, ground-hugging pyroclastic flow (Sparks 1976; Druitt 1998; Freundt et al. 2000). The valley-ponding deposition probably favored larger variations in grain sizes at the base of the deposits. Crude stratifications where the topography is rugged probably result from the interlacing of multiple lobes within the moving pyroclastic flow. Along the same line, the weak coarse-tail grading is also probably caused by variations of the local conditions of sedimentation. Overall, grain size analyses suggest that the spreading of the pyroclastic flow was axisymmetric, which is helpful to address the emplacement dynamics of the current, because it allows direct comparison of locations equidistant from the caldera rim.

Although one might think that such a large pyroclastic flow would significantly erode a rugged topography, evidence of erosion is scarce: the only erosive base was found at the proximal eastern locality AOK138 (Fig. 1). In addition, the high aphyric basalt content of the base at location AOK124 (Fig. 9) is probably derived from the nearby north-trending ridge, where outcrops of the same basalt abound. This indirect evidence suggests that the current eroded part of the northward ridge along section Ia, directly north of the caldera (Fig. 1).

Less than 0.2% of the volume of the density current deposits is stratified. Nevertheless, the correct interpretation of the topology of this scarce facies is essential to understand the parent density current. The bedding pattern and the variable distribution of this facies suggest that it formed by deposition from dilute, turbulent pyroclastic surge(s) (Fisher 1965; Valentine and Fisher 2000).

The distribution of the stratified facies to paleohighs and the massive facies within depressions suggest that they can be characterized as over-bank and paleovalley facies (Schumacher and Schmincke 1990). In this view, scoria accumulations at the facies transition are likely remnants of pumice levees, and their presence where the massive facies thins out suggests that the paleorelief was not high enough at these locations to cause the deposition of

the stratified facies. The fact that the stratified facies is a lateral variation of the massive facies implies their simultaneous deposition. The synchronous and axisymmetric nature of the deposits favors the interpretation that Okmok II deposits have been produced by a single density current. The apparent contradiction of coexisting pyroclastic flow and surge within the same current can best be explained by a segregated pyroclastic density current. In this hypothesis, the current consists of a highly concentrated base that produces massive deposits and an overriding dilute cloud that sediments stratified deposits preferentially on hills (Fisher 1965; Denlinger 1987; Valentine, 1987; Fisher 1990; Baer et al. 1997; Burgisser and Bergantz 2002).

Interactions of the density current with topography

To the southwest of Hourglass Pass (Fig. 1), the pyroclastic density current traveled over successive ridges, leaving both stratified and massive facies in the small valleys that separate these ridges. The pumice levee situated on a hill four kilometers before the first ridge (AOK100, Fig. 1) indicates that the transition between dense flow and dilute cloud was at 70 m above the lowlands before the ridge. Considering that similar transitions exist between the other massive and stratified outcrops, one can infer that the dense part was less than 100 m thick after the first ridge, and about 20 m thick after the second ridge. The first and second ridges are ~120 and ~130 m high, respectively. How can the dense part overcome ridges thicker than the current itself? Woods et al. (1998) proposed that gravity current could overcome obstacles higher than itself by the upstream current filling up the height difference. Such a process is predicted to significantly reduce the thickness of the deposit after the crossing, but would not affect the transport capacities of the current (Bursik and Woods 2001). On the other hand, if the basal part had enough momentum, it could overcome the ridge while maintaining a supercritical regime. The sudden loss of momentum would then enhance sedimentation at the ridge, and one would expect the thickening of the deposit accompanied by decrease in grain size just before or just after the ridge. At Okmok. drastic thickness reduction of the massive deposit across the second ridge (from >19 m to 1.5 m) is consistent with both partial blocking and excess momentum with thickening before the ridge. Similar measurements are unfortunately not possible across the first ridge because the base of the deposit is buried on both sides. However, the evolution of the grain size and the componentry across both ridges is identical to that of an unobstructed pathway, which is inconsistent with an excess momentum (section Ic, Fig. 11 and section IIa, Fig. 14b). Thus, the massive deposit most likely results from partial blocking and filling-up of the dense part across the ridges (Woods et al. 1998).

The stratified facies does not noticeably vary in thickness, grain size, or componentry across the three first ridges, when compared to an unobstructed pathway (section IIIa, Fig. 15a and section IIb, Fig. 14b). This invariance suggests that the three first ridges did not affect the dilute part of the density current, most likely because the current was much thicker than the ridges. The fourth ridge, however, caused significant decrease in thickness and grain size with enrichment in glass and crystal. A sudden thinning of the cloud because of partial blocking could cause such a change, but would not affect componentry. Most likely, the thick dilute current became buoyant at that point, preferentially entraining light scoria while lifting off.

The above data help in reconstructing a likely scenario of emplacement (Fig. 19). The match in size distribution between stratified deposits and the coarser part of the associated dense deposits (Fig. 14c) is consistent with the dense and dilute parts being in dynamic equilibrium and constantly exchanging particles with each other before decoupling at the first ridge (Fisher 1995). After being blocked at the first ridge, the basal part thickened until it was crossed. The process repeated at the second ridge, but the upstream flux was not sufficient for the dense part to cross the third ridge. Meanwhile, the dilute part decoupled from the blocked part and successfully crossed the four ridges. After the fourth ridge, the decoupled cloud became dilute enough to buoyantly lift off.

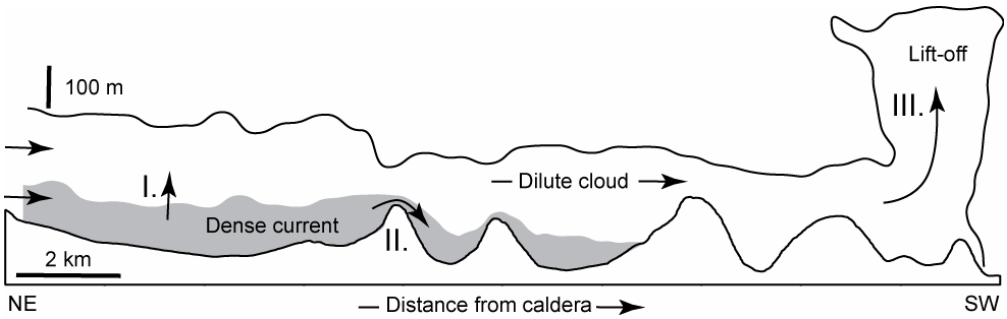

Figure 19 Schematic evolution of the pyroclastic density current across the four ridges of section IIb. At first blocked by the first ridge, the basal part thickened (I.) until it could overcome the two first ridges (II.). The upstream flux, however, was insufficient for the basal part to cross the third ridge. Meanwhile, the dilute part decoupled and overtook the dense part to successfully cross four ridges, which caused its speed to decrease. The slowed-down cloud buoyantly lifted-off when encountering the more massive relief after the fourth ridge (III.), most likely because the previous partial blockings significantly unloaded the cloud. Deposit thickness not to scale, and see Fig. 1 for section location.

Travel of the density current over water

The entrance of a pyroclastic current into the water has been reviewed by Cas and Wright (1991) and possible scenarios abound (e.g., Legros and Druitt 2000). Yet, cases similar to Okmok, where currents traveled over water and deposited analyzable deposits on a distant shore are notably infrequent (Suzuki-Kamata 1988; Fisher et al. 1993; Carey et al. 1996; Allen and Cas 2001).

The most striking difference between deposits on Umnak and the ones on Unalaska is the complete absence of massive facies on the latter island. The facies transition localized on the south side of Idak plateau (Fig. 13) suggests that the dense part of the pyroclastic current was ~120 m thick when it reached the east coast of Umnak. Crossing of Umnak Pass strait thus decoupled the two parts of the density current, and the dense part dove into the waters. Geologic cases of dense flows diving into the sea are multiple, such as the Roseau (Carey and Sigurdsson 1980), the Grande Savanne (Sparks et al. 1980), and the Krakatau 1883 (Mandeville et al 1996) ignimbrites. Unfortunately, at Okmok, the undisturbed nature of the massive facies at shore and the lack of underwater sampling limit the investigations on the interactions between hot pyroclasts and seawater (e.g., Sigurdsson and Carey 1989). Most of the mass of the Okmok pyroclastic current did not cross Umnak Pass, unlike the Ito pyroclastic flow, which ran across a shallow lake of several tens of kilometers without leaving deposits at the bottom of the lake (Baer et al. 1997), or the Campanian ignimbrite, which traveled over water to produce thick deposits across the 35-km-wide Bay of Naples (Fisher et al. 1993).

Whether the crossing affected the dilute cloud can be assessed by comparing the stratified facies between the two islands. Within the variability in grain size inherent to stratified facies, the sorting of the basal, crudely stratified deposit on Unalaska matches that of individual layers found on Umnak (Fig. 20a). This and stratigraphic correlations suggest that the basal unit on Unalaska is the lateral equivalent of the products of the dilute cloud on Umnak. Component analysis of this unit, however, indicates that it is very lithic poor (Fig. 20b). This componentry remains similar over the whole island (Fig. 15b), suggesting that the sorting occurred at sea. Preferential loss of dense lithics during transport across water has also been reported for the Krakatau 1883 ignimbrite (Carey et al., 1996), and the Kos Plateau Tuff (Allen and Cas 2001). Freundt (2003) demonstrated this density-selective process with flume experiments simulating the entrance of pyroclastic currents into the sea. The key idea is that once lithics touch the surface of the water, they immediately sink; lithics are thus removed from the dilute current, whereas the low density of the scoria ensures their preservation within the transport system. Following this reasoning, the high lithic content of the upper layer

becomes problematic. How to preserve lithics within the cloud across the 8-km strait? The answer is probably linked to pumice rafts, which are large accumulations of low-density clasts on the sea surface generated by fallout or pyroclastic currents traveling over water (Whitham and Sparks 1986). Because densities and porosities of pumice and scoria have similar ranges, both pumice and scoria rafts share similar floatation properties (Gardner et al. 1996). If the scoria rafts produced by Okmok's eruption became continuous and thick enough, they could act as a skin over the water, bouncing dense clasts as the ground would. In other words, artificial enhancement of the water surface tension could preserve lithics within the traveling current, thus allowing a lithic-bearing layer of pyroclasts to sediment over Unalaska. Note that the lithic-rich layer irregularly found at the base of both facies on Umnak Island is absent on Unalaska Island, as it cannot be correlated to the upper layer on Unalaska. Its absence after crossing the water is consistent with decreases in lithic size observed in similar lithic-rich ground layers of the Taupo ignimbrite (Wilson 1985) and the Ata pyroclastic deposits (Suzuki-Kamata 1988) after those currents crossed water. Interestingly, both layers on Unalaska are enriched in large (~1 ϕ) crystals in the coastal sections (e.g., Fig. 20b). Unfortunately, no satisfactory explanation for this local enrichment (or depletion in fine scoria) has been found.

The fine sand units with erosive contact atop stratified deposits are linked with the entrance of the density current into Umnak Pass (Fig. 18). The peculiar location of this deposit, higher than the mean high tide (the modern range of maximum tide is 1.2 m at Chernofski Harbor, near AOK150, Fig. 1) but below 15 m, and its stratigraphic characteristics suggest it was produced by a tsunami generated by the density current. The increase in lithic content of these sands also suggests water transport because hydraulic sorting is detrimental to scoria deposition but favorable to denser clasts deposition. In this view, the partially eroded basal unit likely represents flooding and the thick bimodal unit atop correspond to tsunami backwash. The partial preservation of the lower stratified pyroclastic unit (AOK189) indicates that the tsunami wave(s) occurred after the dilute current.

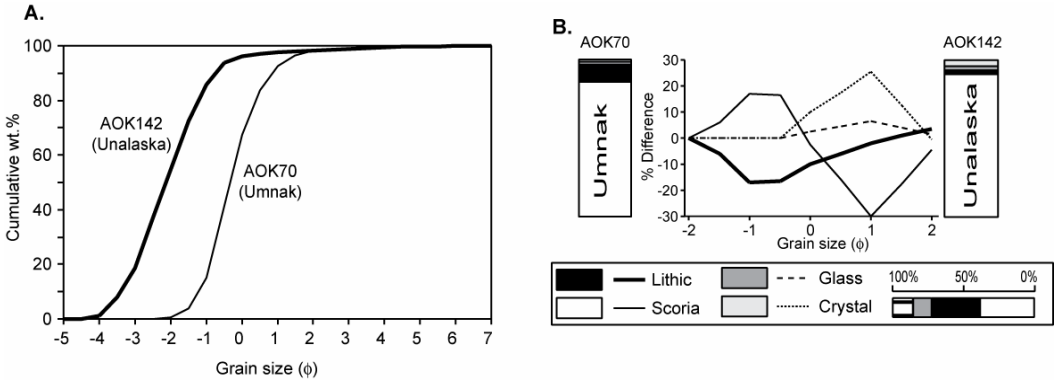

Figure 20 Grain size and component variations of the stratified facies across Umnak Pass. See Fig. 1 for samples location. **a.** Grain size distribution. Note the similar sorting between the two samples. **b.** Component variations with grain size. Component data at each grain size of samples to the left of the diagram is subtracted from the comparative size class of samples to the right.

The highest locality on the plateau of Unalaska (349 m, AOK145, Fig. 1) consists of only the upper stratified unit, which indicates that the current responsible for the basal unit was less than 300 m thick, and that a thicker current deposited the upper unit. The sharp decrease in grain size between the low sites on the coast of Unalaska (section IIIa) and the high plateau (section IIIb) suggests that the 100-m sea cliff acted as a significant topographic barrier to the dilute current, which is consistent with a 300-m estimate. Two possible explanations can be put forward for the curious bimodality displayed by the near-shore upper unit samples (Fig. 16). First, this localized fines increase could result from short-lived aggregates formed either by electrostatic forces or by excessive moisture in the dilute cloud (e.g., ch. 16 in Sparks et al. 1997). Second, it could result from local steam explosions at the sea interface (e.g., Freundt 2003).

Similar contrasting behaviors of dense and dilute flows encountering seawater have also been reported in the literature. In the 1883 Krakatau eruption, one of the best studied examples, dense parts of the flow left hot massive deposits on the subhorizontal seafloor surrounding the caldera, while hot dilute parts of the flow traveled tens of kilometers over the sea (Carey et al. 1996; Mandeville et al. 1994; Mandeville et al. 1996). During the 1902 eruptions of Mt Pelée, pyroclastic currents entered the sea and their dense part broke telegraph cables nearly 20 km offshore, while associated dilute clouds ran out into the harbor and set fire to anchored ships (Lacroix 1904). In the on-going eruption of Montserrat, basal flows were witnessed to enter the sea and generated a zone of intense boiling, while the overriding ash cloud passed over the surface (Cole et al. 1998).

Estimates of dynamic parameters from density current deposit data

The angular nature of the scoria found in the stratified deposit suggests that clast rolling played a negligible role during sedimentation, and the good sorting of most bulk samples ($\sigma \sim 1$) implies deposition occurred either rapidly or steadily. On Unalaska, the absence of over-thickening of the stratified facies in depressions and troughs suggest no significant downhill drainage of the depositional system (cf. Fisher 1990) occurred. These observations are best explained if the current bears a weakly developed sedimentation system, with deposition mainly occurring by suspended load fallout. It is possible to retrieve dynamic variables from deposits of such a dilute cloud with the kinematic template proposed by Burgisser and Bergantz (2002).

Following Burgisser and Bergantz (2002), we assume that, at a given location, the dilute cloud is most likely to sediment particles that decouple from motions due to turbulence. Such particles transiently gather within the current, and their characteristics can be tracked by looking at Σ_T near unity and S_T at unity (Equs. 1 and 3, see *Methods and theory*). The weak skewness of the size distributions guided the choice that the median size of the deposit matches $\Sigma_T = 1$, and that the condition $S_T = 1$ lies within 90% of the size distribution. Thus, a value of U_{rms} from Σ_T and a range of δ_i from S_T can be calculated for each location. It should be kept in mind that speeds given therein are not absolute because of the lack of experimental support of this theory, but they are believed to define meaningful trends.

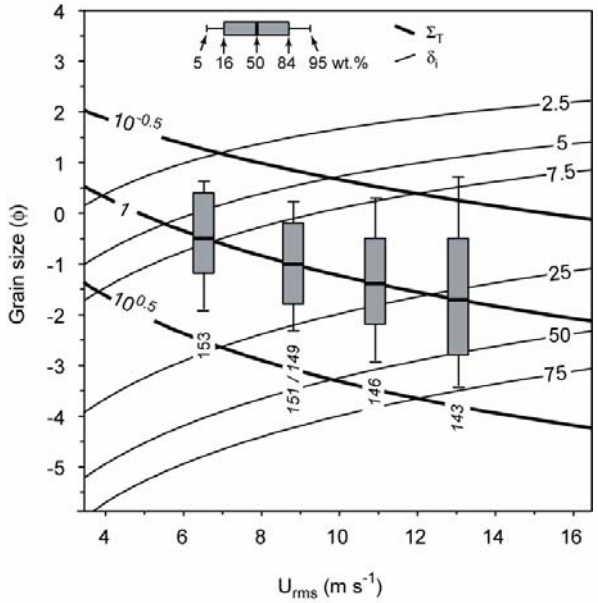

Figure 21 Example of reverse modeling of field data using a U_{rms} vs. grain size plot. Samples are from the section IIIa (see text). Thick lines are values of Σ_T, thin lines are eddy maximum size δ_i, and boxes represent grain size distributions. Variables used are $\mu = 1.5 \times 10^{-5}$ Pa s, $\upsilon = 3 \times 10^{-5}$ m^2 s^{-1} (air at 300 °C), and ρ_p = 1150 kg m^{-3}. For completeness, AOK153 is also shown on this plot although its density is 1250 kg m^{-3}. If accounted for, this difference of +100 kg m^{-3} would shift the curves towards smaller grain sizes by ~0.1 ϕ.

To illustrate this inverse modeling, below is the retrieval of the dynamic parameters of the current that traveled across Unalaska plateau (section IIIa in Fig. 1). Using the mean particle density obtained from bulk component data (1150 kg m^{-3}, Fig. 15c) and Equs. 1-4, the size distribution can be plotted against U_{rms} (Fig. 21). The median grain size (50 wt.%) of each sample is then matched at Σ_T=1 and the size distribution is represented by a box that indicates 5, 16, 50, 84, and 95 wt.%. This match gives a value of U_{rms} for each sample, from which the mean current speed is calculated with Equ. 2 (Table 2, see also section IIIa in Fig. 22). On the obtained graph are three curves for key values of Σ_T ($10^{-0.5}$, 1, and $10^{0.5}$) and six curves for S_T =1, which correspond to various values of the maximum eddy size δ_i. The 5 and 95 wt.% marks of each distribution give upper and lower limits for δ_i, from which Froude numbers are calculated (Equ. 4, Table 2).

Table 2 Dynamic parameters for the stratified facies.

sample	ρ avg (kg m^{-3})	U_{rms} (m s^{-1})	δ_i (m)	mean speed U (m s^{-1})	current height H (m)	F_R
Idak plateau						
AOK64	1950	15	5-300	60	200-300	<0.25
AOK69	1350	1.5	0.01-2.5	6	200-300	<0.01
AOK70	1250	6	2.5-10	24	200-300	<0.03
Kettle Cape – basal unit						
AOK117	2050	15.5	5-300	62	>100	<0.75
AOK114	1950	9.5	0.75-75	38	>100	<0.19
Kettle Cape – upper unit						
AOK116	1750	7	0.1-50	28	>100	<0.13
AOK115	1450	2	0.01-5	8	>100	<0.01
AOK111	1250	9	0.1-50	36	>100	<0.13
Section IIb						
AOK169	1150	12.5	5-75	50	>200	<0.09
AOK170	1150	10.5	2.5-50	42	>200	<0.06
AOK177	1450	9	1-50	36	>200	<0.06
AOK175	1450	0.5	0.01-0.5	2	>200	<0.01
Section IIIa – basal unit						
AOK143	1150	13	7.5-75	52	75-200	<0.25
AOK146	1150	11	7.5-50	44	100-200	<0.13
AOK151	1150	9	5-25	36	50-200	<0.13
AOK149	1150	9	5-25	36	50-200	<0.13
AOK153	1250	6.5	2.5-25	26	50-200	<0.13
Section IIIb – basal unit						
AOK142	1150	16	10-100	64	150-300	<0.17
AOK189	1150	13.5	10-75	54	150-300	<0.13
Section IIIc – upper unit						
AOK144	1650	10	7.5-50	40	>300	<0.04
AOK145	1350	9.5	2.5-50	38	>50	<0.25
AOK147	1250	6	0.75-10	24	>100	<0.03
Section IIId – upper unit						
AOK150	1250	8	0.75-25	32	>200	<0.03
AOK154	1550	4	0.5-7.5	16	>50	<0.04

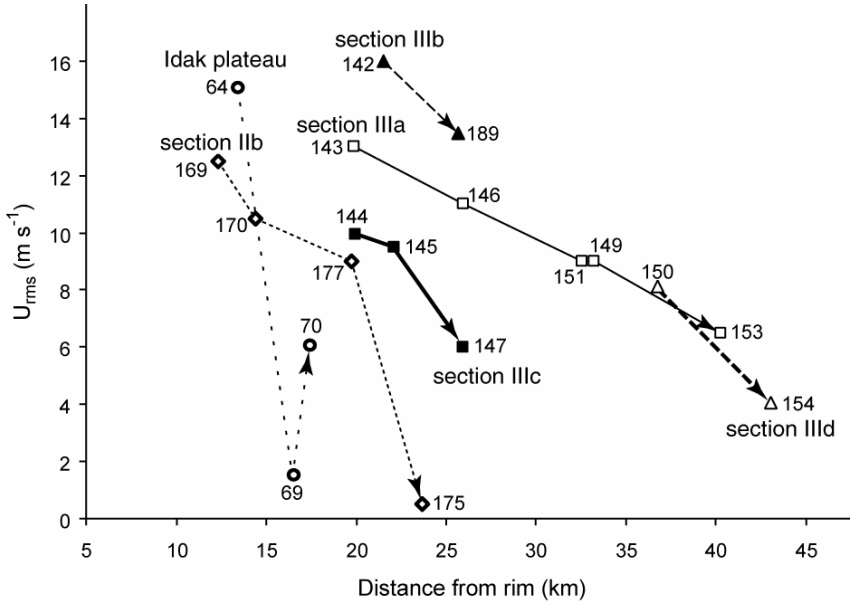

Figure 22 Root-mean square velocities U_{rms} of the dilute pyroclastic current for various sections around Okmok. Arrows indicate the current direction and labels are sample numbers (Fig. 1 for section locations).

Dynamics of proximal deposition

Reverse modeling of the stratified deposits on Idak plateau indicates that speed sharply decreases from the northern edge inwards (Fig. 22). No significant obstacle, however, could explain such a deceleration. The shape of the plateau and the high variability in thickness and grain size of the related stratified deposits suggest that the plateau acted as an obstacle, forcing the density current to flow around it. The peak at the southwest tip thus sheltered the rest of the plateau and its altitude gives an upper boundary to the current thickness. Using stratigraphic constraints (Fig. 13A), the density current was thus ~300 m thick near Idak plateau with most of its mass concentrated in the bottom third. Deposits recorded the cross-stream motions of the dilute cloud overflowing on the plateau, which were small (6 to 24 m s^{-1}, Table 2) compared to 60 m s^{-1} along-stream at the plateau edge (AOK64 in Table 2).

The paucity of data limits the interpretation of the inter-layer variations within the stratified deposit because only deposits at Kettle Cape contain abundant crossed and planar bedding. Data from this locality simply suggest that the basal lithic-rich unit was deposited by a more energetic current/pulse than the upper scoria-rich unit (Table 2). A similar basal unit has been described at Unzen, where it is thought to originate from the interface between the dense and dilute parts of the current (Fujii and Nakada 1999).

The average speed of the pyroclastic density current and the volume of inland deposits can provide an upper estimate of the magma discharge rate. Assuming that speed estimates near the shore (~60 m s^{-1}; Table 2) are representative of the average current velocity, the 24 km^3 of inland deposits took at least 250 s to sediment. Using 1450 kg m^{-3} for average density gives a maximum discharge rate $<1.4\times10^{11}$ kg s^{-1} for the climactic phase of the Okmok II eruption. Of course, the real value is expected to be much lower because sedimentation is unlikely to be instantaneous.

Dynamics of distal decoupling

The distal, decoupled behavior of the current can be constrained by its interactions with the sea. The velocity of the current across Unalaska plateau decreases linearly over more than 20 km (section IIIa, Fig. 22). Compared to localities near the shore, this remarkably regular trend is shifted towards lower speeds (section IIIb, Fig. 22). It is thus likely that the cliffs that fringe Unalaska plateau abruptly decelerated the current. The range of buoyancy frequencies given by S_T and estimates of the current thickness maximize the Froude number at 0.25 at the coast

(Table 2). The height ratio between the cliff and the current is 0.3 to 0.5. The current was thus subcritical with a modest height ratio, which suggests that cliffs blocked a significant portion (up to 100 m) of the dilute current (Baines 1995). On the plateau, the current slowed down to about 40 m s^{-1} and remained subcritical with $F_R < 0.1$ (Fig. 23b). Both the deceleration and the abrupt thinning of the deposit between the coast and the plateau are consistent with an enhanced sedimentation caused by partial blocking. Reverse modeling of the upper layer indicates a similar steep decrease in speed at the edge of Unalaska plateau (sections IIIc-d, Fig. 22). The elevated localities bearing the upper unit suggest that the associated dilute cloud was thicker than 300 m. Thus, the current that deposited the upper unit was also subcritical (Table 2), but thicker and slower than its predecessor (Fig. 23c).

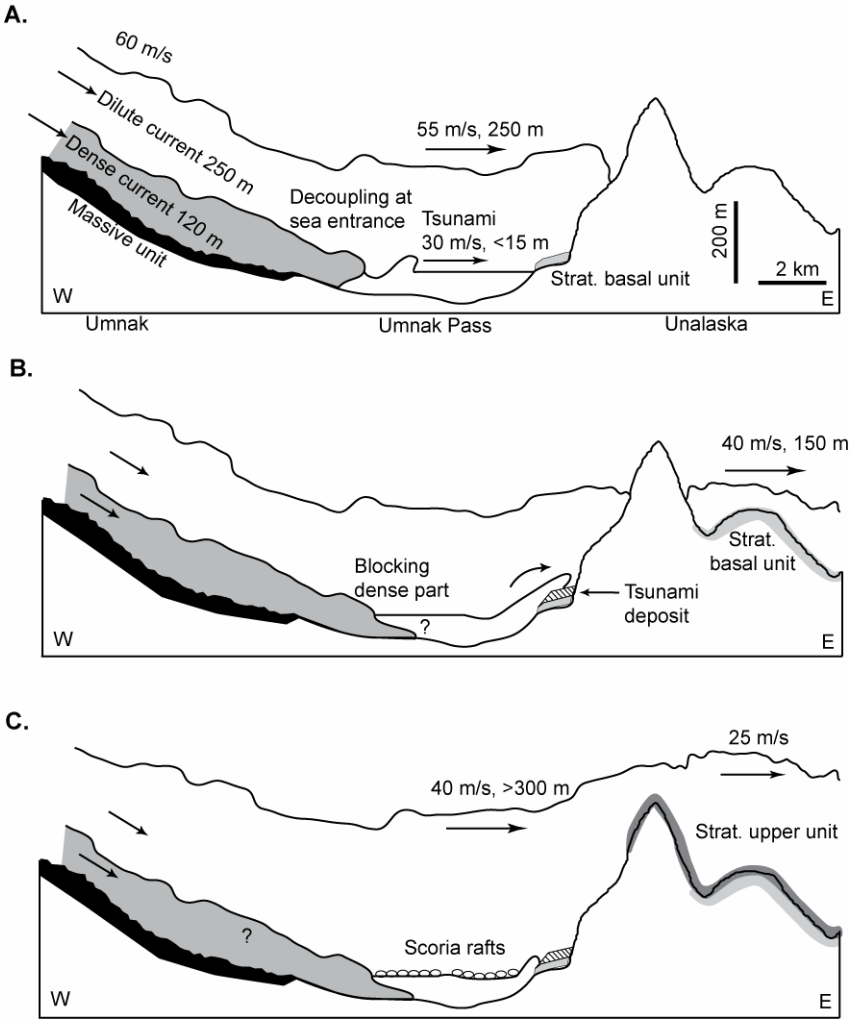

Figure 23 Schematic evolution of the pyroclastic density current crossing Umnak Pass. **a.** The dilute cloud, decoupled from the dense part at sea entrance, reached Unalaska before the tsunami caused by the entrance of the dense part into the sea. **b.** Partial blocking of the dilute cloud by sea cliffs at Unalaska and emplacement of the tsunami deposits on the shore of Unalaska. **c.** The second dilute cloud to reach Unalaska was thicker and enriched in lithics, presumably because of extensive scoria rafts floating on Umnak Pass.

How fast was the tsunami that reached Unalaska coast (Fig. 23a)? Tsunami wave motion is commonly treated with the shallow-water approximation, and the short travel across the strait can be best described with a solitary wave (Watts and Waythomas 2003). The solitary wave speed U_W is expressed as a function of the water depth D and the wave amplitude A (e.g., ch. 7 in Kundu 1990):

$$U_W = \sqrt{gD}\left(1 + \frac{A}{2D}\right) \qquad (5)$$

Umnak strait averages 50 m depth, with a maximum of 100 m, and the wave amplitude reached 15 m. The tsunami thus traveled across the strait at speeds between 25 and 34 m s^{-1}, which is, as expected from stratigraphic evidence, slower than the 54 m s^{-1} estimate for the dilute cloud (Table 2).

Interactions of the current with hills are another effective way to constrain decoupled behavior. Using the evolution of the current speed over the relatively smooth plateau on Unalaska as a reference, calculations indicate that the dilute current lost speed in a stepwise fashion while crossing the southwestern ridges (section IIb, Fig. 22). Importantly, this stepwise deceleration was not apparent from the grain size distribution data alone. The speed step across the second ridge has a comparable magnitude to that caused by the sea cliff on Unalaska, whereas the speed decrease across the third ridge is modest. The current abruptly reached a low value of U_{rms} after the fourth ridge, which is consistent with the transition from horizontal motion to vertical lift-off. The current was always subcritical because F_R was below 0.09 at all localities (Table 2), and thus likely to be partially blocked by each successive ridge. These blockings most likely increased sedimentation within the current in a way similar to that on the west coast of Unalaska and this unloading helped to trigger the lift-off.

Conclusions

Geological and sedimentological data helped to reconstruct the dynamics of the Okmok II caldera-forming eruption. After a significant period of quiescence, the 2050 ± 50 BP volcanic episode started with an increasingly vigorous Plinian column of rhyodacite, the umbrella cloud of which was diverted by strong SSE winds. After a second steady pulse, the column faded and the eruption stopped for a period of days to months. Eruptive activity resumed with unsteady phreatomagmatic explosions under strong westerly winds. As the explosive venting became more magmatic, the composition suddenly changed from rhyodacitic to andesitic. After expelling up to 0.25 km^3 DRE of rhyodacite and up to 0.17 km^3 DRE of andesite, the eruptive regime increased dramatically because of caldera collapse to generate ~29 km^3 DRE of pyroclastic density current deposits that completely covered the northeast part of Umnak Island.

Field evidences suggest that a single density current segregated into a highly concentrated base and an overriding dilute cloud and produced the Okmok II deposits. While the basal part produced massive deposits, the dilute cloud preferentially sedimented stratified deposits on hills. Topographic barriers made by four successive ridges on the southwest of the caldera reveal the dynamic behavior of these two parts. At first blocked by a first ridge, the basal part thickened until it could overcome it. The same process occurred over the next ridge, but the upstream flux was insufficient for the basal part to cross the third ridge. Meanwhile, the dilute part decoupled and overtook the dense part to successfully cross the four ridges. This dilute cloud, however, was subcritical and the successive ridges caused its speed to decrease in a step-wise fashion. The slowed-down cloud buoyantly lifted-off when encountering more massive relief after the fourth ridge, most likely because the partial blockings had significantly unloaded the cloud by increasing sedimentation.

When reaching the east coast of Umnak, the density current was about 300 m thick with a ~120-m dense basal part that concentrated most of its mass. Crossing the 8-km wide strait between Umnak and Unalaska Islands decoupled the two parts of the current. While the dense part dove into the sea, the dilute cloud traveled over the water, preferentially losing dense lithics it transported. On the other side of the strait, cliffs fringing Unalaska plateau decelerated abruptly the dilute, 200-m thick, subcritical current and blocked its bottom half, thereby enhancing sedimentation at shore. The slowed-down current continued its course on the plateau of Unalaska Island, gently decelerating for the next 20 km. Near the end of the eruption, the dilute current thickened to >300 m, slowed down, and deposited a unit enriched in lithics on Unalaska. Lithics were preserved during this late stage most likely because of extensive scoria rafts covering the strait between the two islands.

Pyroclastic density current decoupling can be triggered by both sea entrance and topography interaction. While seawater tends to absorb the dense part of the current and the lithics transported by the dilute cloud, topographical relief noticeably decelerates both parts of the current and favors sedimentation by partial or complete blocking. In the case of subcritical, dilute currents, the resulting unloading may drastically reduce the runout distance by triggering a buoyant lift-off.

Acknowledgments

This manuscript presents research done as part of my Ph.D. thesis at the University of Alaska Fairbanks. Many thanks to S. Applegate, B. Browne, and K. Papp for performing the ungrateful task of field assistant, and P.J. Shamberger for helping me with the sieving. Many thanks also to J. Eichelberger for proposing and supporting the fieldwork, thus allowing the field assistants and myself to enjoy the sheer beauty of the Aleutian Islands. Field discussions with J. Larsen, T. Miller, J. Beget, and C. Waythomas proved extremely useful. Reviews by C. Mandeville and an anonymous reviewer greatly helped to improve the structure and the quality of the manuscript. Funding was provided by the Volcano Hazards Program of the US Geological Survey, through the Alaska Volcano Observatory.

References

Allen SR, Cas RAF (2001) Transport of pyroclastic flows across the sea during the explosive, rhyolitic eruption of the Kos Plateau Tuff, Greece, Bull. Volcanol. 62:441-456.

Baer EM, Fisher RV, Fuller M, Valentine G (1997) Turbulent transport and deposition of the Ito pyroclastic flow: determinations using anisotropy of magnetic susceptibility, J. Geophys. Res. 102:22565-22586.

Baines PG (1995) Topographic Effects in Stratified Flows, Cambridge University Press, 482 p.

Black RF (1975) Late quaternary geomorphic processes: Effects on the ancient Aleuts of Umnak Island in the Aleutians, Arctic 28:159-169.

Burgisser A, Bergantz GW (2002) Reconciling pyroclastic flow and surge: the multiphase physics of pyroclastic density currents, Earth Planet. Sci. Lett. 202:405-418.

Bursik MI, Woods AW (2001) The effect of topography on sedimentation from particle-laden turbulent density currents, J. Sediment. Res. 70:53-63.

Byers FM (1959) Geology of Umnak and Bogoslov Islands, Aleutian Island, Alaska, U.S. Geol. Surv. Bull. 1028-L:107-367

Byers FM Jr (1961) Petrology of three volcanic suites, Umnak and Bogoslov Islands, Aleutian Islands, Alaska, Bull. Geol. Soc. Am. 72:93-128.

Carey SN, Sigurdsson H (1980) The Roseau Ash: deep-sea tephra deposits from a major eruption on Dominica, Lesser Antilles Arc, J. Volcanol. Geotherm. Res. 7:67-86.

Carey S, Sigurdsson H, Mandeville C, Bronto S (1996) Pyroclastic flows and surges over water: an example from the 1883 Krakatau eruption, Bull. Volcanol. 57:493-511.

Cas RAF, Wright JV (1987) Volcanic Successions: Modern and Ancient, Allen & Unwin, London, 528 p.

Cas RAF, Wright JV (1991) Subaqueous pyroclastic flows and ignimbrites: an assessment, Bull. Volcanol. 53:357-380.

Cole PD, Calder ES, Druitt TH, Hoblitt R, Robertson R, Sparks RSJ, Young SR (1998) Pyroclastic flows generated by gravitational instability of the 1996-97 lava dome of Soufriere Hills Volcano, Monserrat, Geophys. Res. Lett. 25:3425-3428.

Denlinger RP (1987) A model for generation of ash clouds by pyroclastic flows, with application to the 1980 eruptions at Mount St. Helens, Washington, J. Geophys. Res. 92:10284-10298.

Druitt TH (1998) Pyroclastic density currents, *in*: Gilbert JS, Sparks RSJ (eds), The physics of explosive volcanic eruptions, Geol. Soc. Spec. Publ., London 145:145-182.

Fisher RV (1965) Mechanism of deposition from pyroclastic flows, Am. J. Sci. 264:350-363.

Fisher RV (1990) Transport and deposition of a pyroclastic surge across an area of high relief: The 18 May 1980 eruption of Mount St. Helens, Washington, Geol. Soc. Am. Bull. 102:1038-1054.

Fisher RV (1995) Decoupling of pyroclastic currents: hazards assessments, J. Volcanol. Geotherm. Res. 66:257-263.

Fisher RV, Orsi G, Ort M, Heiken G (1993) Mobility of a large-volume pyroclastic flow - emplacement of the Campanian ignimbrite, Italy, J. Volcanol. Geotherm. Res. 56:205-220.

Freundt A (2003) Entrance of pyroclastic flow into the sea: experimental observation, Bull. Volcanol. 65:144-164.

Freundt A, Wilson CJN, Carey SN (2000) Ignimbrite and block-and-ash flow deposits, *in*: Sigurdsson H (ed) Encyclopedia of Volcanoes, Academic Press, 581-599.

Fujii T, Nakada S (1999) The 15 September 1991 pyroclastic flows at Unzen Volcano (Japan): a flow model for associated ash-cloud surges, J. Volcanol. Geotherm. Res. 89:159-172.

Gardner JE, Thomas RME, Jaupart C, Tait S (1996) Fragmentation of magma during Plinian volcanic eruptions, Bull. Volcanol. 58:144-162.

Inman, DL (1952) Measures for describing the size distribution of sediments, J. Sed. Petrol. 22:125-145.

Kay SM., Kay RW (1994) Aleutian magmas in space and time *in*: Plafker G, Berg HC (eds.) The Geology of Alaska, Boulder CO, Geol. Soc. Amer., The Geology of North America, G-1:687-722.

Kundu PK (1990) Fluid mechanics, Academic Press, 638 p.

Lacroix A (1904) La Montagne Pelée et ses éruptions, Masson, Paris, 662 p.

Larsen JF, Nye, C (2003) Petrology and geochemistry of the 2050 yBP Okmok caldera-forming eruption: Origin of the voluminous basaltic-andesite pyroclastic deposits, Bull. Volcanol. in review.

Legros F, Druitt TH (2000) On the emplacement of ignimbrite in shallow-marine environments, J. Volcanol. Geotherm. Res. 95:9-22.

Lu Z, Mann D, Freymueller JT, Meyer DJ (2000) Synthetic aperture radar interferometry of Okmok Volcano, Alaska; radar observations, J. Geophys. Res. 105:10791-10806.

Mandeville CW, Carey S, Sigurdsson H, King J (1994) Paleomagnetic evidence for high-temperature emplacement of the 1883 subaqueous pyroclastic flow from Karkatau Volcano, Indonesia, J. Geophys. Res. 99:9487-9504.

Mandeville CW, Carey S, Sigurdsson H (1996) Sedimentology of the Krakatau 1883 submarine pyroclastic deposits, Bull. Volcanol. 57:512-529.

Miller TP, Smith RL (1987) Late quaternary caldera-forming eruptions in the eastern Aleutian arc, Alaska, Geology 15:434-438.

Pope SB (2000) Turbulent Flows, Cambridge University Press, 771 p.

Pyle DM (1989) The thickness, volume and grainsize of tephra fall deposits, Bull. Volcanol. 51:1-15.

Riehle JR (1973) Calculated compaction profiles of rhyolithic ash-flow tuffs, Bull. Geol. Soc. Am. 84:2193-2216.

Schumacher R, Schmincke H-U (1990) The lateral facies of ignimbrites at Laacher See volcano, Bull. Volcanol. 52:271-285.

Sigurdsson H, Carey S (1989) Plinian and co-ignimbrite tephra fall from the 1815 eruption of Tambora volcano, Bull. Volcanol. 51:243-270.

Sparks RSJ (1976) Grain size variations in ignimbrite and implications for the transport of pyroclastic flows, Sedimentology 23:147-188.

Sparks RSJ, Bursik MI, Carey SN, Gilbert JS, Glaze LS, Sigurdsson H, Woods AW (1997) Volcanic Plumes, John Wiley & Sons, 574 p.

Sparks RSJ, Sigurdsson H, Carey SN (1980) The entrance of pyroclastic flows into the sea, I. oceanographic and geologic evidence from Dominica, Lesser Antilles, J. Volcanol. Geotherm. Res. 7:87-96.

Suzuki-Kamata K (1988) The ground layer of Ata pyroclastic flow deposit, southwestern Japan; evidence for the capture of lithic fragments, Bull. Volcanol. 50:119-129.

Thomas RME, Sparks RSJ (1992) Cooling of tephra during fallout from eruption columns Bull. Volcanol. 54:542-553.

Valentine G (1987) Statified flow in pyroclastic surges, Bull. Volcanol. 49:616-630.

Valentine GA, Fisher RV (2000) Pyroclastic surges and blasts, *in*: Sigurdsson H (ed) Encyclopedia of Volcanoes, Academic Press, 571-580.

Watts P, Waythomas CF (2003) Theoretical analysis of tsunami generation by pyroclastic flows, J. Geophys. Res. 108, B5:10.1029/2002JB002265.

Whitham AG, Sparks RSJ (1986) Pumice, Bull. Volcanol. 48:209-223.

Wilson CJN (1985) The Taupo eruption, New Zealand II. The Taupo ignimbrite, Phil. Trans. Royal Soc. London, A314:229-310.

Wolfe BA (2001) Paleohydrology of a catastrophic flood release from Okmok caldera and post-flood eruption history at Okmok volcano, Umnak Island, Alaska, M.S. Thesis, U. Alaska Fairbanks, 100 p.

Woods AW, Bursik MI, Kurbatov AV (1998) The interaction of ash flows with ridges, Bull. Volcanol. 60:38-51.

Redox evolution of a degassing magma rising to the surface

ALAIN BURGISSER, BRUNO SCAILLET

Institut des Sciences de la Terre d'Orléans, CNRS – Université d'Orléans

Publié dans: Nature (2007) v. 445, p.194-197.

Abstract

Volatiles carried by magmas, either dissolved or exsolved, exert a fundamental role on a variety of geological phenomena such as magma dynamics[1-5] or the composition of Earth's atmosphere[6]. In particular, the redox state of volcanic gases emanating at the Earth surface is widely believed to mirror that of their magma source, and thought to have exerted a first order control on the secular evolution of atmospheric oxygen[6-7]. However, fO_2 estimates retrieved from lava or gas chemistry may differ by as much as one log unit[8-10], the reason of such a difference remaining obscure. Here, by using a coupled chemical-physical model of conduit flow, we show that the redox state evolution of an ascending magma, and thus of its coexisting gas phase, is strongly dependent on both the composition and amount of gas in the reservoir. Magmas with no sulphur show a systematic fO_2 increase during ascent, by as much as 2 log units. Magmas with sulphur show also a change of redox state during ascent, but the direction of change depends on the initial fO_2 in the reservoir. Our calculations closely reproduce the H_2S/SO_2 ratios of volcanic gases observed at convergent settings, yet the difference between fO_2 in the reservoir and that at the exit of the volcanic conduit may be as much as 1.5 log unit. This fO_2 evolution provides one explanation for the apparent conflict documented between lava and gas based fO_2 estimates. We thus conclude that the redox state of erupted magmas is not necessarily a good proxy of the redox state of the gases they emit. Our findings may require re-evaluation of current models aimed at quantifying the role of magmatic volatiles on geological processes.

Recent studies have investigated the role of redox equilibria during volatile exsolution but the solution of the numerical problem requires fixing either iron or sulphur redox states[11]: as a result, the effect of decompression on oxygen fugacity (fO_2) cannot be evaluated. In the present work, we relax such an assumption by taking advantage of the fact that the solubility laws of key volatile species other than H_2O and CO_2 have been recently determined, in particular that of H_2, SO_2, and H_2S [12,13]. In this work we considered gas phases in the system H-O-S, with 6 species (H_2O, H_2, SO_2, H_2S, S_2, and O_2) in which the following redox equilibria occur:

$$H_2 + ½\ O_2 = H_2O \quad (1)$$

$$H_2S + ½\ O_2 = H_2O + ½\ S_2 \quad (2)$$

$$O_2 + ½\ S_2 = SO_2 \quad (3)$$

Standard thermodynamic considerations[14,15] show that once total pressure, P, temperature, T, and two additional intensive parameters such as water and hydrogen fugacities (fH_2O and fH_2) are known, the fugacities of all remaining species (fH_2S, fO_2, fS_2, fSO_2) are fixed and the gas phase composition in the H-O-S system is fully determined. Each species *i* in the gas has a mole fraction m_i :

$$\Sigma m_i = 1$$

The gas phase is modelled as an ideal mixture of non-ideal gases, a valid approximation in the pressure range considered here. Departure from ideal behaviour of end-member species is accounted for by the fugacity coefficient γ_i which is fixed by P and T[16]. The total weight fraction of each species (w_{Ti}) is the sum of its exsolved part (w_{gi}) and its dissolved part:

$$w_{Ti} = w_{gi} + a_i\ (\gamma_i m_i P)^{bi}$$

where a_i and b_i are solubility constants experimentally determined (Table 1). We use a homogeneous, one-dimensional conduit flow model[5] to simulate magma ascent under closed system and equilibrium conditions. Magma rises in a cylindrical conduit at constant mass flux and volatile exsolution affects the flow through changes in buoyancy and viscosity (cf. Supplementary Information). Calculations are performed by first fixing P, T, fH_2O fH_2, and the amount of gas in the reservoir. The model seeks first the equilibrium distribution of each volatile species between gas and melt prior to ascent. Then, at each next lower pressure, mass conservation requires that total amounts of each element (O, H, and S) remain constant. Using this constraint, the model calculates the equilibrium distribution of volatile species, which in turn affects ascent dynamics.

Table 1: Solubility constants

species	a_i	b_i
H_2O	$1.063\ 10^{-3}$	0.5399
H_2	$3.400\ 10^{-7}$	1.2800
SO_2	$1.632\ 10^{-10}$	1.3789
H_2S	$8.239\ 10^{-6}$	0.5145
O_2	0	-
S_2	0	-

The a_i and b_i parameters were determined by fitting experimental solubility data of corresponding species to an empirical equation of the form $w_i = a_i f_i^{bi}$. We have used data from ref . 12 for sulphur bearing species, ref. 13 for hydrogen and ref. 29 for water.

Redox equilibrium during magma ascent involving dissolved iron can be written such as:

$$Fe_2O_3 = 2\ FeO + ½\ O_2 \quad (4)$$

The importance of such a reaction will be dictated by the initial amount of dissolved iron oxides. It is currently not possible to include iron as a species into our thermodynamic model because the activities of FeO and Fe_2O_3 are not known. We thus simulated the redox effect of iron by using an empirical model[17]. Runs under typical storage conditions of arc rhyolites (≤1 wt% total iron and fO_2 between NNO-1 and NNO+1, fO_2 being referenced to the solid buffer Ni-NiO, such that NNO+1 means an fO_2 one order of magnitude higher than NNO) show that reaction (4) partly buffers changes in fO_2 when little gas is present in the reservoir (<0.2 unit log without changing the redox trend during ascent, see SI). In contrast, in iron-rich liquids such as basalts, the buffering capacity of iron species will be higher. Thus our results primarily apply to magmas in which the residual melt is rhyolitic, as commonly observed in arc settings. We did not consider the role of iron in crystals because the role of solid buffers as a first order mechanism controlling redox state during magma ascent can be ruled out on kinetic grounds. The lattice diffusion processes that this mechanism requires are exceedingly slow compared to those in gas or liquid phases. Similarly, for simplicity we have not investigated the role of CO_2 since detailed petrologic studies of silicic magmas in arcs show them to have little or no CO_2 under pre-eruptive conditions[18]. In general, however, introduction of CO_2 will lower fH_2O and thus drives our calculated values toward lower fO_2 via equilibrium (1). Our assumption of equilibrium implies that the model might not capture the chemical evolution of the gas within rapidly decompressed magmas such as in Plinian eruptions, in which the contrasted diffusive kinetics of volatile species may inhibit attainment of equilibrium. Both H_2O and H_2 are, however, fast diffusing species relative to CO_2 and S-bearing ones[18,19]. Thus, if physical fractionation of volatile species arises during ascent, the gas phase composition will be driven toward the system H-O (C and S species remain in the melt, such as documented for S for the 1991 Pinatubo eruption[20]), which will exert a dominant control on the redox state of escaping gases. Our model represents thus a fundamental end-member case toward which magmas, notably those intermediate to silicic in arc settings, tend to evolve.

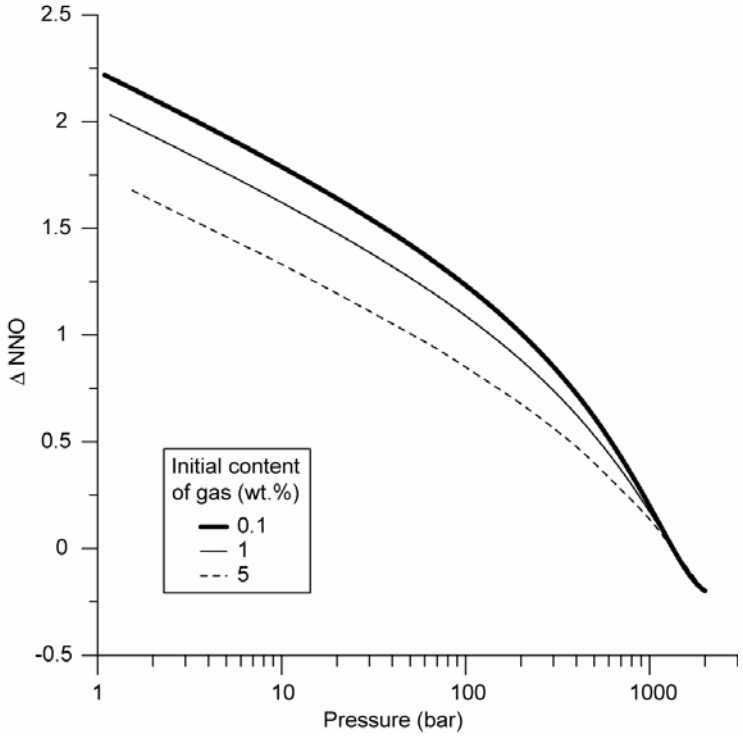

Figure 1: Fundamental relationship between magma ascent and magma redox state, for a rhyolite magma coexisting with a H-O gas. From gas content and composition at depth, the coupled model of conduit flow calculates the evolution of the physical and chemical conditions of the ascending magma. The effect of equilibrium degassing is a systematic increase in fO_2 (referenced to the NNO buffer) with shallower pressure. Representative cases for 3 initial values of exsolved volatiles with an fH_2 initially fixed at 10 bar.

We have explored the following range of starting conditions typical of silicic arc magmas[21,22]: an initial pressure from 2000 to 3000 bars, fO_2 from NNO+2 to NNO-0.5, bulk iron contents (FeO*) up to 3 wt%, bulk water contents up to 10.4 wt% and bulk sulphur contents up to 3 wt%, the two latter parameters being adjusted by varying the amount of excess gas in the reservoir (up to 5 wt%[23]). The conduit radius was fixed at 5 m for all runs. Temperature has been fixed to 825°C, i.e. typical of rhyolite magmas[21], and melt density to 2140 kg/m^3, though different choices will not affect the trends observed. Runs are constrained to reach atmospheric pressure at the vent, which yields initial ascent rates between 0.7 and 12 m/s. Because degassing occurs in equilibrium, changes in chemistry as a function of pressure occur regardless of ascent speed. In all cases, the simulations are carried down to atmospheric pressure though it can be anticipated that the last increments of fO_2 change we compute might not be reached owing either to the inhibiting effect of viscosity at low water content[24] or to gas loss once a permeability threshold is reached such that the system becomes open to gas[25].

We first consider the S- and Fe-free case. All simulations performed showed essentially identical behaviour in terms of redox state evolution, i.e. the fO_2 of the magma increases during ascent, the magnitude of increase being more or less dampened by the amount of free gas present in the reservoir. A representative example is shown on Figure 1, corresponding to a magma initially stored at 2000 bars, at an fO_2 of NNO-0.2, with a melt H_2O content of 5.46 wt% and for excess gas contents of 0.1, 1, and 5 wt%. The simulations show that the magnitude of fO_2 change increases when the amount of excess gas decreases, and can reach more than two log units for a gas-poor magma (0.1 wt%).

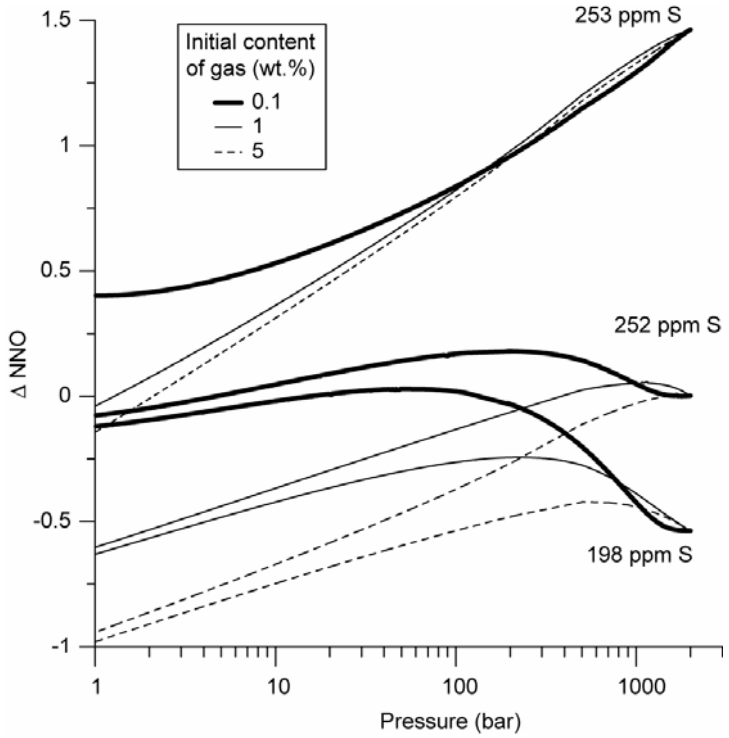

Figure 2: Fundamental relationship between magma ascent and magma redox state, for a rhyolite magma coexisting with a H-O-S gas. Effect of initial redox state on its evolution during decompression. Representative cases for 3 starting values of exsolved volatiles with an fH_2O initially fixed at 1000 bar. Initial redox state was achieved by varying fH_2 (ΔNNO-0.5: fH_2 = 10,ΔNNO+0: fH_2 = 5.38, ΔNNO-1.5: fH_2 = 1).

We now explore the case of sulphur-bearing rhyolite magma with 1 wt.% of total iron and stored at 2000 bar, illustrating our calculations with three different initial fO_2 but similar initial dissolved sulphur contents (ca. 200-250 ppm). A magma starting at an fO_2 of NNO-0.5 displays a continuous increase in its fO_2 as it ascends, except in the last few hundred bars where a reversal in fO_2 toward reduction occurs (Fig. 2). The magnitude of change is strongly dependent on the amount of gas initially present in the reservoir. At low gas content (0.1

wt%), the fO_2 rises by 0.7 log unit relative to starting conditions. With 5 wt% gas, the magma has a redox state nearly constant up to a pressure of 100 bars. When the starting fO_2 in the reservoir is at NNO (Fig. 2), the magma undergoes oxidation only for gas-poor conditions (0.1 wt%). Higher amounts of gas in the reservoir impart a reducing trend in the fO_2 evolution during ascent, the final fO_2 differing by almost one log unit from the initial value for an initial gas content of 5 wt%. When the initial fO_2 in the reservoir is at NNO+1.5, the magma undergoes a significant reduction during ascent regardless of its initial gas content (Fig. 2). In this case, the drop in fO_2 may exceed 1.5 log units at near atmospheric conditions for gas rich conditions.

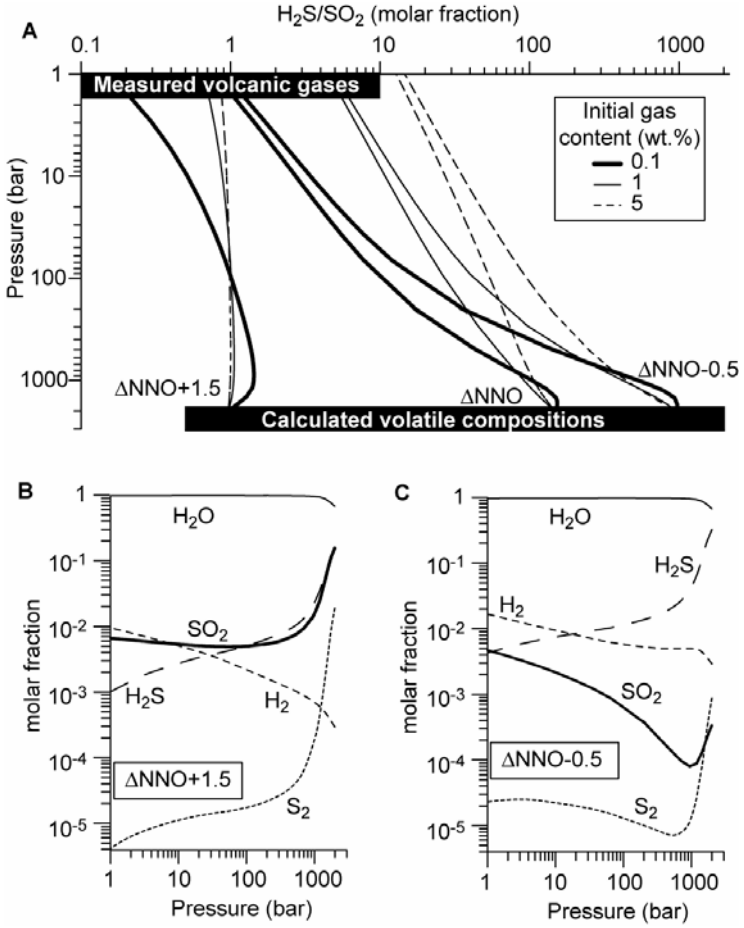

Figure 3: Evolution of the composition of an H-O-S gas phase during ascent of a rhyolite magma. A) Effect of the initial redox state on the ratio H_2S/SO_2 for 3 starting values of fO_2, each with three different gas contents (same initial conditions as in Fig. 2). Natural range observed on active volcanoes in convergent settings[26], and range calculated by phase equilibra experiments[21] are also shown. B) Evolution of the gas composition for a magma oxidized at depth (ΔNNO+1.5, 0.1 wt% gas). C) Evolution of the gas composition for a magma reduced at depth (ΔNNO-0.5, 0.1 wt% gas). Contents of O_2 are too low (<10 ppm) to be displayed

The change in fO_2 during decompression is accompanied by dramatic changes in gas phase composition (Fig. 3). Our calculated H_2S/SO_2 ratios fall in the range 0.1-10, which is comparable to that of volcanic gases measured at convergent settings for silicic to intermediate magmas[26] (Fig. 3). Clearly, a variety of H_2S/SO_2 ratio can be produced from magmas having common initial redox states but different amounts of gases. Conversely, a given H_2S/SO_2 ratio may be produced from a wide range of starting redox conditions. For instance a H_2S/SO_2 ratio of about one can be produced from a magma initially stored at NNO+1.5 with 5 wt% gas, or from a magma initially at NNO-0.5 with 0.1 wt% gas (Fig. 3a). Thus, anticipating the H_2S/SO_2 ratio of gases emanating from a given reservoir would require knowing not only the reservoir fO_2 but also the amount of free gas present in the reservoir and the depth at which gas and melt are physically separated. Although such a rich behaviour

precludes a simple explanation for each trend calculated, a sensitivity analysis of our model suggests that water exsolution plays an important role in oxidizing the system, and that, on the other hand, the complex pressure dependence of the redox equilibria (1)-(3) contribute to the reducing trends. Our findings have thus obvious implications for the use of volcanic gases as a monitoring tool of volcanic activity. They also illustrate the important role of sulphur. Magmas poor in sulphur or in which reactions involving sulphur are kinetically inhibited are likely to undergo a significant increase in their redox state during ascent.

The above results show that the redox state that magma records at depth does not necessarily mirror that of its escaping gases, in particular when they are released from levels shallower than the main reservoir. Thus, from a broader perspective, our findings have implications for our understanding on how past volcanic activity may have impacted Earth's atmosphere. Current models of the evolution of atmospheric oxygen implicitly assume that the redox state of magmatic rocks can be taken as equal to that of their outgassed products[6,7]. Our calculations show that, for silicic magmas, this assumption holds true only under a restricted set of conditions (for instance a magma starting at NNO-0.5 with 1 wt% gas, Fig. 2). Oxidized silicic magmas are particularly prone to redox change during ascent. A recent study[10] has stressed the difference in fO_2 retrieved from volcanic gas[11] and volcanic glass[12] at Kilauea volcano: the basaltic glass, which is fully degassed, records an fO_2 lower by 1.2 log unit than the gases. Although our model is calibrated on Fe-poor liquids, its predictions are qualitatively in accord with such an observation which suggests that even for basaltic magmas in non-arc settings, redox change during degassing may occur[27]. The corollary is that the iron redox state of a magma may significantly differ from its source, in contrast to conventional wisdom[28]. Altogether, this suggests that equating the redox state and composition of present day volcanic gases to those emitted in the geologic past[6] may not be a correct assumption.

References

1. Wilson, L., Sparks, R.S.J. & Walker, G.P.L. Explosive volcanic eruptions. IV. The control of magma properties and conduit geometry on eruption column behavior. *Geophys. J.R. Astron. Soc.* 63, 117-148 (1980)
2. Papale, P. Strain-induced magma fragmentation in explosive eruptions. *Nature* 397, 425-428 (1999).
3. Huppert, H.E. & Woods, A.W. The role of volatiles in magma chamber dynamics. *Nature* 420, 493-495 (2002).
4. Gonnerman, H.M. & Manga, M. Explosive volcanism may not be an inevitable consequence of magma fragmentation. *Nature* 426, 432-435 (2003).
5. Burgisser, A. & Gardner, J. Experimental constraints on degassing and permeability in volcanic conduit flow. *Bull. Volc.* 67, 42-56 (2005).
6. Holland, H.D. Volcanic gases, black smokers and the great oxidation event. *Geochim. Cosmochim. Acta* 66, 3811-3826 (2002).
7. Kasting, J.F., Eggler, D.H. & Raeburn, S.P. Mantle redox evolution and the oxidation state of the atmosphere. *J. Geol.* 101, 245-257 (1993).
8. Gerlach, T.M. Comment on paper « Morphology and compositions of spinel in Pu'u'O'o lava (1996-1998), Kilauea volcano, Hawaii'-enigmatic discrepancies between lava and gas-based fO_2 determinations of Pu'u'O'o lava, *J. Volcanol. Geotherm. Res*. 134, 241-244 (2004).
9. Gerlach, T.M. Oxygen buffering of Kilauea volcanic gases and the oxygen fugacity of Kilauea basalt. *Geochim. Cosmochim. Acta* 57, 795-814 (1993).
10. Roeder, P.L., Thornber, C. Proustovetov, A. & Grant, A. Morphology and composition of spinel in Pu'u'O'o lava (1996-1998), Kilauea volcano, Hawaii. *J. Volcanol. Geotherm. Res.* 123, 245-265 (2003).
11. Moretti, R. & Papale, P. On the oxidation state and volatile behavior in multicomponent gas-melt equilibria. *Chem. Geol*. 213, 265-280 (2004)
12. Clemente, B., Scaillet, B. & Pichavant, M. The solubility of sulphur in hydrous rhyolitic melts. *J. Petrol.* 45, 2171-2196 (2004).
13. Gaillard, F., Schmidt, B. Mackwell, S. & McCammon, C. Rate of hydrogen–iron redox exchange in silicate melts and glasses. *Geochim Cosmochim. Acta 67*, 2427-2441 (2003).
14. Holloway, J.R. Thermodynamic modelling of geological materials: minerals, fluids and melts. *Reviews in Mineralogy* (eds. Carmichael, I.S.E. & Eugster, H.P.) 17, 211-233 (Mineralogical Society of America, Book Crafters, Chelsea, MI, 1987).
15. Scaillet, B. & Pichavant, M. Role of fO_2 on fluid saturation in basalts. *Nature*, doi 10/1038 (2004)

16. Shi, P.F. & Saxena, F.K. Thermodynamic modeling of the C-H-O-S fluid system. *Amer. Mineral*. 77, 1038-1049 (1992).
17. Kress, V.C., & Carmichael, I.S.E. The compressibility of silicate liquids containing Fe2O3 and the effect of composition, temperature, oxygen fugacity and pressure on their redox states. *Contrib. Mineral. Petrol.* 108, 82-92 (1991).
18. Wallace, P. Volatiles in subduction zone magmas: concentrations and fluxes based on melt inclusion and volcanic gas data. *J. Volcanol. Geotherm. Res.* 140, 217-240 (2004).
19. Watson, E.B. (1994). Diffusion in volatile-bearing magmas. In Carroll, M.R. & Holloway, J.R (eds), Volatiles in magmas, *Rev. Mineral*. 30, 371-412.
20. Westrich, H.R. & Gerlach, T.M. Magmatic gas source for the stratospheric SO_2 cloud from the June 15, 1991 eruption of Mount Pinatubo. *Geology* 20, 867-870 (1992).
21. Scaillet, B. & Pichavant, M. Experimental constraints on volatile abundances in arc magmas and their implications fro degassing processes, in Volcanic degassing, C. Oppenheimer, D. Pyle & J. Barclay (eds.) *Geol. Soc. Spec. Pub*. 213, 23-52 (2003)
22. Scaillet, B., Luhr, J. & Carroll, M.R. Petrological and volcanological constraints on volcanic sulfur emissions to the atmosphere. In Volcanism and the Earth's Atmosphere, A. Robock & C. Oppenheimer (eds.), *Geophys. Monog*. 139, 11-40 (2003).
23. Wallace, P., Anderson, A.T. & Davis, A.M. Quantification of pre-eruptive exsolved gas contents in silicic magmas. *Nature* 377, 612-616 (1995).
24. Gardner, J.E., Hilton, M. & Carroll, M.R. Bubble growth in highly viscous silicate melts during continuous decompression from high pressure, *Geochim. Cosmochim. Acta 64*, 1473-1483 (2000).
25. Eichelberger, J.C., Carrigan, C.R., Westrich, H.R. & Price, R.H. Non explosive silicic volcanism. *Nature* 323, 598-602 (1986).
26. Symonds, R.B., Rose, W.I., Bluth, G.J.S., and Gerlach, T.M. Volcanic-gas studies: methods, results, and applications, in: Carroll, M.R., and Holloway, J.R. (eds) Volatiles in magmas, Reviews in Mineralogy, v. 30, p. 1-66 (1994).
27. Mathez, E.A. Influence of degassing on oxidation states of basaltic magmas. *Nature* 310, 371-375 (1984).
28. Carmichael, I.S.E. The redox states of basic and silicic magmas: a reflexion of their source regions. *Contrib. Mineral. Petrol.* 106, 129-141 (1991).
29. Holtz, F., Behrens, H., Dingwell, D.B. & Johannes, W. H_2O solubility in haplogranitic melts: compositional, pressure and temperature dependence. *Am. Mineral.* 80, 94-108 (1995).

Acknowledgements

We thank M. Rutherford, P. Wallace, and an anonymous reviewer for critical comments that helped us to improve our model. A.B. acknowledges support from the Swiss National Science Foundation.

Supplementary Information

A coupled chemical-physical model of magma ascent allowed us to establish the relationship between the ascent of magma and its redox state. The chemistry formulation is based on that of Clemente et al. (2004), whereas the physical part is based on Burgisser and Gardner (2005). The gas phase is composed of n species, each with a molar fraction m_i:

$$\sum_{i=1}^{n} m_i = 1 \tag{1}$$

Conversion between molar fraction and weight fraction is:

$$x_i = \frac{m_i M_i}{\sum_j m_j M_j} \tag{2}$$

where M_i are molecular weights of each species. The total weight fraction of each species (w_{Ti}) is the sum of its exsolved part and its dissolved part:

$$w_{Ti} = w_{gT} x_i + a_i (f_i)^{b_i} \tag{3}$$

where w_{gT} is total gas weight fraction, a_i and b_i are solubility constants determined experimentally (Table 1), and f_i is species fugacity. We assume the gas phase is an ideal mixture of non-ideal gases, which yields the following expression for fugacities:

$$f_i = \gamma_i m_i P \tag{4}$$

where P is total pressure, and coefficients γ_i are calculated at each pressure step following Shi and Saxena (1992). Using (2) and (4), (3) can be written as:

$$w_{Ti} = w_{gT} \frac{m_i M_i}{\sum m_j M_j} + a_i (\gamma_i m_i P)^{b_i} \tag{5}$$

System H-O

The gas phase is composed of 3 species (H_2O, H_2, and O_2) that are in equilibrium at all times:

$$K_1 = (fH_2O)(fH_2)^{-1}(fO_2)^{-1/2} \tag{6}$$

where K_1 is an equilibrium constant calculated according to Robie et al. (1979). Replacing the fugacities by their expressions in (4) yields:

$$K_1 = (\gamma_{H2O} m_{H2O})(\gamma_{H2} m_{H2})^{-1}(\gamma_{O2} m_{O2} P)^{-1/2} \tag{7}$$

Initially, w_{gT} and $f\mathrm{H}_2$ are set at a given pressure and temperature at depth. The molar composition of the gas phase can be determined by using (4) to calculate m_{H2}, (1) and (7) to calculate m_{O2}, and (1) to calculate m_{H2O}. When decompression occurs, mass conservation requires that total amounts of oxygen and hydrogen of the system remain constant. Total weight percents of atomic oxygen (w_{TO}) and atomic hydrogen (w_{TH}) can be determined from initial gas composition by using:

$$w_{TO} = M_O \left(\frac{w_{TH2O}}{M_{H2O}} + 2\frac{W_{TO2}}{M_{O2}} \right) \tag{8a}$$

$$w_{TH} = M_H \left(2\frac{w_{TH2O}}{M_{H2O}} + 2\frac{W_{TH2}}{M_{H2}} \right) \tag{8b}$$

and replacing the total amount of each species w_{Ti} in (8) by their expressions in (5):

$$\frac{w_{TO}}{M_O} = \frac{w_{gT} m_{H2O}}{\sum m_j M_j} + \frac{a_{H2O}(\gamma_{H2O} m_{H2O} P)^{b_{H2O}}}{M_{H2O}} + 2\frac{w_{gT} m_{O2}}{\sum m_j M_j} \tag{9a}$$

$$\frac{w_{TH}}{2M_H} = \frac{w_{gT} m_{H2O}}{\sum m_j M_j} + \frac{a_{H2O}(\gamma_{H2O} m_{H2O} P)^{b_{H2O}}}{M_{H2O}} + \frac{w_{gT} m_{H2}}{\sum m_j M_j} + \frac{a_{H2}(\gamma_{H2} m_{H2} P)^{b_{H2}}}{M_{H2}} \tag{9b}$$

When total pressure decreases, the molar fractions (m_{H2O}, m_{H2}, and m_{O2}) and the total amount of volatiles exsolved (w_{gT}) are constrained by mass conservation, chemical equilibrium, and solubility laws embedded in the four equations (1), (7), (9a), and (9b). Using (1) and (7), m_{H2O} and m_{H2} can be expressed as a function of m_{O2}:

$$m_{H2O} = (1 - m_{O2}) \left(1 + \frac{\gamma_{H2O}}{K_1 \gamma_{H2} \sqrt{m_{O2} \gamma_{O2} P}} \right)^{-1}$$

$$m_{H2} = 1 - m_{O2} - m_{H2O} \tag{10}$$

Combining (9a) and (9b) as to eliminate w_{gT} and using (10) yields an expression for m_{O2} that we solved with an iterative procedure to find its roots:

$$\frac{w_{TH}}{2M_H(1-m_{O2})} - \frac{w_{TO}}{M_O(m_{H2O}+2m_{O2})} =$$
$$\frac{a_{H2}(\gamma_{H2} m_{H2} P)^{b_{H2}}}{M_{H2}(1-m_{O2})} + \frac{a_{H2O}(\gamma_{H2O} m_{H2O} P)^{b_{H2O}}}{M_{H2O}} \left(\frac{1}{1-m_{O2}} - \frac{1}{m_{H2O}+2m_{O2}} \right) \tag{11}$$

Because m_{H2O} is on the order of 10^{-1} and m_{O2} is usually $<10^{-10}$, it is essential to carry all calculations with sufficient numerical precision. We used a precision of 20 digits, which ensured that errors on m_{O2} values were <0.1% when $m_{O2}>10^{-17}$.

System H-O-S

The gas phase is composed of 6 species (H_2O, H_2, O_2, S_2, H_2S and SO_2) that are in equilibrium at all times:

$$K_1 = (fH_2O)(fH_2)^{-1}(fO_2)^{-1/2}$$
$$K_2 = (fSO_2)(fS_2)^{-1/2}(fO_2)^{-1}$$
$$K_3 = (fH_2S)(fO_2)^{1/2}(fS_2)^{-1/2}(fH_2O)^{-1} \quad (12)$$

where K_1, K_2, and K_3 are equilibrium constants (Ohmoto and Kerrick, 1977; Robie et al., 1979). The total weight percents of atomic oxygen (w_{TO}), atomic hydrogen (w_{TH}), and atomic sulfur (w_{TS}) are given by:

$$w_{TO} = M_O\left(\frac{w_{TH2O}}{M_{H2O}} + 2\frac{w_{TO2}}{M_{O2}} + 2\frac{w_{TSO2}}{M_{SO2}}\right)$$
$$w_{TH} = M_H\left(2\frac{w_{TH2O}}{M_{H2O}} + 2\frac{w_{TH2}}{M_{H2}} + 2\frac{w_{TH2S}}{M_{H2S}}\right)$$
$$w_{TS} = M_S\left(2\frac{w_{TS2}}{M_{S2}} + \frac{w_{TH2S}}{M_{H2S}} + \frac{w_{TSO2}}{M_{SO2}}\right) \quad (13)$$

Like the H-O system, the resolution is carried out in two steps. First, w_{gT}, fH_2O and fH_2 are set at depth so that the composition of the gas phase and the total amounts of each element could be determined. Second, each time pressure decreases, mass conservation (1) and (13), chemical equilibrium (12), and solubility laws (5) are used jointly to solve for the seven unknowns (molar fractions m_i and the total gas weight fraction w_{gT}).

Effects of Iron

When there is iron dissolved in the melt, the following redox reaction occurs:

$$FeO + \frac{1}{2}O_2 = Fe_2O_3 \quad (14)$$

It is currently not possible to include the redox effects of iron into our thermodynamic model because the activities of FeO and Fe_2O_3 dissolved into a rhyolitic melt are not known. It is, however, possible to simulate such effects by using an empirical model that links, at constant temperature, the molar ratio of FeO and Fe_2O_3 to the oxygen fugacity (Kress and Carmichael, 1991):

$$\ln\left(\frac{m_{Fe2O3}}{m_{FeO}}\right) = a_{KC}\ln(fO_2) + \frac{b_{KC}}{T} + c_{KC} + \sum_k d_{KCk}m_k + f_{KC}\frac{P}{T} + h_{KC}\frac{P^2}{T} \quad (15)$$

where k is one of (FeO*, Al_2O_3, CaO, Na_2O, and K_2O), m_k is the total molar fraction of these species, and a_{KC}, b_{KC}, c_{KC}, d_{KCk}, f_{KC}, h_{KC} are constants given in Kress and Carmichael (1991). We calculated the redox effect of iron in the H-O-S system by using (15) and keeping track of the total amounts of Fe (w_{TFe}), oxygen in the FeO and Fe_2O_3 form ($w_{TO(Fe)}$), and oxygen in the O_2, H_2O, and SO_2 form (w_{TO}).

Because the relation (14) contains the total molar fraction of several oxides and our mass balance (13) is in weight fraction, conversions between the two units are needed, and the total composition of the melt should be known. Thus, we fixed the total weight fraction of 9 major oxides of a typical rhyolite (in wt%: SiO_2=77.44, Al_2O_3=12.88, TiO_2=0.07, CaO=0.6, Na_2O=4.14, K_2O=4.76, MgO=0.03, MnO=0.05, P_2O_5=0.03). These initial values add up to 100%, and need to be corrected to take in account the amounts of volatiles and iron. For each run, initial quantities of FeO* (w_{TFeO*}), w_{gT}, fH_2O and fH_2 are set at depth. Using the same procedure as described in "*H-O-S system*", total amounts of sulphur, hydrogen, and oxygen in the O_2, H_2O, and SO_2 form can be calculated. The initial amount of oxygen in the FeO and Fe_2O_3 form is not known and should be determined using the empirical equation (14). Thus, the initial quantities of the 9 major oxides are normalized so that the 9 oxides, plus the volatiles species (w_{TO}, w_{TS}, w_{TH}), plus the total iron (w_{TFeO*}) add up to 100%. Then the total molar fraction of FeO*, Al_2O_3, CaO, Na_2O, and K_2O are calculated using:

$$m_i = \frac{w_{Ti}}{M_i} \frac{1}{\sum_j \frac{w_{Tj}}{M_j}} \quad (16)$$

The total amounts of iron and oxygen fixed by the iron can be expressed as:

$$m_{Fe} = m_{FeO} + 2m_{Fe2O3} \quad (17a)$$

$$m_{O(Fe)} = m_{FeO} + 3m_{Fe2O3} \quad (17b)$$

From (15), we define that

$$\frac{m_{Fe2O3}}{m_{FeO}} = KC \quad (18)$$

Combining (17)-(18), we get:

$$m_{O(Fe)} = m_{Fe} \frac{1+3KC}{1+2KC} \quad (19)$$

Using $w_{TFe} = \frac{w_{TFeO^*}}{M_{FeO}} M_{Fe}$ and the conversion (16) for w_{TFe} and $w_{TO(Fe)}$ yields the total amount of oxygen fixed by the iron:

$$w_{TO(Fe)} = M_O \frac{w_{TFe}}{M_{Fe}} \frac{1+3KC}{1+2KC} \quad (20)$$

The mass balance can now be rigorously carried out by adding the 9 oxides, the volatiles species (w_{TO}, w_{TS}, and w_{TH}), the total iron (w_{TFe}) and the oxygen fixed by the iron ($w_{TO(Fe)}$). The total molar fractions m_k can be updated using (16) and are used in (15) for the rest of the simulation. Because the system is closed, all the quantities involved in the mass balance, except w_{TO} and $w_{TO(Fe)}$, are considered constant. The reaction (14) imposes an exchange of oxygen between that locked in the Fe-bearing species and that involved in the H-O-S redox reactions. The sum $w_{TO} + w_{TO(Fe)} = w_{TO(Total)}$, however, remains constant. Thus, using (20), the total amount of "free" oxygen w_{TO} can be related to fO_2:

$$w_{TO} = w_{TO(Total)} - \frac{m_{Fe} M_O}{\sum_j m_j M_j} \frac{1+3KC}{1+2KC} \quad (21)$$

The numerical resolution of (21) needs to be coupled with that of the H-O-S system. For each pressure step, solving for the redox equilibrium of the volatile species (equations (1), (5), (12) and (13)) yields an fO_2 . This fugacity is used in (21) to obtain a new amount of "free" oxygen. The redox equilibrium of the volatile species is solved again with the updated w_{TO}, and the process is conducted iteratively until desired precision ($<10^{-5}$ % on w_{TO}) is reached. An under-relaxation factor of 0.1 is applied to the updated w_{TO} to ensure convergence in 20 to 30 iterations.

Runs with 1 wt% of total iron under typical storage conditions of arc rhyolites (fO_2 between NNO-0.5 and NNO+1.5) show that the buffering capacity of iron is limited to less than 0.2 unit log compared to the S-O-H system when little gas is present in the reservoir, and becomes insignificant when more gas is present in the reservoir (Fig. SI-1). Under such storage conditions, iron does not change the redox evolution of the magma with pressure. Similarly, the H_2S/SO_2 ratio changes by less than 0.2 log units when little gas is present in the reservoir and is unaffected by iron when the reservoir hosts a large amount of gas.

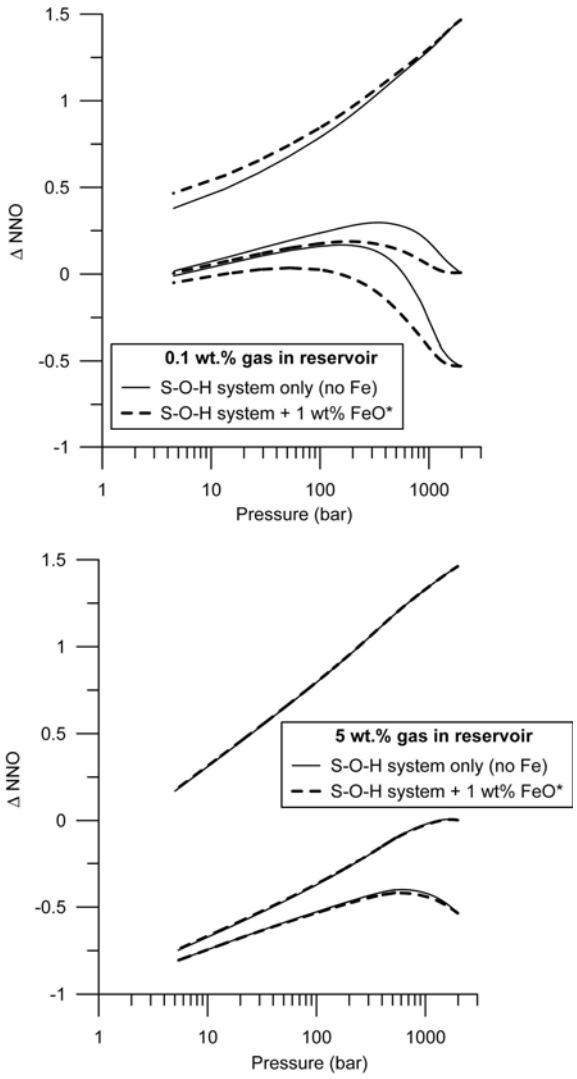

Figure SI-1: Effect of dissolved iron on the redox evolution of an ascending rhyolite. Stippled lines are runs with 1 wt.% total iron (FeO*) and solid lines are runs with no iron. Upper graph runs start with 0.1 wt.% gas at depth and lower graph runs start with 5 wt% gas at depth.

Physical part of the model

The conduit flow model is homogenous and one-dimensional. From mass and momentum conservation, the pressure evolution with depth (*dP/dz*) is given by:

$$\frac{dP}{dz} = v^2 \frac{d\rho}{dz} - \rho g - \frac{8\mu v}{r^2} - \frac{0.0025}{r}\rho v^2 \qquad (22)$$

where v is magma velocity, ρ is magma density, r is conduit radius, and g is gravity. The viscosity μ is calculated with the relationship by Hess and Dingwell (1996) for the melt and correcting for the effect of bubbles using the relationship by Dobran (1992). We note that using instead the relationship by Jaupart and Allègre (1991) for the effect of bubbles on viscosity did not change the trends caused by variations in volatile chemistry. Magma bulk density is:

$$\frac{1}{\rho} = \frac{w_{gT}}{\rho_g} + \frac{1 - w_{gT}}{\rho_l} \qquad (23)$$

where ρ_g is gas density from perfect gas law, and ρ_l is melt density. Replacing the derivative of (23) into (22) and rearranging gives:

$$\frac{dP}{dz} = \left[A\left(\frac{w_{gT}}{M}\frac{dM}{dz} - \left(1 - \frac{\rho_g}{\rho_l}\right)\frac{dw_{gT}}{dz} \right) - \rho g - \frac{8\mu v}{r^2} - \frac{0.0025}{r}\rho v^2 \right] \left[1 - \frac{A w_{gT}}{P} \right]^{-1} \qquad (24)$$

with

$$A = v^2 \rho_g \left(w_{gT} + (1 - w_{gT}) \frac{\rho_g}{\rho_l} \right)^{-2}$$

where M is the average molar mass of the gas phase:

$$M = \sum_{i=1}^{n} x_i M_i \qquad (25)$$

Above fragmentation (gas volume fraction >0.75), the viscosity is that of a dusty gas (Dobran, 1992), and degassing continues.

Equation (24) is solved using a fourth-order Runge-Kutta algorithm with adjustable distance step. At each pressure step, the gas composition is calculated for the system considered (H-O or H-O-S). The terms dM/dz and dw_{gT}/dz in (24) are evaluated implicitly, which can be justified by the fact that they are always several orders of magnitude smaller than inertia and viscous terms. Boundary condition is either atmospheric pressure at the vent, or initial velocity at depth. In the former case, a run starts with an initial guess for the velocity at depth, and the pressure is solved for until vent is reached. Initial velocity is then changed until upper boundary condition is satisfied. Because degassing occurs in equilibrium, changes in chemistry as a function of pressure are identical for the two cases.

References

Burgisser, A., and Gardner, J.E. (2005) Experimental constraints on degassing and permeability in volcanic conduit flow, Bulletin of Volcanology, v.67, p. 42-56.

Clemente, B., Scaillet, B. & Pichavant, M. The solubility of sulphur in hydrous rhyolitic melts. *J. Petrol.* 45, 2171-2196 (2004).

Dobran, F. (1992) Nonequilibrium flow in volcanic conduits and application to the eruptions of Mt. St. Helens on May, 18, 1980, and Vesuvius in AD 79, Journal of Volcanology and Geothermal Research, v.49, p. 285-311.

Hess, K-U., and Dingwell, D.B. (1996) Viscosities of hydrous leucogranitic melts: A non-Arrhenian model, American Mineralogist, v.81, p. 1297-1300.

Jaupart C, and Allègre C (1991) Gas content, eruption rate and instabilities of eruption regime in silicic volcanoes, Earth Planet Sci Lett 102:413-429

Kress, V.C., and Carmichael, I.S.E. (1991) The compressibility of silicate liquids containing Fe2O3 and the effect of composition, temperature, oxygen fugacity and pressure on their redox states, Contributions to Mineralogy and Petrology, v.108, p. 82-92.

Ohmoto, H., and Kerrick, D.M. (1977) Devolatilisation equilibria in graphitic systems, American Journal of Science, v.277, p. 1013-1044.

Robie, R.A., Hemingway, B.S., and Fisher, J.R. (1979) Thermodynamic properties of minerals and related substances at 298.15 K and 1 bar (10^5 Pa) pressure and at higher temperatures, US Geological Survey Bulletin 1452.

Shi, P.F. & Saxena, F.K. (1992) Thermodynamic modeling of the C-H-O-S fluid system. Amer. Mineral. 77, 1038-1049.